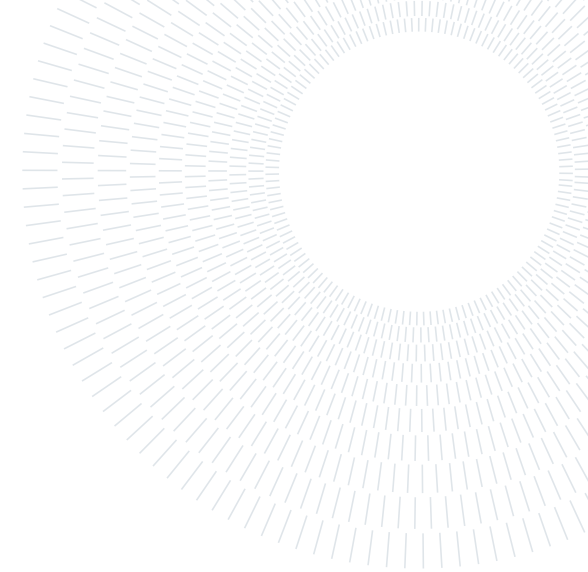




POLITECNICO
MILANO 1863

SCUOLA DI INGEGNERIA INDUSTRIALE
E DELL'INFORMAZIONE



EXECUTIVE SUMMARY OF THE THESIS

Modelling, control, integration and testing of an eVTOL drone

LAUREA MAGISTRALE IN AERONAUTICAL ENGINEERING - INGEGNERIA AERONAUTICA

Author: ELIA MARTINELLI

Advisor: PROF. MARCO LOVERA

Co-advisor: ENG. NICOLÒ BATTAINI

Academic year: 2021-2022

1. Introduction

There is a growing interest in unmanned aerial vehicles (UAVs) due to their capabilities: they can reduce time to perform complex tasks, like infrastructure inspections, or make missions like last mile delivery quicker and cheaper. Several UAV configurations have been adopted: the most popular is the multicopter one, which is easy to fly and not so expensive but presents a reduced flight time (usually less than an hour); the fixed-wing configuration, which allows to cover long ranges but requires a runway to take-off and land (or systems like a net or a cable to land). To overcome the cons of these two configurations, vertical take-off and landing (VTOL) aircraft have been designed: they represent the overlap of multicopter and fixed-wing UAVs since they can perform vertical take-off and landings, hovering flight and can fly for long distances thanks to the high efficiency wings.

1.1. Background

This thesis represents the third stage in the development of a VTOL UAV designed and built at *Politecnico di Milano* during two previous master theses. The first one is related to the design of the aircraft from initial requirements up to the production technical drawings; in the



Figure 1: eVTOL UAV developed at *Politecnico di Milano*

second one the production and integration of the components, together with the development of a simulator, have been performed. The aircraft, shown in Figure 1, is an electric VTOL (eVTOL) powered by a 8500 mAh LiPo battery that guarantees around 100 minutes of flight time; it has eight electrical motors for vertical flight and two for forward flight. Its wingspan is of 2.25 m and its mass is 4.8 kg.

This thesis has two main objectives: to develop the control system of the aircraft in all its flight phases (multicopter, fixed-wing and transition) and to test the aircraft in flight to gather experimental data. The study of the transition phase is of particular interest since it is the distinctive characteristic of a VTOL aircraft.

2. Hardware upgrades

After the first flights of the UAV, some hardware problems have been identified. They are related to:

- weight and balance: the weight is greater than expected due to a different manufacturing process of the components for technological reasons (mainly the tail);
- propulsion system: the selected motors for vertical flight provide less thrust than declared by the manufacturer; moreover, the power distribution is limited by the battery voltage drop and the maximum current required;
- structure: torsion of the fuselage is experienced when flying and vibrations of the wings are clearly visible.

These problems are solved at first, before starting the flight testing and control activities:

- a lighter wood tail is manufactured and installed to reduce the aircraft weight and improve longitudinal static stability (forward shift of the center of gravity towards the nose of the aircraft).
- Larger propellers are installed (7 inches diameter instead of 5 inches) to recover the required performance given the limitations shown by the motors; a second battery and a second power distribution board are installed: in this way the power distribution problem is mitigated.
- Structural supports are installed both on the front motor booms and inside the fuselage to reduce torsional problems. Moreover, the spinning direction of some motors for vertical flight is inverted to reduce these problems. The wing spars are connected to reduce the vibrations of these components.

As a result of these hardware upgrades, the VTOL mass is increased to 6.4 kg (33% increase) and the aircraft (previously statically unstable) has now neutral static stability. The simulator developed in the previous thesis is updated consequently.

3. Multicopter control

3.1. Control architecture

Several control architectures for multicopters have been developed at the *Aerospace Systems and Control Laboratory (ASCL)* of *Politecnico di Milano*.

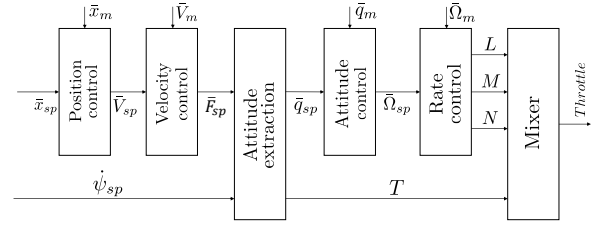


Figure 2: Multicopter controller architecture.

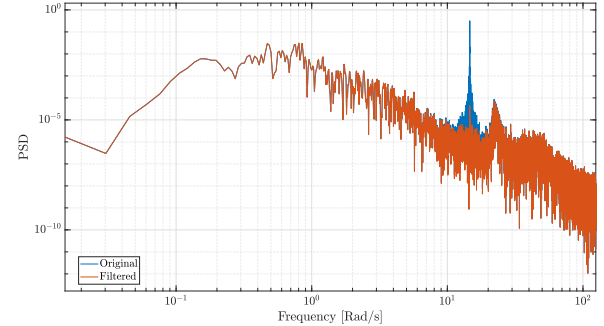


Figure 3: PSD of roll rate measurements, before and after filtering.

In this case a conventional cascaded PID loops architecture has been implemented (Figure 2): the inner loop controls attitude and angular rate while the outer loop controls position and velocity.

3.2. Controller tuning

As a reliable model for the attitude dynamics is not available, the following approach has been adopted:

1. preliminary tuning in simulation, based on a rigid-body model;
2. in-flight refinement of the tuning, taking also into account structural issues (a notch filter has been implemented to filter the structural vibrations produced by the wings. Figure 3 shows the power spectral density of the roll rate measurements before and after the filtering);
3. close-loop identification experiments, to collect data for model refinement;
4. model identification, both to obtain control-oriented model to further refine the tuning and to improve the fidelity of the simulator.

3.3. Results

The performance of the multicopter controller has been assessed using the gain and phase margins; Table 1 shows the values obtained.

	Phase margin [deg]	Gain margin [dB]
Roll rate	76.8	22.0
Pitch rate	63.9	11.6
Yaw rate	89.0	16.1
Roll angle	70.9	18.9
Pitch angle	76.0	16.9
Yaw angle	54.6	41.0
V_N	67.2	18.6
V_E	65.5	20.6
V_D	93.7	57.2
POS_N	53.5	12.9
POS_E	52.7	12.0
POS_D	48.5	38.4

Table 1: Multicopter controller evaluation.

4. Multicopter dynamics identification

An identification campaign of the multicopter dynamics has been performed; it focuses on the longitudinal, lateral, directional and vertical dynamics, in particular:

- lateral: from roll moment L to roll rate p ;
- longitudinal: from pitch moment M to pitch rate q ;
- directional: from yaw moment N to yaw rate r ;
- vertical: from force T to vertical speed v_z .

Identification is performed using a black-box approach. In particular the optimized version of the Predictor Based Subspace Identification method ($PBSID_{opt}$) is used which is a suitable and efficient solution to obtain an unstructured state-space model. The typical limitation is that it provides a model representation that is not physically-motivated. To obtain the best model, two excitation signals have been tested in closed-loop: Pseudo Random Binary Sequence (PRBS) and frequency sweep. An example of the identi-

	ω_{min} [rad/s]	ω_{max} [rad/s]	Amp.	T [s]
Lat	0.3	10	$0.1L_{max}$	30
Lon	0.3	10	$0.1M_{max}$	30

Table 2: Frequency sweep excitation signal: frequency range, amplitude and duration T.

	Order	VAF_{PRBS}	VAF_{pilot}
Lat	3	81%	84%
Lon	8	90%	83%
Dir	3	86%	-
Vert	4	65%	-

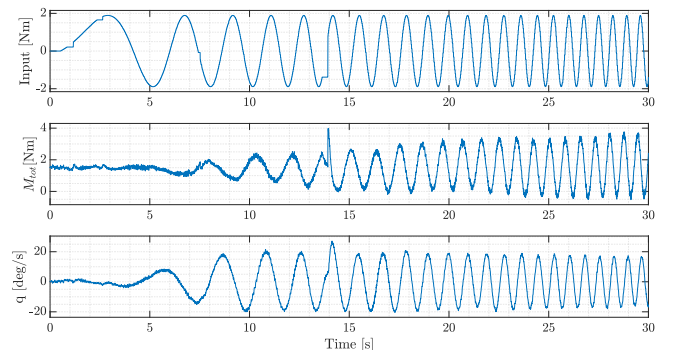
Table 3: Identification results.

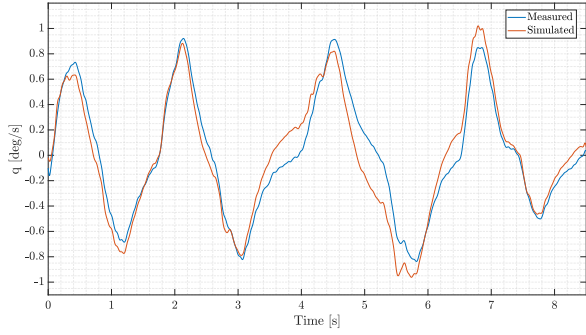
fication experiment for the pitch model identification with frequency sweep is shown in Figure 4.

Table 2 presents, as example, the characteristics of the frequency sweep signals used in the identification of the longitudinal and lateral dynamics.

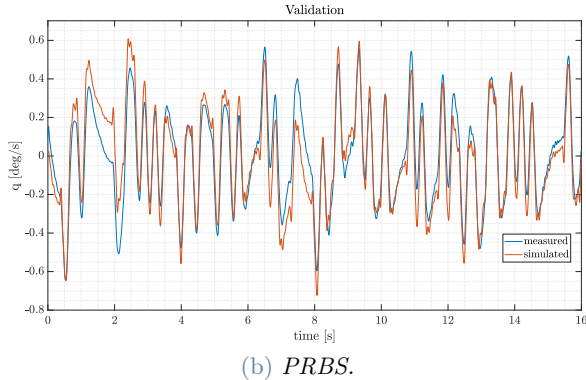
4.1. Results

In the case of longitudinal and lateral dynamics, the best results are obtained with the frequency sweep since it better excites the low frequency dynamics. Figure 5 shows the time-domain validation of the model of longitudinal dynamics while Table 3 shows the results of the obtained models: order, variance accounted for (VAR) with respect to PRBS and pilot input validation datasets.

Figure 4: Input, total pitch moment M_{tot} and pitch rate q in identification experiment.



(a) Manually piloted maneuvers.



(b) PRBS.

Figure 5: Time-domain validation for longitudinal dynamics.

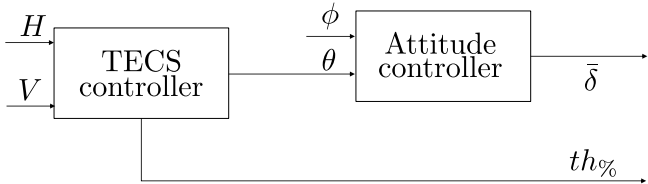


Figure 6: Fixed-wing control architecture.

5. Fixed-wing control

Since the aircraft works both as multicopter and as fixed-wing, also a controller for the latter has been designed. A cascade loop architecture is adopted, as presented in Figure 6; the inner loop controls the attitude (see Figure 7) while the outer loop controls the airspeed and the altitude at the same time (its detailed architecture is shown in Figure 8). For this part a total energy control system (TECS) approach has been used as described in the following.

5.1. TECS

The aircraft's responses in altitude and speed are coupled: an increase in thrust will generally increase both the airspeed and the altitude, while a nose-up elevator command will result in increasing altitude and decreasing speed. Con-

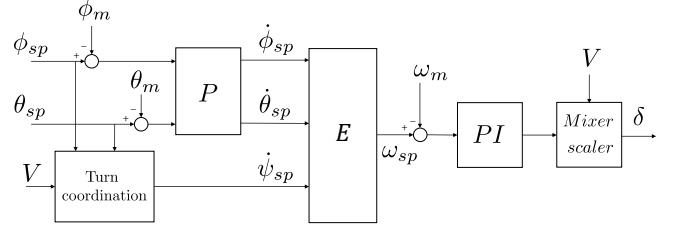


Figure 7: Fixed-wing attitude controller.

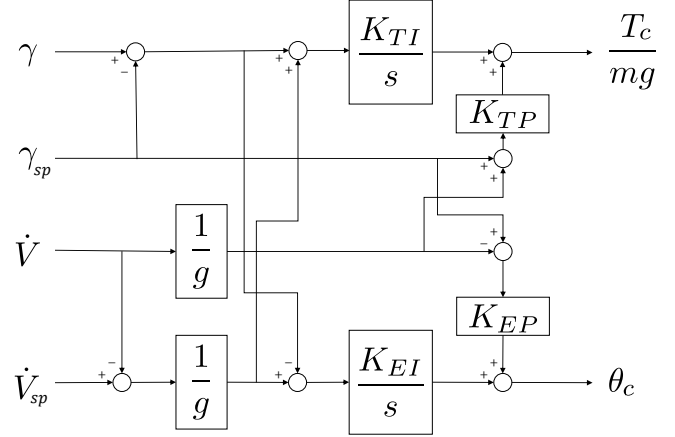


Figure 8: Fixed-wing TECS controller.

ventional SISO controllers do not account for this, leading to a lack of capability to provide integral flight envelope protection and to prevent control coupling problems. TECS offers a solution by representing the problem in terms of energies rather than in terms of the original setpoints.

Two versions of TECS have been implemented: the first one is based on the initial version developed by NASA in the '80s while the second one, although respecting the original structure, presents small but useful improvements. The main difference is that both the proportional and integral parts of the controller (not only the integral term) work on the error.

The developed controller has been tested in simulation, as shown in Figure 10.

6. Transition

The transition is the flight phase during which the VTOL passes from multicopter mode to fixed-wing mode and *vice versa*. This has to be done quickly, smoothly, without oscillations and, most important, without altitude changes. The transition from multicopter mode to fixed-wing mode is done by accelerating forward: the speed increases, the wings start to produce lift

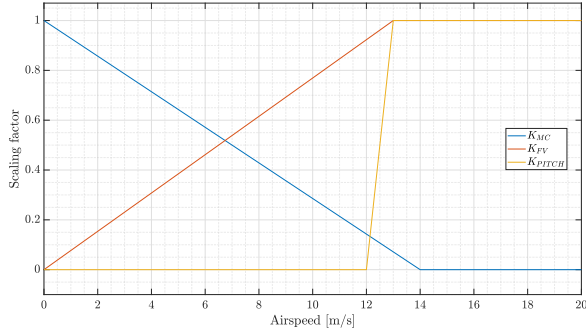


Figure 9: Scaling factors of transition control.

that will gradually replace the vertical force produced by the vertical motors in order to ensure equilibrium in the longitudinal plane. In this process both controllers work, each one with its own task:

- the multicopter controller maintains constant altitude and level attitude,
- the fixed-wing controller maintains constant altitude, level attitude and controls the forward airspeed.

More authority is given to the control logic that is more effective for the airspeed condition at hand: the control outputs are weighted with scaling factors that are function of the airspeed (K_{FW} for fixed-wing, K_{MC} for multicopter and K_{PITCH} for TECS pitch setpoint), shown in Figure 9.

The presented control strategy has been tested in simulation with a mission made up of vertical climb as multicopter, transition to forward flight, maneuvered flight in fixed-wing mode; the simulation result is shown in Figure 10. Figure 11 shows a detail of the vertical forces during the transition: the smooth exchange from multicopter mode to fixed-wing mode is clearly visible in the lift increase and the concomitante vertical thrust decrease.

The two versions of the TECS controller implemented in Section 5.1 have been used in the simulation. The modified controller shows the best results in terms of altitude holding.

As for the back transition, only a concept of the procedure has been developed. The logic to manage all the phases of a complete mission has been developed; a preliminary indoor flight test has been conducted with success.

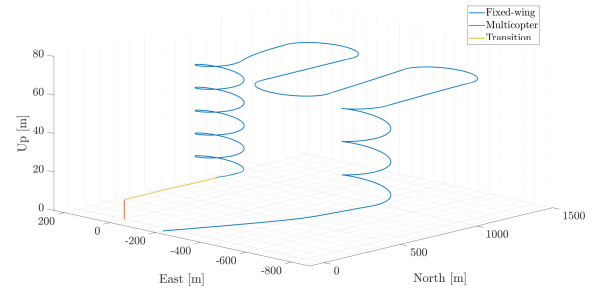


Figure 10: VTOL mission. Vertical take-off, transition and fixed-wing flight.

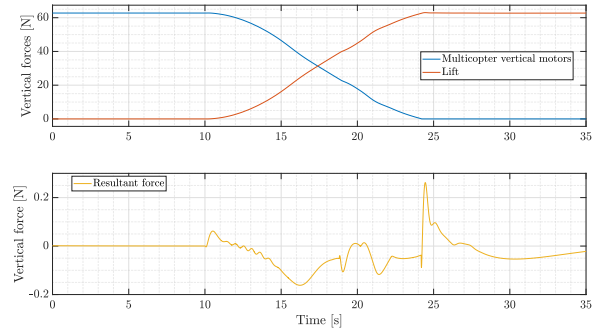


Figure 11: Vertical forces during transition.

7. Conclusion

In this thesis the modeling, control, integration and testing of an eVTOL completely designed and built at *Politecnico di Milano* has been carried out. Some initial hardware problems related to weight and balance, structure and propulsion which emerged during the integration phase have been solved. Then the multicopter controller has been designed: a conventional PID cascaded loops architecture has been adopted; the tuning has been performed manually in flight, achieving good results in terms of gain and phase margins. The multicopter model has been identified using a black-box approach with a frequency sweep excitation input signal applied in closed-loop. The obtained identified dynamics (longitudinal, lateral, directional and vertical) have been implemented in the simulator and validated against a flight data. After that, the fixed-wing controller has been designed, adopting also in this case a cascade loops architecture. In the case of the outer loop, responsible for altitude and airspeed, the total energy control system method has been implemented; two versions have been designed and compared to select the most suitable also for

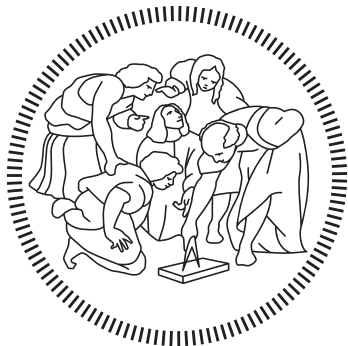
the transition. In the end, the control for transition flight has been designed: the mixing of the controller outputs is based on the forward velocity and the stall speed. As for the fixed-wing controller, also this part has been tested in simulation; however, an experimental test of the initial part of the procedure has been performed indoor. The results obtained present some limitations:

- the tuning of the multicopter controller has been performed only manually, no structured approach based on the identified model has been implemented;
- the fixed-wing and transition controllers have been tuned and tested only in simulation, an outdoor flight testing activity is still required.

Starting from the obtained results and their limitations, the following activities can be outlined:

- flight testing of the fixed-wing configuration,
- comparison of identified fixed-wing model with the present simulator,
- test of the transition procedure in flight.

POLITECNICO DI MILANO
Scuola di Ingegneria Industriale e dell'Informazione
Corso di Laurea Magistrale in Ingegneria Aeronautica



Modelling, control, integration and testing of an
eVTOL drone

Advisor: Prof. Marco LOVERA
Co-Advisor: Eng. Nicolò BATTAINI

Thesis by:
Elia MARTINELLI Matr. 928294

Academic Year 2021–2022

Alle mie montagne...

Acknowledgments

Il primo ringraziamento va al professor Marco Lovera per avermi dato la possibilità di lavorare su di un progetto interessante e vario, potendo sperimentare sul campo i concetti appresi dopo anni di faticosi studi. Il ringraziamento più grande va sicuramente a Nicolò; oltre ad essere stato un ottimo collega, si è dimostrato essere un vero amico. Ringrazio inoltre tutto lo staf del laboratorio *ASCL*: le giornate di lavoro in vostra compagnia sono sempre state divertenti e stimolanti. A tutta la mia famiglia, che mi ha sempre supportato. Ai compagni di università, che da vicini di banco sono diventati compagni di cordata e di avventure. *Last but not the least*, la mia professoressa di fisica del liceo, Emanuela Antolini, che con la sua passione mi ha indirizzato su questa strada.

Abstract

Nowadays, unmanned aerial vehicles (UAVs) represent a research field that is continuously expanding, due to their vast applications and economic advantages both in commercial and military cases: parcel delivery, aerial photography, search and rescue, reconnaissance and inspection are just some examples. The most common multi-rotor configuration has been studied in detail and has shown its limitations in terms of flight endurance: one of the solutions implemented in order to overcome this limit is the combination with the fixed-wing configuration. This is the case of Vertical Take Off and Landing (VTOL) UAVs, that combine the ability to hover, take-off and land vertically, with a high efficiency and long endurance and range typical of conventional fixed-wing aircraft.

The main purpose of this thesis is to implement and fly an electric VTOL (eVTOL) designed and built in two previous master thesis within the *Aerospace Systems and Control Laboratory* (ASCL) of *Politecnico di Milano*. In particular, in [1] the drone has been designed while in [2] it has been built and integrated. The result is a vehicle capable of both vertical and forward flight, with a take-off mass of around 6 kg, wing span of 2.25 m and an expected flight time of about 100 minutes. It is the first one to be completely designed and produced within the *Department of Aerospace Science and Technology* (DAER).

In details, during the thesis some initial hardware problems have been solved, mainly related to the propulsion system; then the control system for the different flight modes (multirotor, transition and fixed-wing) has been implemented. The *Simulink* model of the vehicle developed in previous works has been improved and the control module has been added, allowing to simulate all the flight modes of the drone. Then, the controllers have been installed on the eVTOL: the multi-rotor configuration has been successfully tested in flight, allowing to perform an identification campaign. The identified model has then been included in the flight simulator and compared to the previous analytical model, validating both with respect to a real flight. Transition and forward flight have been successfully tested in simulation, but a complete flight test has not been performed yet; only preliminary ground tests have been done: these experiments have confirmed the proper functioning of the controller and the results obtained in simulation, giving the green light to proceed with full flight tests.

Sommario

Oggiorno, i velivoli a pilotaggio remoto (APR o UAV - *Unmanned Aerial Vehicles* - in inglese) rappresentano un campo di ricerca in continua crescita ed espansione, grazie ai numerosi ambiti applicativi e vantaggi economici sia in campo civile che militare: consegna di pacchi, riprese aeree, ricerca e soccorso, ricognizione e ispezione sono solo alcuni esempi. La maggiormente diffusa configurazione multi rotore è stata studiata approfonditamente e ha mostrato le sue limitazioni per quanto riguarda il tempo di volo; una delle strategie ideate per superare questa limitazione è l'unione con la configurazione ala fissa. Si parla in questo caso di droni VTOL (dall'inglese *Vertical Take Off and Landing*) in grado di combinare il decollo, l'atterraggio verticale e la capacità di hover con un'elevata efficienza e conseguenti lunghe distanze e tempi in volo tipici di velivoli convenzionali.

L'obiettivo principale di questa tesi è sviluppare e portare in volo un drone VTOL elettrico (eVTOL), progettato e costruito durante due precedenti tesi magistrali all'interno dell'*Aerospace System and Control Laboratory* (ASCL) del *Politecnico di Milano*. Nello specifico, in [1] il drone è stato progettato in ogni suo aspetto mentre in [2] è stato costruito e integrato. Il risultato è un aereo-mobile in grado di svolgere missioni sia in volo verticale che in volo avanzato; ha una massa al decollo di circa 6 kg, apertura alare di 2,25 m e un tempo di volo stimato di circa 100 minuti. È il primo ad essere completamente progettato e costruito all'interno del *Dipartimento di Scienze e Tecnologie Aerospaziali* (*Department of Aerospace Science and Technology*, DAER).

Nel dettaglio, durante la tesi sono stati risolti alcuni iniziali problemi hardware legati principalmente al sistema propulsivo; è poi stato progettato il sistema di controllo per le diverse fasi di volo: multi rotore, transizione e volo in modalità ala fissa. Il modello *Simulink* del velivolo sviluppato nei precedenti lavori è stato migliorato e il modulo di controllo è stato aggiunto, permettendo di simulare una missione completa: decollo, salita verticale, transizione al volo avanzato e volo avanzato. I controllori sviluppati sono poi stati installati a bordo dell'eVTOL per il test in volo, integrandosi nell'autopilota open-source PX4: la configurazione multirrotore è stata testata con successo in volo, permettendo poi di eseguire una campagna di identificazione del modello. Il modello identificato è stato poi inserito nel simulatore e comparato al precedente modello analitico, validando entrambi

rispetto ad una missione realmente volata. La transizione e il volo avanzato invece sono stati testati con successo in simulazione, ma non è ancora stata eseguita una prova completa in volo; sono stati infatti effettuati solo test preliminari a terra: questi esperimenti hanno confermato il corretto funzionamento del controllore e i risultati ottenuti in simulazione, dando il via libera per procedere con le prove di volo complete.

Contents

Acknowledgments	I
Abstract	III
Sommario	V
List of figures	IX
List of tables	XIII
Introduction	1
1 VTOL dynamics	7
1.1 Reference frames	7
1.2 Rotation formalism	8
1.3 Flight dynamics equations	12
1.3.1 Kinematic equations	12
1.3.2 Dynamic equations	12
1.3.3 External forces and moments	14
1.4 Multicopter linearized mathematical model	18
1.4.1 State equations	19
1.4.2 Transfer functions	20
2 Hardware upgrades	21
2.1 Aerospace Systems and Control Laboratory	21
2.2 Weight and balance	22
2.3 Propulsive system problems	25
2.3.1 Motors	25
2.3.2 Power distribution	31
2.4 Structural problems	36
2.5 Final configuration	39

3 Multicopter control	45
3.1 Stock controller	45
3.2 Multicopter controller	48
3.2.1 Multicopter simulator	49
3.3 In-simulation tuning	49
3.4 In-flight manual tuning	58
3.5 Control system performance	63
4 Multicopter dynamics identification	67
4.1 Black box identification	67
4.2 Experiments description	68
4.3 Identification	70
4.3.1 Longitudinal dynamics	71
4.3.2 Lateral dynamics	79
4.3.3 Directional and vertical dynamics	80
4.4 Updated simulator model	80
4.5 Simulator validation	81
5 Fixed-wing controller	89
5.1 Fixed-wing attitude controller	89
5.1.1 Roll and pitch control	89
5.1.2 Yaw rate control: turn coordination	90
5.1.3 Simulations and controller evaluation	91
5.2 Total energy control system (TECS)	92
5.2.1 Controller algorithm	94
5.2.2 Controller input and output	99
5.2.3 Controller tuning	100
5.2.4 Controller evaluation	100
6 Transition controller	109
6.1 Transition	109
6.1.1 Selected strategy	110
6.1.2 Goals	110
6.2 Implementation	111
6.2.1 Simulation results	112
6.2.2 Analysis	114
6.3 Back transition	118
6.4 Mission management and indoor testing	120
Conclusions	125
A Flight modes	131
A.1 Multicopter flight modes	131
A.2 Fixed-wing flight modes	134

List of Figures

1	Example of VTOL UAV, source [8].	1
2	eVTOL UAV developed at <i>Politecnico di Milano</i> , source [2].	2
3	Technical drawings of the eVTOL UAV, scale 1:10. The measurements are given in mm.	3
1.1	Reference frames.	8
2.1	Flying Arena for Rotorcraft Technologies (Fly-ART).	22
2.2	Motion Capture System.	23
2.3	New balsa wood tail.	24
2.4	Test at motor test bench of the motor for vertical flight <i>KDE 2315 XF – 2050</i> , 5x4.5 inch, 2 blades bullnose propeller, DC power supply, from [2].	26
2.5	Thrust against throttle and current against throttle, motor for vertical flight <i>KDE 2315 XF – 2050</i> , 5x4.5 inch, 2 blades bullnose propeller, powered with 16,8 V battery.	27
2.6	Thrust against throttle: comparison between different propellers, vertical flight motor <i>KDE 2315 XF – 2050</i> , powered with standard battery.	28
2.7	Thrust against throttle and current against throttle (for the entire propulsive system): motor for vertical flight <i>KDE 2315 XF – 2050</i> , 7x4.2 propeller, powered with standard battery.	29
2.8	Angular velocity against throttle: motor for vertical flight <i>KDE 2315 XF – 2050</i> , 7x4.2 propeller, powered with standard battery.	30
2.9	Battery data time history during second test flight: motor <i>KDE 2315 XF – 2050</i> , 7x4.2 propeller, powered with 4S battery, 100% SoC at the start of the test.	31
2.10	Thrust and current comparison between KDE and T-MOTOR propulsion systems, 7x4.2 propeller, powered with 4S battery.	34
2.11	Front fuselage part with double battery and second PDB installed.	35
2.12	Current and voltage time histories during an endurance test with double PDB and battery.	36
2.13	Front motor booms modification.	37
2.14	Time history of yaw angle and normalized yaw control moment.	37

2.15	Motors forces during a yaw maneuver with original configuration of propellers.	38
2.16	Aircraft top view, with relevant dimensions named, propellers numbering and propellers spinning directions.	39
2.17	Fuselage reinforcement with a carbon fiber plate.	40
2.18	Modification of the wing locking mechanism.	40
2.19	Final configuration of the VTOL.	42
3.1	Oscillation of roll angle ϕ and pitch angle θ ; the divergence in the pitch axis is clearly visible.	46
3.2	Position and pitch angle θ during a move-forward maneuver.	46
3.3	Multicopter controller.	48
3.4	<i>Simulink</i> multicopter controller.	50
3.5	<i>Simulink</i> position control block.	51
3.6	<i>Simulink</i> attitude control block.	52
3.7	<i>Simulink</i> multicopter simulator.	53
3.8	<i>Simulink</i> state filter block.	54
3.9	Simulated step responses with controllers tuned in simulation.	56
3.10	PWM motors command during the flight test with the controller gains obtained in simulation.	57
3.11	Yaw rate, comparison between initial and final phase of the tuning.	60
3.12	Pitch rate, comparison between initial and final phase of the tuning.	61
3.13	Roll rate, effect of an increase of roll angle proportional gain on noise.	62
3.14	PSD of rate measurements.	62
3.15	PSD of roll rate measurements, before and after filtering.	63
3.16	Notch filter magnitude Bode diagram.	64
3.17	PSD of roll rate measurements of a flight with notch filter installed.	64
3.18	Attitude angles during an hovering test.	65
4.1	Data time-histories (pitch angle θ , roll angle ϕ , pitch rate q and roll rate p) of longitudinal dynamics validation fight test; a suitable time-window is chosen where the lateral quantities are small.	69
4.2	Excitation signal, total input command L_{tot} and roll rate p during an identification test.	71
4.3	Time-domain validation for longitudinal model with $n = 2$ and $p = f = 30$	73
4.4	VAF index for model order $n = 6$ and increasing horizon parameter p and f	74
4.5	Frequency response of the non-parametric estimate, Model 1, Model 2 and Model 3.	75
4.6	Coherence function of non-parametric frequency response function estimate.	76

4.7	Excitation signal, total input command M_{tot} and pitch rate q during an identification test with frequency sweep excitation signal.	76
4.8	Frequency response of the non-parametric estimate, Model 4, Model 5, Model 6 and Model 7.	77
4.9	Time-domain validation for Model 4, longitudinal dynamics.	78
4.10	Time-domain validation for lateral dynamics on PRBS dataset.	79
4.11	Singular values decomposition; a gap can be spotted between the first three values and the others.	80
4.12	<i>Simulink</i> VTOL model with identified dynamics.	82
4.13	<i>Simulink</i> VTOL simulator with identified dynamics.	83
4.14	Position measurements.	85
4.15	Velocity measurements.	85
4.16	Attitude measurements.	86
4.17	Angular rates measurements.	86
5.1	Fixed-wing attitude control architecture: ω is the body rates vector, δ the control surfaces deflections vector ($\delta = [\delta_a, \delta_e, \delta_r]$) and V the airspeed.	90
5.2	Forces during a turn, from [35].	91
5.3	<i>Simulink</i> fixed-wing attitude controller.	93
5.4	Pitot tube airspeed measurement during on-ground testing.	94
5.5	TECS algorithm structure.	96
5.6	<i>Simulink</i> TECS model: core algorithm and outer loop.	97
5.7	<i>Simulink</i> $TECS_m$ model: core algorithm and outer loop.	98
5.8	Simulation of a 2 m/s speed increase: physical quantities.	102
5.9	Simulation of a 2 m/s speed decrease: physical quantities.	103
5.10	Simulation of a 10 m climb manoeuvre: physical quantities.	104
5.11	Simulation of a 10 m descent manoeuvre: physical quantities.	105
5.12	Simulation of a combined manoeuvre: 5 m climb and 1 m/s speed decrease.	106
5.13	Simulation of a combined manoeuvre: 5 m descent and 1 m/s speed increase.	106
5.14	Trim recover simulation: physical quantities.	108
6.1	Scaling factors.	112
6.2	Height and airspeed during transition for TECS and $TECS_m$ controllers.	113
6.3	Vertical forces during transition.	114
6.4	Pitching moments during transition.	115
6.5	Horizontal position during transition.	115
6.6	Elevator deflection and forward motors throttle during transition.	116
6.7	Elevator deflection during transition: action A activated and deactivated.	117

6.8	Pitch angle during transition: action A activated and deactivated.	117
6.9	Height and airspeed during transition with scaling factor K_{PITCH_m} .	119
6.10	Vertical forces during transition with scaling factor K_{PITCH_m} .	119
6.11	Pitch angle during transition: with K_{PITCH} and K_{PITCH_m} .	120
6.12	VTOL mission. Vertical take off, transition and fixed-wing phase.	122
6.13	Flight modes and states switches during transition phase.	123
6.14	Forward velocity and position during transition phase.	123
6.15	Pitch angle during transition phase.	124
A.1	FrSky Taranis X9D remote controller ([41]).	132
A.2	Multicopter controller.	134
A.3	Fixed-wing controller.	135

List of Tables

2.1	Aircraft mass, position of center of gravity and neutral point calculated in design phase ([1]). Being the axis from the tail to the nose, a negative x value means that the point is behind the wing leading edge.	23
2.2	Comparison between the old (3D printed) and the new (wood) tails.	25
2.3	Motor static coefficients comparison, motor for vertical flight <i>KDE 2315 XF–2050</i> , 5x4.5 inch, 2 blades bullnose propeller, from [2].	25
2.4	Test result for different propellers with vertical propulsion system.	29
2.5	Motor static coefficients and time constant; motor for vertical flight <i>KDE 2315 XF – 2050</i> , 7x4.2 propeller.	29
2.6	Angular velocity against throttle quadratic model's coefficients.	30
2.7	Mass of considered motors and ESC.	32
2.8	Total mass of the drone and variation of x_{CG} for different propulsive system.	33
2.9	Current and throttle comparison between KDE and T-MOTOR propulsion systems.	33
2.10	Final batteries characteristics (specifications of single battery shown).	35
2.11	Aircraft mass, position of center of gravity and neutral point of the final configuration of the VTOL. Position measured form the wing leading edge along the b1 body axis.	41
2.12	Eigenvalues of the aircraft's dynamic modes during the forward fight phase at cruise speed ($V = 15\text{m/s}$), previous model from [2] and improved model.	42
2.13	Frequency and damping of the aircraft's dynamic modes during the forward fight phase at cruise speed ($V = 15\text{m/s}$), previous model from [2] and improved model.	43
3.1	Multicopter controller gains, from tuning in simulation.	55
3.2	Multicopter controller gains, from in-flight tuning.	59
3.3	Notch filter parameters.	63
3.4	Multicopter controller valuation.	66
4.1	PRBS excitation signals.	70

4.2	Frequency sweep excitation signals.	70
4.3	Different model structures for longitudinal dynamics obtained with PRBS experiment.	72
4.4	Different longitudinal models obtained with frequency sweep experiment.	77
4.5	Lateral dynamics model and VAF results.	79
4.6	Directional and vertical dynamics models and VAF_{PRBS} results. .	80
4.7	VAF values of old and new simulator compared to a real flight. . .	87
5.1	Maximum measured surfaces deflections.	91
5.2	TECS gains.	100
5.3	$TECS_m$ gains.	100
5.4	Outer loop gains.	100
5.5	Airspeed and altitude loss during a trim recover simulation. . . .	107
6.1	Transition performance comparison.	113
6.2	VTOL mission states.	121
6.3	States assignment logic.	121
A.1	Radio commands for multicopter flight modes.	133
A.2	Radio commands for different fixed-wing flight modes.	134

Introduction

The first thing that people think to when they listen to the word *drone* is usually a multicopter drone, generally a quadrotor. These vehicles are wide spread, easy to fly and not so expensive. However, they do not represent the only adopted drone configuration: given the limited flight time of multicopter drones (in most cases less than an hour), they are not suitable for long endurance missions such as surveillance and reconnaissance or long range delivery. Fixed wing unmanned aerial vehicles (UAVs) may represent the best option for these missions, given the better efficiency of this configuration. A runway for take-off and a system to land (or conventionally with a runway or with a net or a hook and cable system) is nevertheless required.

Engineers came up with a configuration that overlaps the pros of both multicopter and fixed wing UAVs: the vertical take-off and landing (VTOL) configuration. There is no need for a runway since the drone can take-off and land vertically, it can perform hovering and can cover long ranges due to the wings. The interest in these aircraft is growing rapidly, both in the civil and military fields as attested in [3], [4], [5], [6] and [7]. An example of VTOL UAV is shown in Figure 1.



Figure 1: Example of VTOL UAV, source [8].



Figure 2: eVTOL UAV developed at *Politecnico di Milano*, source [2].

Background

This thesis represents the third part in the development of a VTOL UAV designed and built at *Politecnico di Milano, Department of Aerospace Science and Technology* (DAER). The initial design from the basic requirements has been carried out in [1] while the production and integration of the components, together with development of a simulator, have been performed in [2]. This second thesis is the starting point for the present work: the aircraft, shown in Figure 2, is assembled and ready for the first flight tests and the development of the flight control system. The aircraft is an electric VTOL (eVTOL) powered by a 8500 mAh LiPo battery that guarantees around 100 minutes of flight time; it has eight electrical motors for vertical flight and two for forward flight. It has a span of 2.25 m and its mass is 4.8 kg. A technical representation of the aircraft is shown in Figure 3.

Thesis objectives

This thesis has two main objectives; the first one is to develop the control system for the drone in all its flight modes: multicopter mode, fixed-wing mode and transition from one to the other (in both directions). This activity is based both on the simulator developed in [1] and [2] and on flight experiments performed in the *Aerospace System and Control Laboratory* (ASCL) of DAER. The second objective is to test the aircraft in flight and to improve the mathematical model already developed in the previous works: an identification campaign is planned to build reliable models of the VTOL dynamics in multirotor flight mode. Moreover,

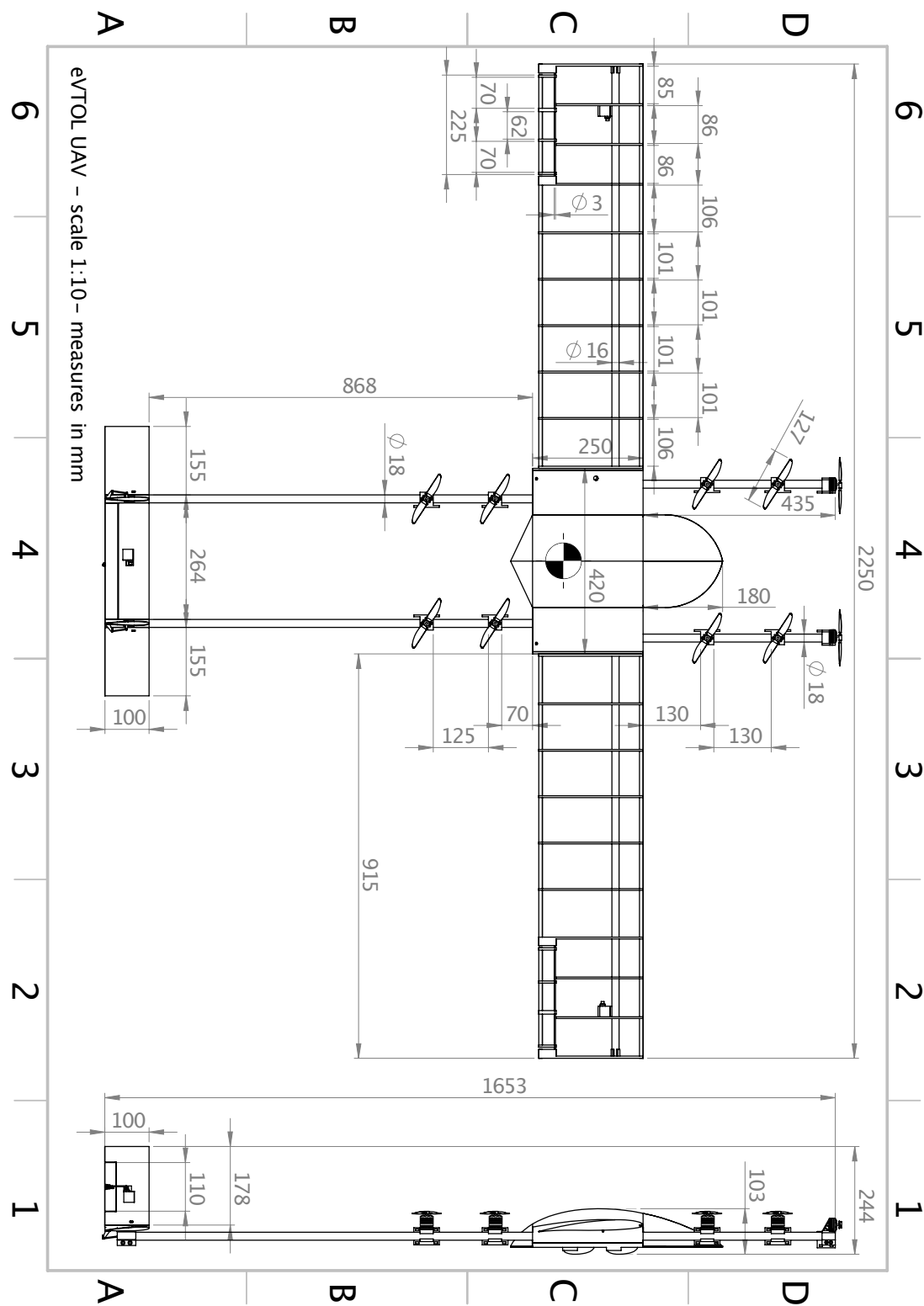


Figure 3: Technical drawings of the eVTOL UAV, scale 1:10. The measurements are given in mm.

the transition process from one flight mode to the other is studied with the aim to test it in the ASCL facility. It is worth mentioning that, being an experimental activity, some problems may arise modifying the expected workflow; thus, some hardware and/or software modifications to the initial design may be required.

Structure of the thesis

The thesis is organized as follows:

- in Chapter 1 the dynamics model of the aircraft is derived for all its modes of operation, focusing on the different forces acting in each flight regime. Then the linearized equations of motion of a multicopter UAV are introduced.
- Chapter 2 presents the results of the first flights performed with VTOL, the identified problems related to weight and balance, propulsion and structure. Several options to solve each problem are identified and compared, evaluating the possible impact on the aircraft and the development costs. In the end the characteristics of the updated UAV are listed.
- Chapter 3 is devoted to the control of multicopter mode: a cascade loops control architecture is adopted; the inner loop controls attitude and angular rate while the outer one controls position and velocity. The tuning procedure adopted, made up of an in simulation phase and an in flight one, is presented. The results obtained are evaluated both in flight and in terms of phase and gain margins.
- Chapter 4 presents the identification of the multicopter dynamics using a black box approach; the main focus is the dynamic response to control actions of roll, pitch, yaw axes and vertical motion. Then, the different inputs used to increase the accuracy of the model at low frequencies are presented; several model have been developed and are then compared between them and validated against a flight experiment.
- In Chapter 5 the control of the fixed wing mode is presented. Also in this case a cascade architecture is used: the inner controller is related to the attitude while the outer one to the control of altitude and airspeed; in this case the total energy control system (TECS) is adopted and developed in two versions to identify the best one to be used also during the transition phase.
- Chapter 6 presents the control of the transition process from multicopter mode to fixed-wing mode. The adopted strategy is presented with a particular focus on the mixing of the control outputs produced by the multicopter and fixed-wing controllers. The results obtained in simulation are shown;

only initial flight tests have been performed indoor. Fundamentals of back transition from fixed-wing mode to multicopter mode are introduced.

Chapter 1

VTOL dynamics

In this Chapter the conventions, the notation and the model that describes the dynamics of a VTOL are briefly described. The first section is related to the reference frames adopted, the second one to the rotation formalism used to rotate vectors from one reference frame to another, the third section shows the dynamics equations of the VTOL while the last one the linearized equations of motion of the multirotor flight mode.

1.1 Reference frames

In order to describe the motion of a flying vehicle it is important to define the reference frames needed in the derivation of the equations of motion; since the UAV flies near ground, both indoor and outdoor, the Earth is assumed flat and non-rotating. The reference frames defined in the following are presented in Figure 1.1.

Navigation frame $\bar{\mathcal{N}}$

The navigation frame has origin in a generic point O_N on Earth's surface. The first unit vector $\bar{\mathbf{n}}_1$ is directed towards the local North pole, $\bar{\mathbf{n}}_2$ points towards the local East and $\bar{\mathbf{n}}_3$ is aligned with the direction of gravity, pointing downward. With the hypothesis of flat and non-rotating Earth, the $\bar{\mathcal{N}}$ frame can be considered as an inertial frame.

Local vertical reference frame (NED) \mathcal{N}

The local vertical reference frame (or NED, North-East-Down frame) has origin in the centre of gravity of the aircraft; \mathbf{n}_1 points to the local North pole, \mathbf{n}_2 is aligned with the local East and \mathbf{n}_3 points to the centre of the Earth.

Body frame \mathcal{B}

The body frame has origin in the centre of gravity of the aircraft; the unit vector \mathbf{b}_1 lies in the plane of symmetry of the vehicle and points forward, \mathbf{b}_2 is normal to the plane of symmetry pointing rightward and \mathbf{b}_3 points downward.

Wind frame \mathcal{W}

The wind frame has origin in the centre of gravity of the aircraft. The unit vector \mathbf{w}_1 is aligned with the relative wind speed, with a positive verse in the direction of motion, \mathbf{w}_3 lies within the aircraft's longitudinal plane of symmetry and is perpendicular to \mathbf{w}_1 , pointing downwards; \mathbf{w}_2 forms a right-hand triad with \mathbf{w}_1 and \mathbf{w}_3 .

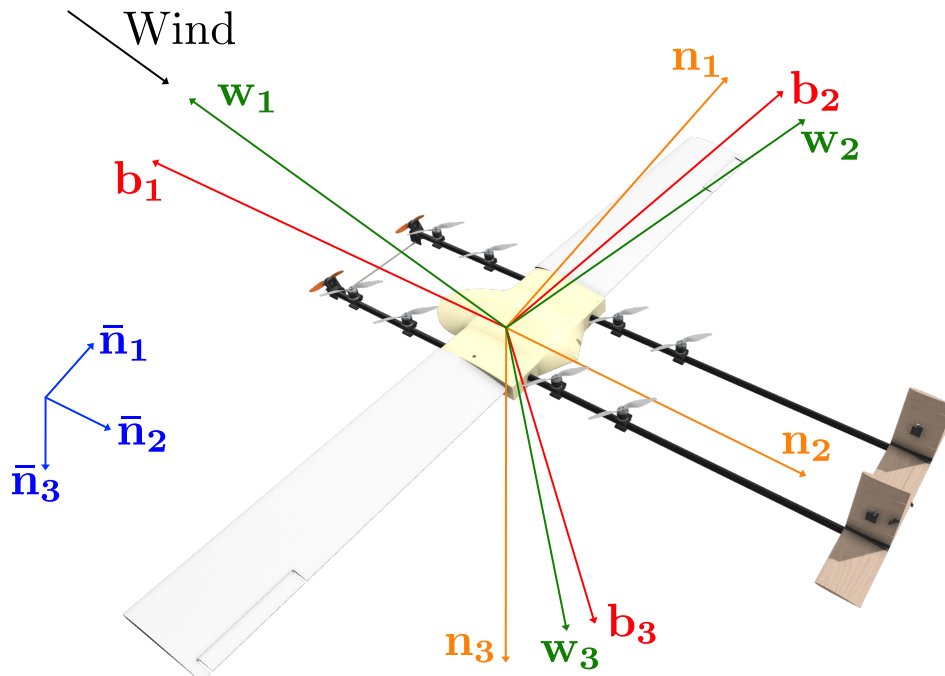


Figure 1.1: Reference frames.

1.2 Rotation formalism

Euler angles

The Euler angles (called roll ϕ , pitch θ and yaw ψ) are three independent angular quantities able to describe the 3D orientation of an object, using two sets of

reference frames: an inertial Earth-fixed one and a body one, rigidly attached to the object. The Euler angles define the transformation of the components of a generic vector between two sets of axes. A vector v_A in the initial reference frame A can be rotated into the reference frame B obtaining v_B , with the rotation matrix R_A^B :

$$v_B = R_A^B v_A. \quad (1.1)$$

Any arbitrary attitude is obtained by an ordered sequence of three consecutive rotations around each axis of an orthogonal frame; the rotation around the x axis can be described with matrix $R_x(\phi)$

$$R_x(\phi) = \begin{bmatrix} 1 & 0 & 0 \\ 0 & \cos \phi & \sin \phi \\ 0 & -\sin \phi & \cos \phi \end{bmatrix}, \quad (1.2)$$

while, in similar fashion the rotation around y and z are described respectively with rotation matrices $R_y(\theta)$, $R_z(\psi)$:

$$R_y(\theta) = \begin{bmatrix} \cos \theta & 0 & -\sin \theta \\ 0 & 1 & 0 \\ \sin \theta & 0 & \cos \theta \end{bmatrix}, \quad (1.3)$$

$$R_z(\psi) = \begin{bmatrix} \cos \psi & \sin \psi & 0 \\ -\sin \psi & \cos \psi & 0 \\ 0 & 0 & 1 \end{bmatrix} \quad (1.4)$$

In aircraft dynamics the generic attitude of the vehicle is obtained by the so-called rotation sequence 321: the attitude of the body axes \mathcal{B} (always aligned with the aircraft) with respect to a non-rotating NED \mathcal{N} reference frame, is obtained by a first rotation about the z axis of an angle ψ , then a rotation about the y axis of an angle θ , and finally a rotation about the x axes of an angle ϕ . The final rotation matrix from \mathcal{N} to \mathcal{B} is obtained by the ordered multiplication of the previous rotation matrices (equations (1.2), (1.3) and (1.4)); it is called Euler rotation matrix and has the following expression:

$$T_N^B(\phi, \theta, \psi) = \begin{bmatrix} C_\theta C_\psi & C_\theta S_\psi & -S_\theta \\ S_\phi S_\theta C_\psi - C_\phi S_\psi & S_\phi S_\theta S_\psi + C_\phi C_\psi & S_\phi C_\theta \\ C_\phi S_\theta C_\psi - S_\phi S_\psi & C_\phi S_\theta S_\psi - S_\phi C_\psi & C_\phi C_\theta \end{bmatrix}, \quad (1.5)$$

where $C_\alpha = \cos(\alpha)$ and $S_\alpha = \sin(\alpha)$ for the sake of brevity.

The roll angle ϕ , the pitch angle θ and the yaw angle ψ are grouped in the vector α_e , which uniquely describes the aircraft's attitude in space with respect to the NED reference frame \mathcal{N} .

$$\alpha_e = \begin{bmatrix} \phi \\ \theta \\ \psi \end{bmatrix}. \quad (1.6)$$

Time derivatives of Euler angles

The attitude of an aircraft changes with time when the aircraft manoeuvres. The Euler angle rates are function of the Euler angles and body-axis angular rates. The components of the angular velocity measured in body frame ω_B are the roll rate p , pitch rate q and yaw rate r :

$$\omega_B = \begin{bmatrix} p \\ q \\ r \end{bmatrix}. \quad (1.7)$$

The rate of change of Euler angles is related to ω_B by the following equation:

$$\dot{\alpha}_e = E^{-1}\omega_B, \quad (1.8)$$

with E^{-1} being the inverse of matrix E , whose expressions are given by:

$$E(\phi, \theta) = \begin{bmatrix} 1 & 0 & -\sin \theta \\ 0 & \cos \phi & \cos \theta \sin \phi \\ 0 & -\sin \phi & \cos \theta \cos \phi \end{bmatrix}, E^{-1}(\phi, \theta) = \begin{bmatrix} 1 & \sin \phi \tan \theta & \cos \phi \tan \theta \\ 0 & \cos \phi & -\sin \phi \\ 0 & \sin \phi / \cos \theta & \cos \phi / \cos \theta \end{bmatrix}. \quad (1.9)$$

It can be seen that matrix E is singular for pitch angles of $\pm 90^\circ$; this singularity is called gimbal lock and can be avoided using quaternions.

Quaternions

A quaternion q is a parametrisation of the four-dimensional unit sphere that can be used to represent the orientation of a rigid body or a coordinate frame in three-dimensional space ([9]):

$$q = \begin{bmatrix} q_0 \\ q_1 \\ q_2 \\ q_3 \end{bmatrix}, \quad \|q\| = 1. \quad (1.10)$$

The quaternion elements generate the following rotation matrix (the analogous of the one expressed in equation (1.5) in terms of Euler angles):

$$T_N^B = \begin{bmatrix} q_0^2 + q_1^2 - q_2^2 - q_3^2 & 2(q_1 q_2 + q_0 q_3) & 2(q_1 q_3 - q_0 q_2) \\ 2(q_1 q_2 - q_0 q_3) & q_0^2 - q_1^2 + q_2^2 - q_3^2 & 2(q_2 q_3 + q_0 q_1) \\ 2(q_1 q_3 + q_0 q_2) & 2(q_2 q_3 - q_0 q_1) & q_0^2 - q_1^2 - q_2^2 + q_3^2 \end{bmatrix}. \quad (1.11)$$

The Euler angles ϕ, θ and ψ can be obtained from the element of the quaternion expressing the aircraft's orientation with respect to a non-rotating frame through

these equations:

$$\begin{aligned}\phi &= \tan^{-1} \left(\frac{2q_3q_4 - 2q_1q_2}{2q_1^2 - 1 + 2q_4^2} \right), \\ \theta &= -\sin^{-1} (2q_2q_4 + 2q_1q_3), \\ \psi &= \tan^{-1} \left(\frac{2q_2q_3 - 2q_1q_4}{2q_1^2 - 1 + 2q_2^2} \right).\end{aligned}\quad (1.12)$$

The quaternion conjugate, denoted by $(\cdot)^*$, can be used to swap the frames described by an orientation. To follow the previous example, the orientation of frame B with respect to frame A can be described by the quaternion q_{AB} , and its conjugate q_{AB}^* describes the orientation of frame A relative to frame B (q_{BA}), like in the following equation:

$$q_{AB}^* = q_{BA} = \begin{bmatrix} q_0 \\ -q_1 \\ -q_2 \\ -q_3 \end{bmatrix}. \quad (1.13)$$

The quaternion product, denoted as (\otimes) , is used to describe successive rotations and can be determined using the Hamilton rule, as expressed by equation (1.14). The quaternion product is not commutative.

$$q_{AC} = q_{BC} \otimes q_{AB} = \begin{bmatrix} a_0 \\ a_1 \\ a_2 \\ a_3 \end{bmatrix} \otimes \begin{bmatrix} b_0 \\ b_1 \\ b_2 \\ b_3 \end{bmatrix} = \begin{bmatrix} a_1b_1 - a_2b_2 - a_3b_3 - a_4b_4 \\ a_1b_2 + a_2b_1 + a_3b_4 - a_4b_3 \\ a_1b_3 - a_2b_4 + a_3b_1 + a_4b_2 \\ a_1b_4 + a_2b_3 - a_3b_2 + a_4b_1 \end{bmatrix}. \quad (1.14)$$

A three dimensional vector can be rotated by a quaternion using equation (1.15) and by appending a zero as a first element of the vector, to make it dimensionally consistent with quaternions:

$$v_B = q_{AB} \otimes v_A \otimes q_{AB}^*, \quad (1.15)$$

where v_A and v_B are the same vector described in frame A and frame B respectively.

Finally, the quaternion derivative describing the the rate of change of orientation of the Earth frame relative to the body frame can be calculated by the equation:

$$\dot{q}_{BE} = \frac{1}{2}q_{BE} \otimes \omega \quad \text{where } \omega = \begin{bmatrix} 0 \\ \omega_B \end{bmatrix}. \quad (1.16)$$

Resolving equation (1.16) leads to

$$\begin{bmatrix} \dot{q}_1 \\ \dot{q}_2 \\ \dot{q}_3 \\ \dot{q}_4 \end{bmatrix} = \frac{1}{2} \begin{bmatrix} 0 & -p & -q & -r \\ p & 0 & r & -q \\ q & -r & 0 & p \\ r & q & -p & 0 \end{bmatrix} \begin{bmatrix} q_1 \\ q_2 \\ q_3 \\ q_4 \end{bmatrix}. \quad (1.17)$$

1.3 Flight dynamics equations

1.3.1 Kinematic equations

Considering a generic inertial frame \mathcal{I} and the non-inertial body frame \mathcal{B} , and using the convention that the velocity (or acceleration) of a point P with respect to a frame \mathcal{I} is written as $v_{P/\mathcal{I}}$, the velocity of a generic point Q belonging to the aircraft, measured with respect to the inertial frame \mathcal{I} can be expressed as

$$v_{Q/\mathcal{I}} = v_{P/\mathcal{I}} + \boldsymbol{\omega}_{\mathcal{B}/\mathcal{I}} \times r_{PQ}, \quad (1.18)$$

where point P is another generic point belonging to the aircraft, and r_{PQ} is the vector between point P and Q .

The acceleration of point Q measured in the inertial frame \mathcal{I} is found computing the derivative of equation (1.18) with respect to time:

$$a_{Q/\mathcal{I}} = \frac{\mathcal{I}d v_{Q/\mathcal{I}}}{dt} = \frac{\mathcal{I}d v_{P/\mathcal{I}}}{dt} + \frac{\mathcal{I}d \boldsymbol{\omega}_{\mathcal{B}/\mathcal{I}}}{dt} \times r_{PQ} + \boldsymbol{\omega}_{\mathcal{B}/\mathcal{I}} \times \frac{\mathcal{I}d r_{PQ}}{dt}, \quad (1.19)$$

where $\frac{\mathcal{I}d(\cdot)}{dt}$ represents the derivative of (\cdot) in the reference frame \mathcal{I} . By expressing the derivatives in body frame \mathcal{B} usign the moving axes theorem¹ and assuming that the aircraft is a rigid body one gets

$$a_{Q/\mathcal{I}} = \frac{\mathcal{B}d v_{P/\mathcal{I}}}{dt} + \boldsymbol{\omega}_{\mathcal{B}/\mathcal{I}} \times v_{P/\mathcal{I}} + \frac{\mathcal{B}d \boldsymbol{\omega}_{\mathcal{B}/\mathcal{I}}}{dt} \times r_{PQ} + \boldsymbol{\omega}_{\mathcal{B}/\mathcal{I}} \times (\boldsymbol{\omega}_{\mathcal{B}/\mathcal{I}} \times r_{PQ}). \quad (1.20)$$

1.3.2 Dynamic equations

Translational motion

By integrating the *first cardinal equation* for a particle of mass dm located in a generic point Q over the whole aircraft volume \mathcal{V} , one gets the equation for translational motion for the whole aircraft:

$$\int_{\mathcal{V}} dF_Q = \int_{\mathcal{V}} a_{Q/\mathcal{I}} dm. \quad (1.21)$$

By substituting equation (1.20) into (1.21), one gets the sum of all the external forces F acting on the aircraft

$$F = \int_{\mathcal{V}} \left[\frac{\mathcal{B}d v_{P/\mathcal{I}}}{dt} + \boldsymbol{\omega}_{\mathcal{B}/\mathcal{I}} \times v_{P/\mathcal{I}} + \frac{\mathcal{B}d \boldsymbol{\omega}_{\mathcal{B}/\mathcal{I}}}{dt} \times r_{PQ} + \boldsymbol{\omega}_{\mathcal{B}/\mathcal{I}} \times (\boldsymbol{\omega}_{\mathcal{B}/\mathcal{I}} \times r_{PQ}) \right] dm. \quad (1.22)$$

¹The moving axes theorem states that for any two frames of reference \mathcal{I} and \mathcal{J} , using the notation previously introduced, for any generic vector b the following holds true:

$$\frac{\mathcal{I}db}{dt} = \frac{\mathcal{J}db}{dt} + \boldsymbol{\omega}_{\mathcal{J}/\mathcal{I}} \times b.$$

By taking point P coincident with the center of gravity G of the aircraft several terms cancel out, leading to

$$F = m \dot{v}_G + \boldsymbol{\omega} \times m v_G, \quad (1.23)$$

with v_G the velocity of the center of gravity measured with respect to the inertial frame, $\boldsymbol{\omega}$ the angular velocity measured in the inertial frame and m the total mass of the aircraft, calculated as:

$$m = \int_{\mathcal{V}} dm. \quad (1.24)$$

Rotational motion

The *second cardinal equation* states that, for a particle of mass located in point Q , with moments taken with respect to point P , the following equation holds true:

$$dM_P = r_{PQ} \times dF_Q = dm r_{PQ} \times a_{Q/\mathcal{I}}. \quad (1.25)$$

Integrating equation (1.25) over the entire aircraft's volume \mathcal{V} , and substituting the expression of $a_{Q/\mathcal{I}}$ (equation (1.20)) leads to

$$M_P = \int_{\mathcal{V}} dm r_{PQ} \times \left[\frac{\mathcal{B} dv_{P/\mathcal{I}}}{dt} - r_{PQ} \times \frac{\mathcal{B} d\boldsymbol{\omega}_{\mathcal{B}/\mathcal{I}}}{dt} + \boldsymbol{\omega}_{\mathcal{B}/\mathcal{I}} \times (v_{P/\mathcal{I}} - r_{PQ} \times \boldsymbol{\omega}_{\mathcal{B}/\mathcal{I}}) \right]. \quad (1.26)$$

By considering, as said, P coincident with G , one gets

$$M_G = J_G \dot{\boldsymbol{\omega}} + \boldsymbol{\omega} \times J_G \boldsymbol{\omega}, \quad (1.27)$$

where $\boldsymbol{\omega}$ is the angular velocity measured in the inertial frame and J the inertia matrix, defined as follow:

$$J_G = \begin{bmatrix} J_{xx} & -J_{xy} & -J_{xz} \\ -J_{xy} & J_{yy} & -J_{yz} \\ -J_{xz} & -J_{yz} & J_{zz} \end{bmatrix}, \quad (1.28)$$

where

$$\begin{aligned} J_{xx} &= \int_{\mathcal{V}} (y^2 + z^2) dm, & J_{yy} &= \int_{\mathcal{V}} (x^2 + z^2) dm, & J_{zz} &= \int_{\mathcal{V}} (x^2 + y^2) dm, \\ J_{xy} &= \int_{\mathcal{V}} (xy) dm, & J_{xz} &= \int_{\mathcal{V}} (xz) dm, & J_{yz} &= \int_{\mathcal{V}} (yz) dm. \end{aligned}$$

Hence, the 6 degrees of freedom equations of motion with respect to the centre of gravity are as follows:

$$\begin{cases} F = m \dot{v}_G + \boldsymbol{\omega} \times m v_G \\ M_G = J_G \dot{\boldsymbol{\omega}} + \boldsymbol{\omega} \times J_G \boldsymbol{\omega}. \end{cases} \quad (1.29)$$

It is important to remark that, since no assumption on the flight mode of the aircraft (multicopter, transition flight and fixed wing) has been made, equation (1.29) is true for all modes. The difference between a flight mode and the other is related to external forces and moments which act on the vehicle, that will be defined in the next Section.

1.3.3 External forces and moments

For all the three flight modes, the forces and moments which act on the VTOL are of gravitational, aerodynamic and propulsive type:

$$\begin{cases} F^B = F_{Grav}^B + F_{Aero}^B + F_{Prop}^B \\ M_G^B = M_{G_{Grav}}^B + M_{G_{Aero}}^B + M_{G_{Prop}}^B. \end{cases} \quad (1.30)$$

Common to all flight modes

Gravitational forces and moments

Gravity force is directed downward along the D direction of the NED frame, so it must be projected on the body axes:

$$F_{Grav}^B = T_N^B(\phi, \theta, \psi) \begin{bmatrix} 0 \\ 0 \\ mg \end{bmatrix}. \quad (1.31)$$

By definition of centre of gravity, the moment due to the gravitational force about this point is null:

$$M_{G_{Grav}}^B = 0. \quad (1.32)$$

Multirotor mode

Aerodynamic forces and moments

The main contributions are the aerodynamic drag coming from the wing, fuselage and tail and the aerodynamic damping caused by rotating propellers moving through the air.

Aerodynamic drag

The overall aerodynamic drag force in body axes is given by

$$\mathbf{F}_{Drag}^B = \begin{bmatrix} 0 \\ D_{VTail} \\ D_{Wing} + D_{Fus} + D_{HTail} \end{bmatrix}, \quad (1.33)$$

where:

$$\begin{aligned} D_{Wing} &= -sgn(w_{Wing}) \frac{1}{2} \rho w_{Wing}^2 S_{Wing} C_{D_{Wing}}, \\ D_{Fus} &= -sgn(w_{Fus}) \frac{1}{2} \rho w_{Fus}^2 S_{Fus} C_{D_{Fus}}, \\ D_{HTail} &= -sgn(w_{HTail}) \frac{1}{2} \rho w_{HTail}^2 S_{HTail} C_{D_{HTail}}, \\ D_{VTail} &= -sgn(v_{VTail}) \frac{1}{2} \rho v_{VTail}^2 S_{VTail} C_{D_{VTail}}, \end{aligned} \quad (1.34)$$

where D indicates the drag, w and v the vertical and lateral velocity, S the surface and c_D the drag coefficient respectively of wing, fuselage, horizontal and vertical tails. The moment produced by the drag force on each single surface is obtained as:

$$M_{G_{Drag_i}}^B = r_{CG-CP_i}^B \times D_i^B, \quad (1.35)$$

where $r_{CG-CP_i}^B$ is the vector from the center of gravity to the center of pressure of the i -th surface. The total moment is obtained by summing up the moment contributions from all surfaces:

$$M_{G_{Drag}}^B = M_{G_{DragWing}}^B + M_{G_{DragFus}}^B + M_{G_{DragHTail}}^B + M_{G_{DragVTail}}^B. \quad (1.36)$$

Aerodynamic damping

Only aerodynamic damping proportional to $\omega_b = [p \ q \ r]^T$ is considered. Another important approximation is to consider the moments relative to an axis only proportional to the rotational speed around that axis (decoupled moments) ([10]):

$$M_{G_{Damp}}^B = \begin{bmatrix} \frac{\partial M_x}{\partial p} & 0 & 0 \\ 0 & \frac{\partial M_y}{\partial q} & 0 \\ 0 & 0 & \frac{\partial M_z}{\partial r} \end{bmatrix} \begin{bmatrix} p \\ q \\ r \end{bmatrix}. \quad (1.37)$$

The stability derivatives $\frac{\partial M_x}{\partial p}$, $\frac{\partial M_y}{\partial q}$ and $\frac{\partial M_z}{\partial r}$ have an analytical form, which is taken from helicopter dynamics background (see [11], [12]). As a rough approximation, the derivatives $\frac{\partial M_x}{\partial p}$ and $\frac{\partial M_y}{\partial q}$ can be considered to be equal, due to the VTOL's geometry, and have the following expression:

$$\frac{\partial M_x}{\partial p} = -4\rho A R^2 \Omega^2 \frac{\partial C_T}{\partial p} \frac{b}{\sqrt{2}}, \quad \frac{\partial C_T}{\partial p} = \frac{C_{L_\alpha}}{8} \frac{\sigma}{R\Omega} \frac{b}{\sqrt{2}}, \quad (1.38)$$

where σ is the solidity ratio, defined as the ratio between the total blade area A_b and the disk area A . The lift coefficient derived with respect to the angle of attack $C_{L\alpha}$ of the propeller can be approximated as being equal to 2π , from the results of analytical aerodynamics, since no accurate geometric data is known for the propeller. Note that, due to the fact that not all propellers have the same distance from the centre of gravity, the value of $\frac{\partial M_x}{\partial p}$ is an approximation, which however has a negligible impact, since the difference in distance is small. Finally, due to the small rotational speed around the z axis compared to the other axis, the derivative $\frac{\partial M_z}{\partial r}$ can be neglected.

Propulsive forces and moments

Each of the propellers exerts a thrust and torque proportional to the square of the angular velocity:

$$T_i = K_T \Omega_i^2, \quad K_T = C_T \rho A R^2, \quad (1.39)$$

$$Q_i = K_Q \Omega_i^2, \quad K_Q = C_Q \rho A R^3, \quad (1.40)$$

where C_T and C_Q are the thrust and torque coefficients, ρ is the air density, A and R are respectively the area of the propeller disk and its radius, and Ω_i is the rotational speed of the i -th propeller.

The overall forces T and the roll L , pitch M and yaw N moments generated by the VTOL propulsion, in body axes, are expressed with the so-called "mixer matrix" χ , which relates the forces and moments generated by the propellers to the square of the angular velocities:

$$\begin{bmatrix} T \\ L \\ M \\ N \end{bmatrix} = \chi \begin{bmatrix} \Omega_{1a}^2 \\ \Omega_{1b}^2 \\ \Omega_{2a}^2 \\ \Omega_{2b}^2 \\ \Omega_{3a}^2 \\ \Omega_{3b}^2 \\ \Omega_{4a}^2 \\ \Omega_{4b}^2 \end{bmatrix}. \quad (1.41)$$

The mixer matrix χ depends on motors coefficients (K_T and K_Q), the distances between the motors and the center of gravity of the aircraft and the direction of rotation of the motors: it will be defined in Chapter 2 following the presentation of the hardware upgrades performed on the VTOL.

In particular, to generate a rolling moment, the rotation is increased on the propellers on one side of the vehicle and decreased on the propellers on the other side. Similarly, for the pitching moment there is a difference between the rotation of forward and rear motors. For the yaw moment, instead, the rotation on diametrically opposite propellers is increased and simultaneously decreased on the remaining propellers. Hence, the total torque provided by the VTOL motors is

not zero anymore, and a resulting moment about the z axis is generated, while the other forces and moments remain the same as during the hover condition.

Being χ rectangular, the required rotor-motor angular speeds, needed for control purposes, are obtained with the pseudo inverse matrix χ^\dagger :

$$\begin{bmatrix} \Omega_{1a}^2 \\ \Omega_{1b}^2 \\ \Omega_{2a}^2 \\ \Omega_{2b}^2 \\ \Omega_{3a}^2 \\ \Omega_{3b}^2 \\ \Omega_{4a}^2 \\ \Omega_{4b}^2 \end{bmatrix} = \chi^\dagger \begin{bmatrix} T \\ L \\ M \\ N \end{bmatrix} = \chi^T (\chi \chi^T)^{-1} \begin{bmatrix} T \\ L \\ M \\ N \end{bmatrix}. \quad (1.42)$$

Forward-flight mode

Aerodynamic forces and moments

Aerodynamic forces and moments, in the wind frame, can be written as follows:

$$\begin{bmatrix} D \\ Q \\ L \end{bmatrix} = \frac{1}{2} \rho V^2 S \begin{bmatrix} C_D \\ C_Q \\ C_L \end{bmatrix}, \quad \begin{bmatrix} L_A \\ M_A \\ N_A \end{bmatrix} = \frac{1}{2} \rho V^2 S \begin{bmatrix} b C_L \\ c C_M \\ b C_N \end{bmatrix}, \quad (1.43)$$

where V is the absolute value of airspeed, S is the wing's reference surface, c is the mean aerodynamic chord, b is the wingspan, D , Q , L are drag, sideforce, lift and L_A , M_A , N_A are pitching, rolling and yawing aerodynamic moments. The coefficients C_D , C_Q , C_L , C_L , C_M , C_N are, in the most general sense, function of the angle of attack α and its derivative $\dot{\alpha}$, angle of sideslip β and its derivative $\dot{\beta}$, body angular rates p , q , r , airspeed V , aileron, elevator and rudder deflections δ_a , δ_e , δ_r . The derivatives of the aerodynamic coefficients are calculated in [2] with the VLM software *OpenVSP*. The forces and moments, calculated in the wind frame, are then expressed in body axes by multiplying them with the transformation matrix from the wind frame to body axes T_W^B :

$$T_W^B = \begin{bmatrix} \cos \alpha \cos \beta & -\cos \alpha \sin \beta & -\sin \alpha \\ \sin \beta & \cos \beta & 0 \\ \sin \alpha \cos \beta & -\sin \alpha \sin \beta & \cos \alpha \end{bmatrix}, \quad (1.44)$$

hence

$$F_{Aero}^B = T_W^B \begin{bmatrix} -D \\ -L \\ -Q \end{bmatrix}, \quad M_{G_{Aero}}^B = T_W^B \begin{bmatrix} L_A \\ M_A \\ N_A \end{bmatrix}, \quad (1.45)$$

where the negative sign in front of the forces comes from the definition of drag, lift and sideforce.

Propulsive forces and moments

The propulsive force of the two horizontal propellers is calculated with equation (1.39) and is aligned with the aircraft x body axis, and hence has always only an x component in the body frame:

$$\mathbf{F}_{Prop}^{\mathcal{B}} = \begin{bmatrix} 2T \\ 0 \\ 0 \end{bmatrix}. \quad (1.46)$$

The moment generated by the forward flight propellers has only a pitch component, since the two motors spin in opposite directions. Hence, by denoting as d_{vert} the vertical (along the body z axis) distance between the motors and the center of gravity, the moment generated by the propulsive units, in body axes, is given by the following expression:

$$\mathbf{M}_{G_{Prop}}^{\mathcal{B}} = \begin{bmatrix} 0 \\ -2d_{vert}T \\ 0 \end{bmatrix}. \quad (1.47)$$

1.4 Multicopter linearized mathematical model

The equations of motion of the multirotor linearized about a reference steady flight condition (hovering condition), derived in [13], are here reported:

$$\begin{aligned} m\Delta\dot{u} &= -mg\Delta\theta + \frac{\partial X_T}{\partial\delta_{lon}}\Delta\delta_{lon} + \frac{\partial X_T}{\partial u}\Delta u + \frac{\partial X_T}{\partial q}\Delta q, \\ m\Delta\dot{v} &= mg\Delta\phi + \frac{\partial Y_T}{\partial\delta_{lat}}\Delta\delta_{lat} + \frac{\partial Y_T}{\partial v}\Delta v + \frac{\partial Y_T}{\partial p}\Delta p, \\ m\Delta\dot{w} &= \frac{\partial Z_T}{\partial\delta_{ver}}\Delta\delta_{ver} + \frac{\partial Z_T}{\partial w}\Delta w, \\ J_{xx}\Delta\dot{p} &= \frac{\partial \mathcal{L}_{\mathcal{T}}}{\partial\delta_{lat}}\Delta\delta_{lat} + \frac{\partial \mathcal{L}_{\mathcal{T}}}{\partial v}\Delta v + \frac{\partial \mathcal{L}_{\mathcal{T}}}{\partial p}\Delta p, \\ J_{yy}\Delta\dot{q} &= \frac{\partial \mathcal{M}_{\mathcal{T}}}{\partial\delta_{lon}}\Delta\delta_{lon} + \frac{\partial \mathcal{M}_{\mathcal{T}}}{\partial u}\Delta u + \frac{\partial \mathcal{M}_{\mathcal{T}}}{\partial q}\Delta q, \\ J_{zz}\Delta\dot{r} &= \frac{\partial \mathcal{N}_{\mathcal{T}}}{\partial\delta_{dir}}\Delta\delta_{dir} + \frac{\partial \mathcal{N}_{\mathcal{T}}}{\partial r}\Delta r. \end{aligned} \quad (1.48)$$

where u, v and w are the components of the velocity of the center of mass with respect to an inertial reference system expressed in the body frame; X_T, Y_T, Z_T and $\mathcal{L}_{\mathcal{T}}, \mathcal{M}_{\mathcal{T}}, \mathcal{N}_{\mathcal{T}}$ are the total external forces and moments in body reference frame;

the δ are dimensionless variables that express the intensity of the maneuvers, in particular: δ_{ver} for collective thrust, δ_{dir} for change in direction, δ_{lat} for rolling and driving lateral movements, δ_{lon} for pitching and driving longitudinal movements.

1.4.1 State equations

The linearized flight dynamics equations (1.48) can be reformulated as a set of first-order differential equations of *state variables* x , that are the minimum set of variables that fully describes the system and its response to any given set of *inputs* u :

$$\dot{x} = A(\vartheta)x + B(\vartheta)u \quad (1.49)$$

where ϑ is the set of time-invariant physical parameters that defines the model structure. In the case of the multicopter the general state model of equation (1.49) can be written as follows:

$$x = [v \ p \ \phi \ u \ q \ \theta \ r \ \Delta\psi \ w]^T, \quad u = [\delta_{lat} \ \delta_{lon} \ \delta_{dir} \ \Delta\delta_{ver}]^T \quad (1.50)$$

$$\begin{aligned} \vartheta &= \{\vartheta_{lat} \ \vartheta_{lon} \ \vartheta_{dir} \ \vartheta_{ver}\}, \\ \vartheta_{lat} &= \left\{ \frac{1}{m} \frac{\partial Y_T}{\partial v} \ \frac{1}{m} \frac{\partial Y_T}{\partial p} \ \frac{1}{J_{xx}} \frac{\partial \mathcal{L}_T}{\partial v} \ \frac{1}{J_{xx}} \frac{\partial \mathcal{L}_T}{\partial p} \ \frac{1}{m} \frac{\partial Y_T}{\partial \delta_{lat}} \ \frac{1}{J_{xx}} \frac{\partial \mathcal{L}_T}{\partial \delta_{lat}} \right\} \\ &= \{Y_v \ Y_p \ L_v \ L_p \ Y_\delta \ L_\delta\}, \\ \vartheta_{lon} &= \left\{ \frac{1}{m} \frac{\partial X_T}{\partial u} \ \frac{1}{m} \frac{\partial X_T}{\partial q} \ \frac{1}{J_{yy}} \frac{\partial \mathcal{M}_T}{\partial u} \ \frac{1}{J_{yy}} \frac{\partial \mathcal{M}_T}{\partial q} \ \frac{1}{m} \frac{\partial X_T}{\partial \delta_{lon}} \ \frac{1}{J_{yy}} \frac{\partial \mathcal{M}_T}{\partial \delta_{lon}} \right\} \\ &= \{X_u \ X_q \ M_u \ M_q \ X_\delta \ M_\delta\}, \\ \vartheta_{dir} &= \left\{ \frac{1}{J_{zz}} \frac{\partial \mathcal{N}_T}{\partial r} \ \frac{1}{J_{zz}} \frac{\partial \mathcal{N}_T}{\partial \delta_{dir}} \right\} = \{N_r \ N_\delta\}, \\ \vartheta_{ver} &= \left\{ \frac{1}{m} \frac{\partial Z_T}{\partial w} \ \frac{1}{m} \frac{\partial Z_T}{\partial \delta_{ver}} \right\} = \{Z_w \ Z_\delta\}, \end{aligned} \quad (1.51)$$

$$A = \begin{bmatrix} Y_v & Y_p & g & 0 & 0 & 0 & 0 & 0 & 0 \\ L_v & L_p & 0 & 0 & 0 & 0 & 0 & 0 & 0 \\ 0 & 1 & 0 & 0 & 0 & 0 & 0 & 0 & 0 \\ 0 & 0 & 0 & X_u & X_q & -g & 0 & 0 & 0 \\ 0 & 0 & 0 & M_u & M_q & 0 & 0 & 0 & 0 \\ 0 & 0 & 0 & 0 & 1 & 0 & 0 & 0 & 0 \\ 0 & 0 & 0 & 0 & 0 & 0 & N_r & 0 & 0 \\ 0 & 0 & 0 & 0 & 0 & 0 & 1 & 0 & 0 \\ 0 & 0 & 0 & 0 & 0 & 0 & 0 & 0 & Z_w \end{bmatrix}, \quad B = \begin{bmatrix} Y_\delta & 0 & 0 & 0 \\ L_\delta & 0 & 0 & 0 \\ 0 & 0 & 0 & 0 \\ 0 & X_\delta & 0 & 0 \\ 0 & M_\delta & 0 & 0 \\ 0 & 0 & 0 & 0 \\ 0 & 0 & N_\delta & 0 \\ 0 & 0 & 0 & 0 \\ 0 & 0 & 0 & Z_\delta \end{bmatrix}. \quad (1.52)$$

The perturbed terms in equation (1.48), indicated with Δ , has been substituted with the actual quantity to avoid a heavy notation, whenever its reference value in hovering condition is zero.

1.4.2 Transfer functions

The structured model, as a function of the physical parameters ϑ , is finally obtained adding to equation (1.49) the output equation

$$y = C(\vartheta)x + D(\vartheta)u \quad (1.53)$$

where $y = [p \ q \ r \ w]^T$ is the output vector and:

$$C = \begin{bmatrix} 0 & 1 & 0 & 0 & 0 & 0 & 0 & 0 & 0 \\ 0 & 0 & 0 & 0 & 1 & 0 & 0 & 0 & 0 \\ 0 & 0 & 0 & 0 & 0 & 0 & 1 & 0 & 0 \\ 0 & 0 & 0 & 0 & 0 & 0 & 0 & 0 & 1 \end{bmatrix}, \quad D = \begin{bmatrix} 0 & 0 & 0 & 0 \\ 0 & 0 & 0 & 0 \\ 0 & 0 & 0 & 0 \\ 0 & 0 & 0 & 0 \end{bmatrix}. \quad (1.54)$$

In the Laplace domain, the Multi-Input Multi-Output (MIMO) transfer function can be formulated starting from the state space system made up of equations (1.52) and (1.54) as

$$G(s) = C(sI - A)^{-1}B + D = \begin{bmatrix} G_p(s) & 0 & 0 & 0 \\ 0 & G_q(s) & 0 & 0 \\ 0 & 0 & G_r(s) & 0 \\ 0 & 0 & 0 & G_w(s) \end{bmatrix}, \quad (1.55)$$

where the Single-Input Multi-Output (SISO) models are:

$$G_p(s) = \frac{s(L_\delta s - L_\delta Y_v + L_v Y_\delta)}{s^3 - (L_p + Y_v)s^2 + (L_p Y_v - L_v Y_p)s - g L_v}, \quad (1.56)$$

$$G_q(s) = \frac{s(M_\delta s + M_u X_\delta - M_\delta X_u)}{s^3 - (M_q + X_u)s^2 + (M_q X_u - M_u X_q)s + g M_u}, \quad (1.57)$$

$$G_r(s) = \frac{N_\delta}{s - N_r}, \quad (1.58)$$

$$G_w(s) = \frac{Z_\delta}{s - Z_w}. \quad (1.59)$$

The transfer functions just formulated provide an insight of the estimation problem of the physical parameters of an under-actuated multirotor UAV. The overall UAV dynamics has been decoupled into SISO structured models describing its dynamics around each body axis. In particular, the lateral and longitudinal transfer functions are not of the zero type but present a zero in the origin (*i.e.*, for $s = 0$).

Chapter 2

Hardware upgrades

This chapter presents the hardware modifications implemented on the VTOL due to the problems encountered in the first flight tests. In fact, during the first flight the vehicle does not take off: the thrust generated by the motors, even at full throttle, is not enough to lift completely the VTOL, only minor bumps on the ground have been achieved. Moreover, a strong weight imbalance has been noticed mainly due to the tail since it remains always on the ground. Rotations of the front motor booms within their fuselage supports have been seen. Solved this complications, the vehicle is able to get off the ground but other problems related to battery and power distribution are faced. Additionally, large torsional and bending movements of the fuselage and wings are present, affecting the controllability and stability of the VTOL during the flight.

The chapter is organized as follow: the first section presents the infrastructure used in the experimental activities, the second one the problems related to weight and balance, the third one those related to the propulsive system while the fourth is related to structural problems. The last section summarizes the UAV specifications after the hardware upgrades presented in the chapter.

2.1 Aerospace Systems and Control Laboratory

The experiments are carried out in the Flying Arena for Rotorcraft Technologies (Fly-ART) of Politecnico di Milano (Figure 2.1) which is an indoor facility with a flight volume of 12m x 6m x 4m, equipped with a *Motion Capture system* (Mo-Cap) connected to a *Ground Control System* (GCS).

Motion Capture System

The Mo-Cap is composed by 12 Infra-Red (IR) sensitive Optitrack cameras which incorporate IR flood lights (Figure 2.2a). The cameras, mounted on the FlyART structure, are fixed at calibrated positions and orientation so that the measurement object is into the field of view of multiple cameras. Through markers sensi-



Figure 2.1: Flying Arena for Rotorcraft Technologies (Fly-ART).

tive to infrared light (Figure 2.2b) mounted on top of the drones, it is possible to track and define their positions into space: this information is processed by Motive, which is the Optitrack software platform, that tracks the rigid-body motion of the UAV and estimates the attitude and the position inside the flight volume ([14], [15]).

For this reason, the wings of the VTOL, originally composed by a reflecting surface (Mylar cladding), have been painted with a matt white coating, avoiding undesirable reflection of the Optitrack infrared light that may corrupt the measurements.

Ground Control System

The GCS is dedicated to send and retrieve information from the multicopter during the flight session. The communication with the drone is based on the Robot Operating System (ROS): it is a communication interface that enables different parts of a robot system, including UAVs, to discover each other, and send and receive data between them; indeed, ROS provides libraries, tools, hardware abstractions, device drivers, visualizers, messagepassing, package management, and more ([17]).

2.2 Weight and balance

The design weight W_{TO} and the estimated position of center of gravity x_{CG} and neutral point x_N (measured from the leading edge of the wing), calculated in [1], are reported in Table 2.1. In particular the aircraft is designed to be longitudinally statically stable: the center of gravity is in front of the neutral point, with a static



Figure 2.2: Motion Capture System.

Parameter	Value
W_{TO}	4.8 kg
x_{CG}	-10 cm
x_N	-13 cm

Table 2.1: Aircraft mass, position of center of gravity and neutral point calculated in design phase ([1]). Being the axis from the tail to the nose, a negative x value means that the point is behind the wing leading edge.

margin e , defined as

$$e = \frac{x_{CG} - x_N}{MAC}, \quad (2.1)$$

equals to 13%, where MAC is the mean aerodynamic chord ($MAC = 23$ cm, from [1]). The neutral point position has been initially estimated using *XFLR5* in [1], and then validated with *OpenVSP* in [2].

The real aircraft is now weighted: the actual weight W_{TO} is 5.7 kg, 18.75% more of the design value. This is caused by uncertainties of the CAD model and by the modifications occurred during the production and integration of the components (see [2]).

The weight of the 3D printed tail ($W_{Tail} = 506$ g) causes an imbalance towards the rear part of the vehicle: the resultant CG position ($x_{CG} = -17.8$ cm) is well behind the neutral point ($x_N = -13.0$ cm), so the VTOL is statically unstable. It has been decided to change the material of the tail surfaces: the aerodynamic loads acting on these are limited, so it has been chosen the balsa wood which is much

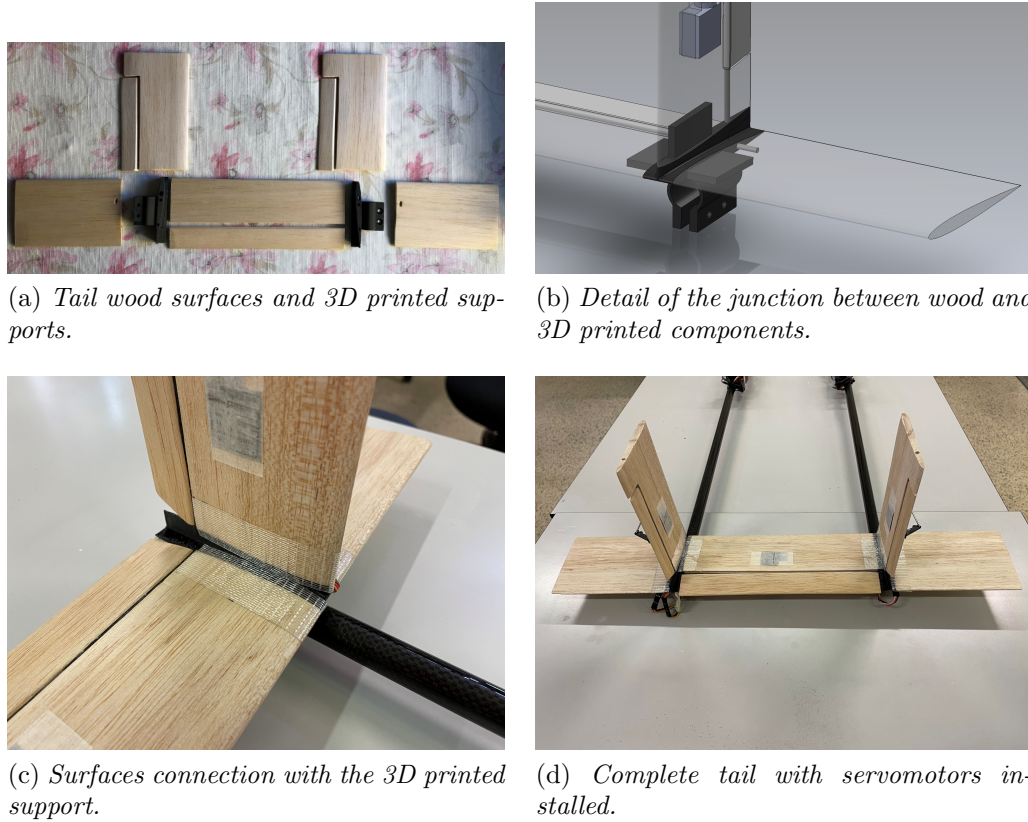


Figure 2.3: New balsa wood tail.

more lighter. The surfaces are then produced with the same external geometry (Figure 2.3a) but with some modification in the inner structure to allows a better connection with the 3D printed support, accounting with the structural limits of the material and of the manufacturing process. The surfaces are connected to the support through a joint (Figure 2.3b), glued and reinforced with duct tape (Figure 2.3c). The result is a tail with the same shape of the old one (Figure 2.3d) but that is much more lighter. The comparison between the tails is reported in Table 2.2: the new tail is 65% lighter with respect to the old one and the position of the center of mass x_{CG} is still behind the neutral point but very nearly.

The final weight and the position of center of mass are reported in Section 2.5, calculated after all the implemented modifications.

	Tail mass [g]	Center of mass position x_{CG} [cm]
3D printed tail	506	-17.8
Wood tail	175	-13.6

Table 2.2: Comparison between the old (3D printed) and the new (wood) tails.

	Experimental result	Manufacturer data
Thrust coefficient C_T	0.0168	0.0219
Torque coefficient C_Q	0.00168	0.00229
Power coefficient C_P	0.00168	0.00229

Table 2.3: Motor static coefficients comparison, motor for vertical flight *KDE 2315 XF – 2050*, 5x4.5 inch, 2 blades bullnose propeller, from [2].

2.3 Propulsive system problems

2.3.1 Motors

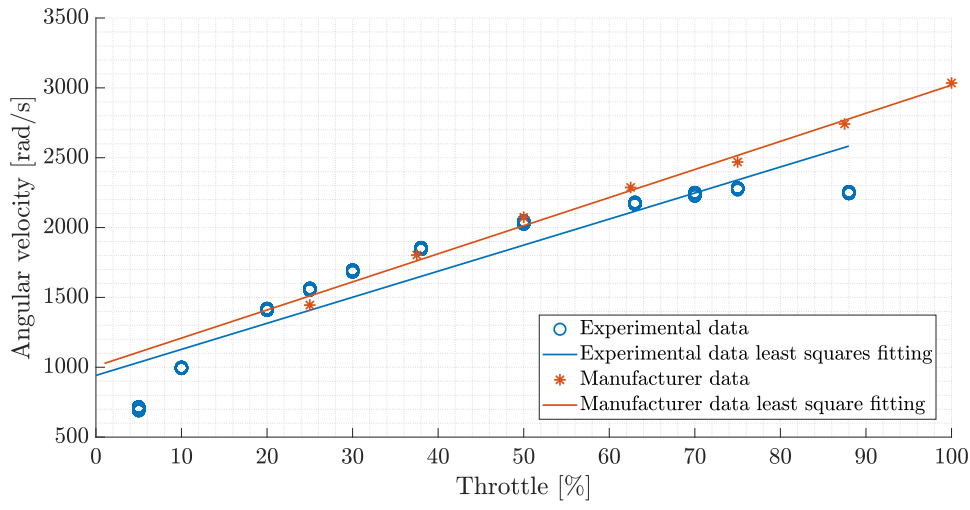
During the motors tests performed in [2] it emerged that the maximum thrust that can be produced by the vertical motors (*KDE 2315 XF – 2050* with 5x4.5 BN propeller and 4S battery) is lower compared to the declared data by the manufacturer ([18]). These results are depicted in Figure 2.4: Figure 2.4a shows the angular velocity against throttle curve: for throttle values greater than 65%, the angular velocity sets to a constant value, less than that indicated by the manufacturer. Figure 2.4b shows the thrust against angular velocity curve, that is always below the data declared by the manufacturer and in particular, due to the limited angular velocity, the maximum thrust obtained (for throttle equal to 90%, limited for excessive vibrations of the test bench structure) is less than half the expected value. The resultant static coefficients are reported in Table 2.3 and confirm the low performance shown in Figure 2.4.

The possible cause of this mismatch, indicated in [2], might be the differences between the propellers used in the test: even though the tested propeller and the one used by the manufacturer have the same macroscopic characteristics (number of blades, diameter and nominal pitch), the actual realisation and manufacturing might be slightly different, hence explaining the mismatch.

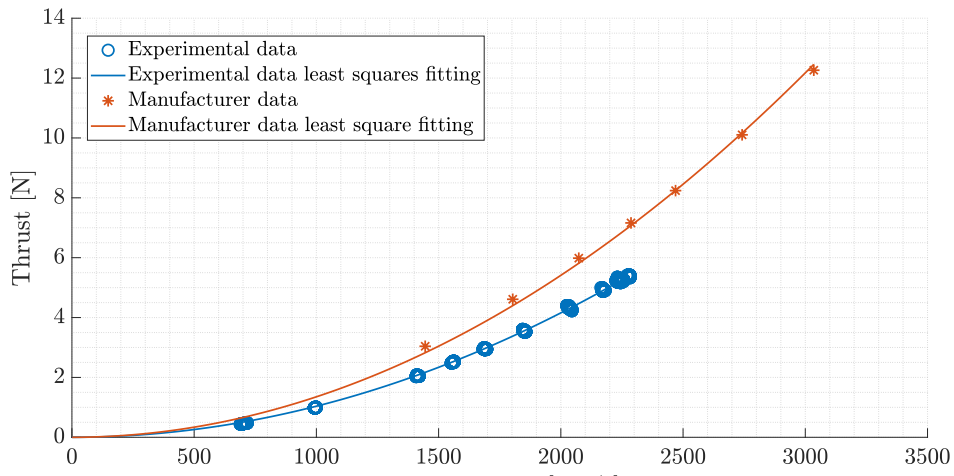
This lower performance, together with the increased weight of the VTOL, does not allow the vehicle to fly.

The possible solutions investigated are:

- power the actual motors with a higher voltage battery;
- change the propellers with different ones more performing;



(a) Angular velocity against throttle.



(b) Thrust against angular velocity.

Figure 2.4: Test at motor test bench of the motor for vertical flight *KDE 2315 XF – 2050*, 5x4.5 inch, 2 blades bullnose propeller, DC power supply, from [2].

- replace the complete propulsion system: motors, propellers, ESC and battery.

Higher voltage battery

The possible choices are limited: the forward motors are limited to work with batteries up to 4 cells (4S) while for the vertical motors the limit is 6S: having a single battery for both the forward and vertical motors, this limitation can not be overtaken. The 6S batteries, already successfully used in the laboratory with other drones, can not be used.

A possible solution is to use a high voltage LiPo battery (LiPo HV) 4S, which has a standard voltage of 15,2 V and a maximum voltage of 17,4 V while at 100% state of charge (SoC), against the 14,8 V in standard condition and 16,8 V at 100% SoC of the standard LiPo batteries. The result of the test at the bench is shown in Figure 2.5, where are depicted the thrust against throttle curve and current against throttle curve. The thrust obtained is similar to the case with the standard battery; always abundantly below the declared value, with a maximum value around the 5.5 N (against the 12.5 N expected). In addition, above 75% of throttle the current absorbed by the motor rises quickly while the thrust settles to a constant value: this condition ended up with the burned engine. Then, this option is discarded.

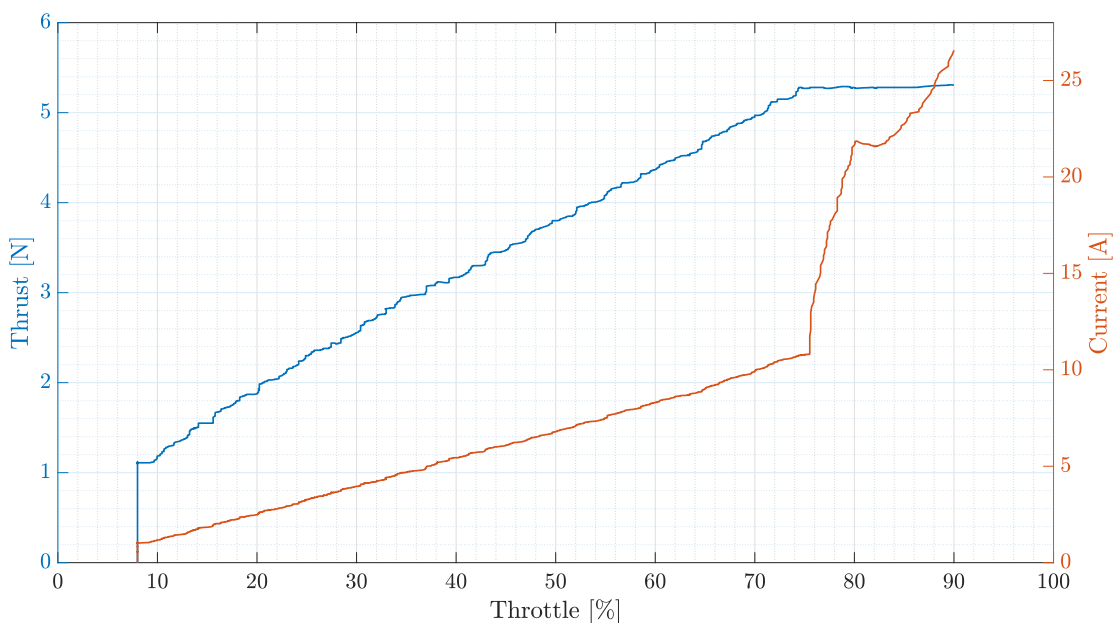


Figure 2.5: Thrust against throttle and current against throttle, motor for vertical flight *KDE 2315 XF – 2050, 5x4.5 inch, 2 blades bullnose propeller, powered with 16,8 V battery.*

New propellers

Different types of propellers are tested, respecting the dimension limit suggested by the motors' manufacturer (diameter limited to 7 inch). The tests are performed with *KDE 2315 XF – 2050* motor powered with the standard LiPo battery (4S, 8500 mAh). The comparison between the thrust against throttle curve for the propellers tested is depicted in Figure 2.6 while in Table 2.4 are described all the different propellers tested and the results obtained. The 7x4.2 propeller model has the best performance, with maximum thrust of 14.89 N; the eight motors can easily support the weight of the vehicle with an hovering throttle equal to 43% and a total current demand of 84 A (Figure 2.7), meetings the propulsion requirements. This solution guarantees excellent performance with a limited economic cost so the propeller 7x4.2 is selected and mounted on the eight vertical motors of the VTOL. Then, the last solution identified has not been studied in detail; moreover, the complete change of the propulsion system would be clearly more expensive with respect to the change of the propellers only. The motors supports have to be moved along the motor booms, increasing their distance in order to have the space necessary for the new propellers with larger diameter (7 inches against 5 inches). This modification has negligible effect on the position of the center of gravity since the change is more or less symmetric with respect to that point.

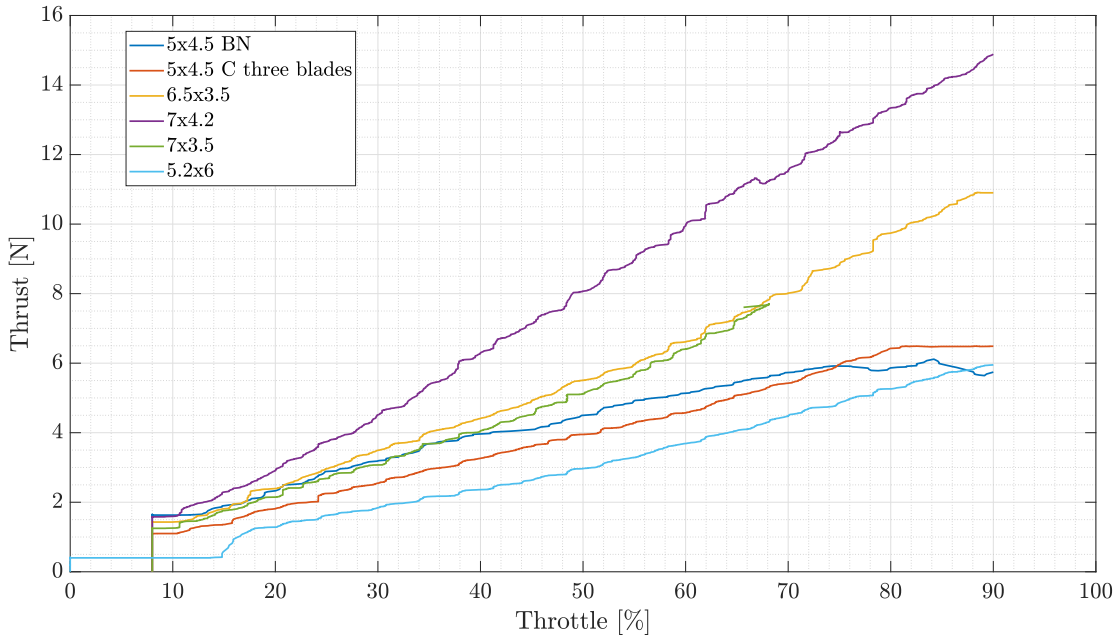
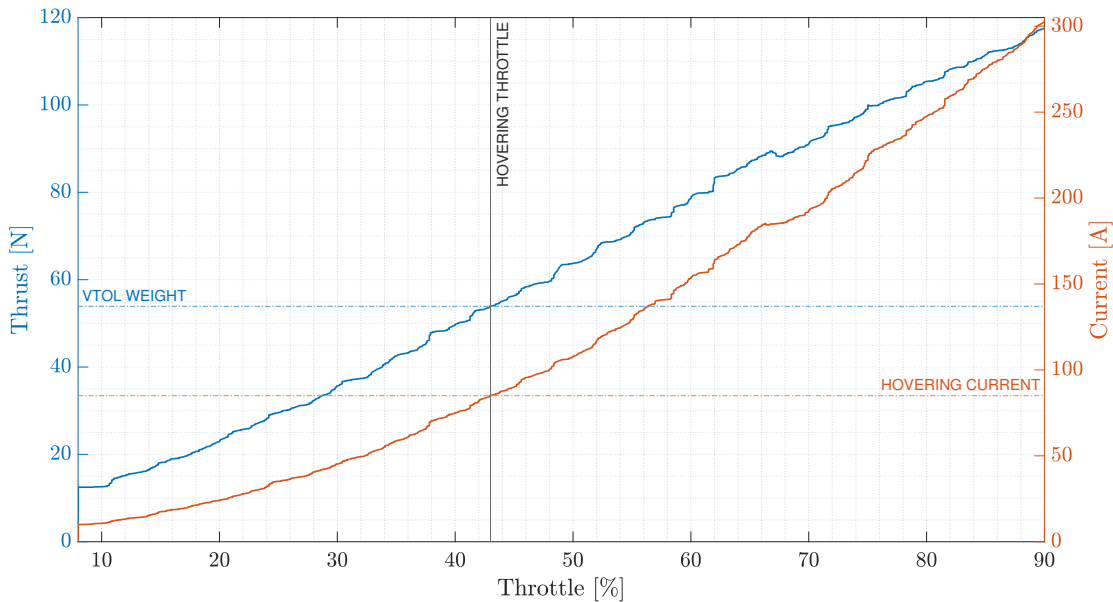


Figure 2.6: Thrust against throttle: comparison between different propellers, vertical flight motor *KDE 2315 XF – 2050*, powered with standard battery.

The new motor static coefficients (thrust, torque and power) and the motor time constant τ are summarized in Table 2.5. The relationship between throttle th and angular velocity Ω , needed for control purposes, is shown in Figure 2.8. The

Propeller	Blades no.	Max thrust [N]	Hovering th [%]	Notes
5x4.5 BN	2	6.12	-	High current absorbed with throttle > 75%
5x4.5 C	3	6.49	-	-
6.5x3.5	2	10.91	62	-
7x4.2	2	14.89	45	-
7x3.5	3	7.68	66	High vibrations (flutter) at 70% throttle
5.2x6	2	5.96	-	-

Table 2.4: Test result for different propellers with vertical propulsion system.

Figure 2.7: Thrust against throttle and current against throttle (for the entire propulsive system): motor for vertical flight *KDE 2315 XF – 2050*, 7x4.2 propeller, powered with standard battery.

C_T [-]	C_Q [-]	C_P [-]	τ [1/s]
0.0186	0.00241	0.00241	0.015

Table 2.5: Motor static coefficients and time constant; motor for vertical flight *KDE 2315 XF – 2050*, 7x4.2 propeller.

Coefficients	Value
a	$2.71 \cdot 10^{-5}$
b	$1.73 \cdot 10^{-4}$

Table 2.6: Angular velocity against throttle quadratic model's coefficients.

linear model used in [2],

$$\Omega = m \cdot th + q, \quad (2.2)$$

shows poor fitting result, especially at low throttle values, calculating a non zero angular velocity with zero throttle command. For this reason, in the present work the following quadratic model is used

$$th = a \cdot \Omega^2 + b \cdot \Omega. \quad (2.3)$$

The relationship between angular velocity Ω and throttle command th is

$$\Omega = \frac{-b + \sqrt{b^2 + 4 \cdot a \cdot th}}{2 \cdot a}. \quad (2.4)$$

The coefficients a and b , obtained with a least square fitting, are summarized in Table 2.6. The comparison between the two models is depicted in Figure 2.8: the quadratic model has better result in all the throttle range.

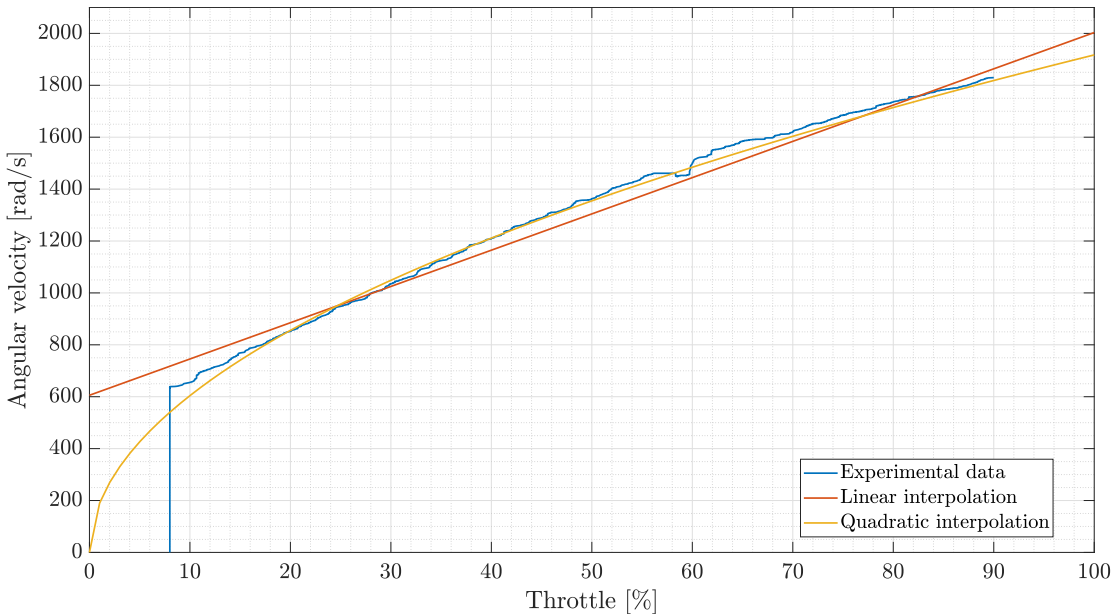


Figure 2.8: Angular velocity against throttle: motor for vertical flight KDE 2315 XF – 2050, 7x4.2 propeller, powered with standard battery.

2.3.2 Power distribution

The new propellers allows the drone to take off, but during the second flight test other problems related to the propulsive system are identified:

- the current reaches the saturation limit of the Power Distribution Board (PDB) (Figure 2.9), that is 120 A ([19]);
- there is a huge voltage drop; after 30 seconds of flight the voltage goes below the minimum allowable value (13 V for a 4S battery) (Figure 2.9).

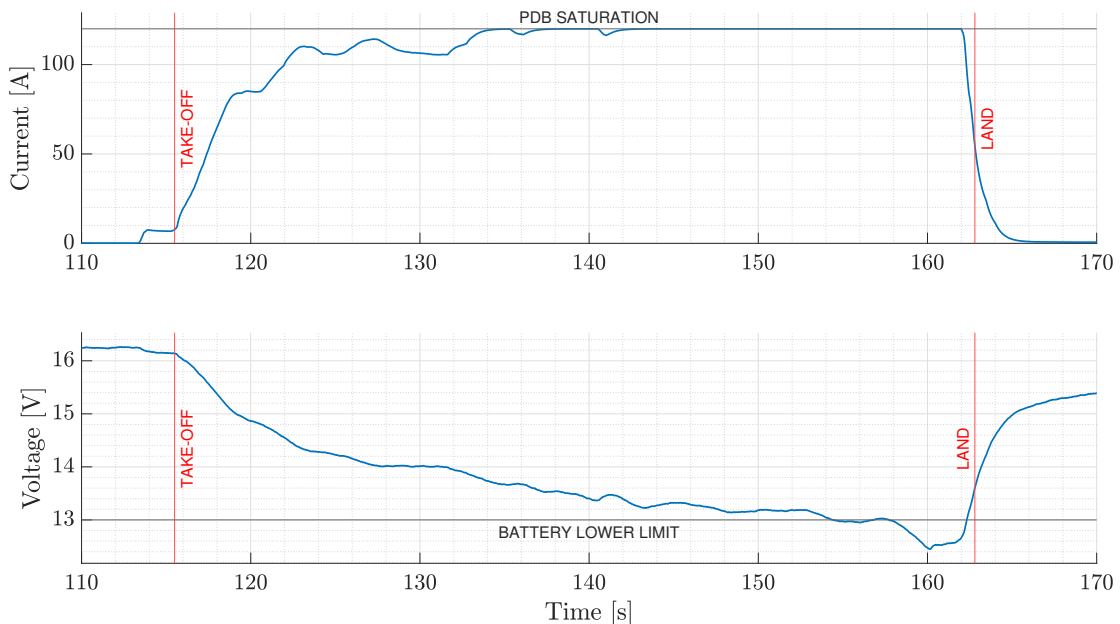


Figure 2.9: Battery data time history during second test flight: motor *KDE 2315 XF – 2050*, 7x4.2 propeller, powered with 4S battery, 100% SoC at the start of the test.

Maximum supplied current problem

The hovering current demand identified during the motors test (Figure 2.7) is equal to 84 A: with this value, there are still 36 A of margin, enough to perform maneuvers, before reaching the saturation limit of the PDB. However, during the flight test, after an initial moment at this value (more or less 120 s), the current continues to increase, reaching the PDB limit (120 A). This is caused by the voltage drop: in order to maintain the same electrical power needed by the motors the current increases. Additionally, Figure 2.7 also shows that for throttle values greater than 70% the current reaches very high values, greater than 200 A, with a maximum of 290 A. It is worth mentioning that usually these throttle values are

Manufacturer	Motor mass [g]	ESC mass [g]
KDE	73.0	64.0
T-MOTOR	36.6	10.0

Table 2.7: Mass of considered motors and ESC.

not maintained for long times in the normal operating life of a UAV.

A second PDB has been mounted on the VTOL to solve the problem and it has been positioned in the front part of the fuselage (Figure 2.11). The ten motors are divided between the two PDBs; thus, the maximum current that can be supplied is 240 A, 120 A for each group made up of 4 vertical motors and one horizontal motor. The 4S - 8500 mAh battery can support this kind of load: it has a standard C-rate¹ of 50C and maximum of 100C, hence it can provide 425 A in standard conditions with a peak of 850 A.

Voltage drop problem

The voltage drop is caused by the internal resistance of the battery and by the high current required by the motors: a battery is not an ideal generator but has an internal resistance, then the larger is the current drawn, the larger is the battery voltage drop. The internal resistance value R_i is calculated experimentally with the procedure described in [20] since it is not provided by the manufacturer ([21]); the internal resistance is equal to 0.034Ω . Hence, for a hovering current demand of 84 A, a voltage drop of 2.85 V occurs, in accordance with the result presented in Figure 2.9.

One way to mitigate the high voltage drop problem is to adopt different components that require a reduced current: *F90 – kv1300* motor together with F45 ESC (manufactured by T-MOTOR [22]), already available in the laboratory, are tested. The weight of the different components of the propulsion system considered (KDE and T-MOTOR) are presented in Table 2.7 and in Table 2.8 there are the final weight of the VTOL for the different propulsive system together with the variation of the position of the center of gravity: the T-MOTOR's configuration is 11.5% lighter, so the thrust required to fly is smaller. The comparison between the thrust curves of the two solutions is shown in Figure 2.10a: even if the aircraft is lighter with the T-MOTOR's components, the hovering throttle is greater because the thrust produced is lower than KDE's motors. Despite this, the current demand in hovering condition is smaller, as shown in Figure 2.10b. The

¹The C-rate is a measure of the rate at which a battery is being charged or discharged. It is defined as the current through the battery divided by the theoretical current draw under which the battery would deliver its nominal rated capacity in one hour. Hence, for example, for a battery rated at 8500 mAh, a 1C discharge delivers 8.5 A of current, a 10C discharge delivers 85 A of current, and a 20C discharge delivers 170 A of current.

Motor	ESC	Total mass [kg]	x_{CG} variation [mm]
KDE	ESC	5.56	-
T-MOTOR	T-MOTOR	4.92	-4.6

Table 2.8: Total mass of the drone and variation of x_{CG} for different propulsive system.

	KDE	T-MOTOR
Hovering current [A]	84	70
Maximum current [A]	289	154
Hovering throttle [%]	43	66

Table 2.9: Current and throttle comparison between KDE and T-MOTOR propulsion systems.

resulting throttles and currents are reported in Table 2.9: the current demand in hovering condition is 70 A; considering the battery internal resistance (0.033 Ω), it would cause a voltage drop of 2.38 V, similar to the previous case. Since this option does not work, it is necessary to split the power system: by using two batteries, selected with the same voltage but half the capacity with respect to the original one, the request of current and the consequent voltage drop are divided between the two. This choice is also facilitated by the presence of the two PDBs: each battery is connected to a single PDB that powers four vertical motors and one horizontal motor.

Considering the results shown in this section, it has been decided to maintain the original motors and ESCs: in fact the T-MOTOR's option has a slightly lower current demand but with lower maximum thrust and higher throttle value to perform hovering; that translates into a reduced thrust margin for maneuvers. The high economic cost to replace all the motors and ESCs is therefore not justified. The selected batteries (produced by [21]) specifications are presented in Table 2.10: they have the same voltage (14.8 V) and half the capacity (4000 mAh) but weigh 480 g, hence there is an increase of mass of 290 g with respect to the single battery case.

Summarizing, the solution implemented is made up of two parts: a second PDB and a dual battery with reduced capacity. This option proves to be much cheaper than replacing the complete propulsive system. In Figure 2.11 is shown the front of the fuselage with the new components: there are the two batteries, that fits perfectly in the original volume, and the additional PDB, that uses the space originally designed for the payload.

The modifications have been successfully tested: in Figure 2.12 are depicted cur-

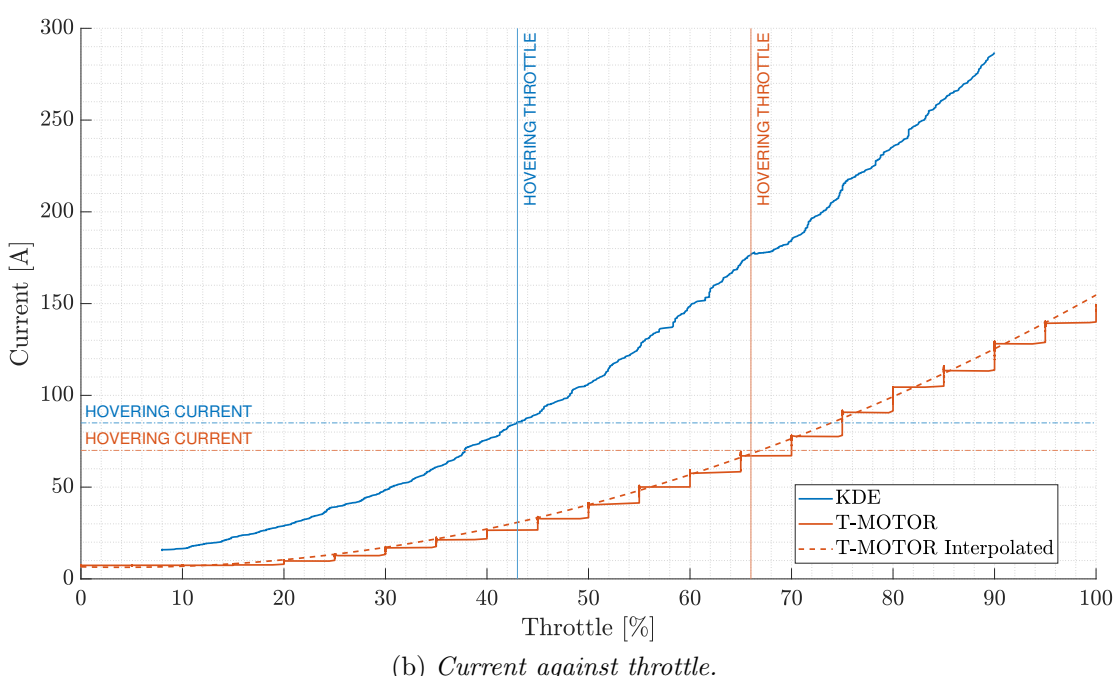
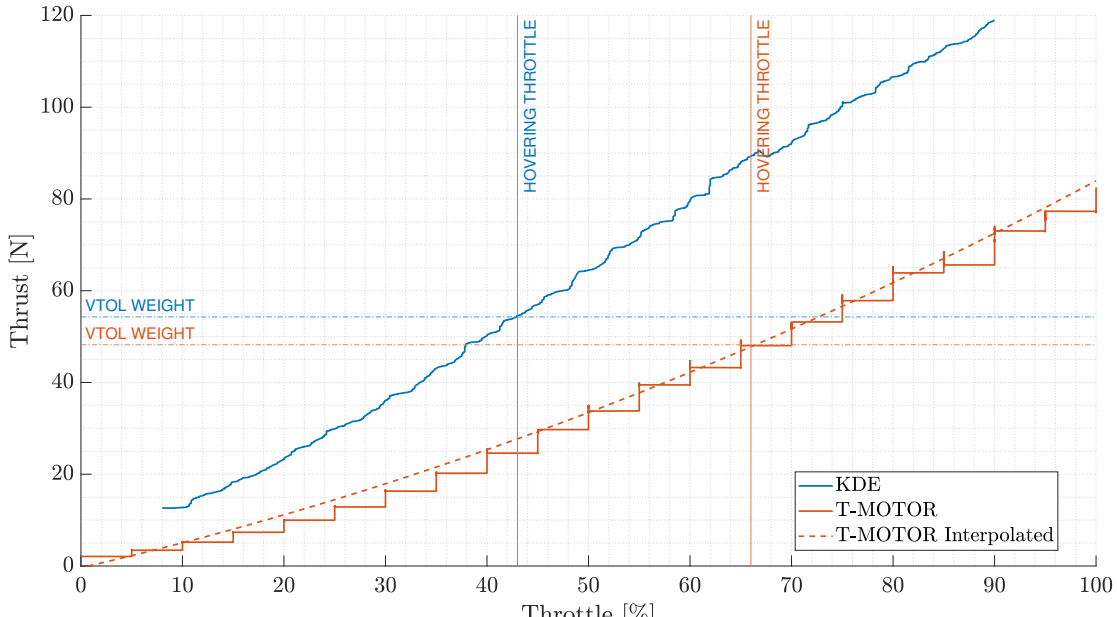


Figure 2.10: Thrust and current comparison between KDE and T-MOTOR propulsion systems, 7x4.2 propeller, powered with 4S battery.

Parameter	Value
Type	LiPo
Cells	4
Voltage	14.8 V
Capacity	4000 mAh
C rate	60-120
Mass	480 g

Table 2.10: Final batteries characteristics (specifications of single battery shown).

rent and voltage of the two batteries during an endurance test (the small differences between the batteries are caused by the fact that only one battery powers all the electronics). In a two minutes flight the current never reaches the saturation limit and it has a mean value around 80 A. The minimum voltage is 14 V, greater than the recommended lower limit. The voltage drop still has important effects on the flight duration: the drone landed with 25% battery SoC but, after some seconds with the motors in idle, the measured battery SoC was 50%, allowing another short flight. This consideration is important considering the nature of this VTOL aircraft: after a high current demanding vertical flight phase, the battery would recover during transition and in forward flight since the current demand is heavily reduced.

The final weight and the position of center of mass are reported in Section 2.5, calculated after all the implemented modifications.

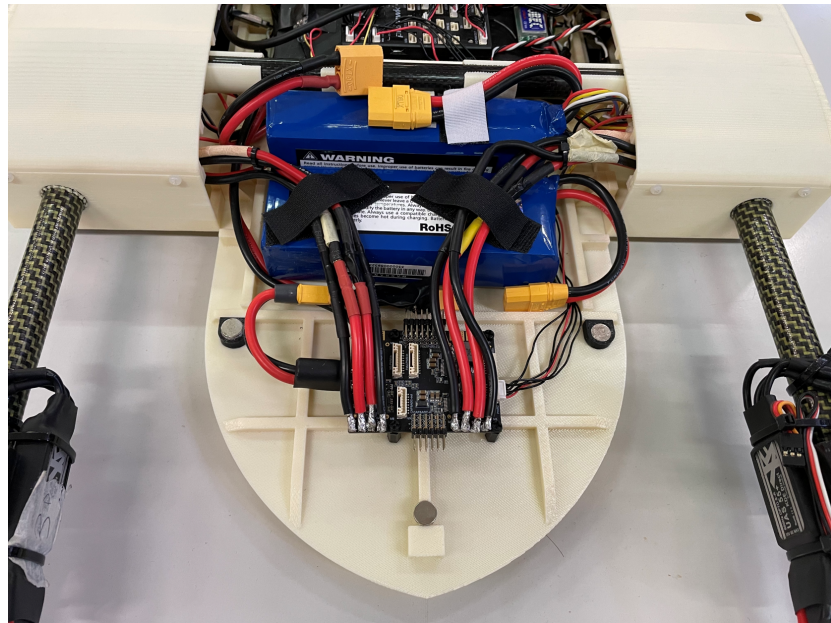


Figure 2.11: Front fuselage part with double battery and second PDB installed.

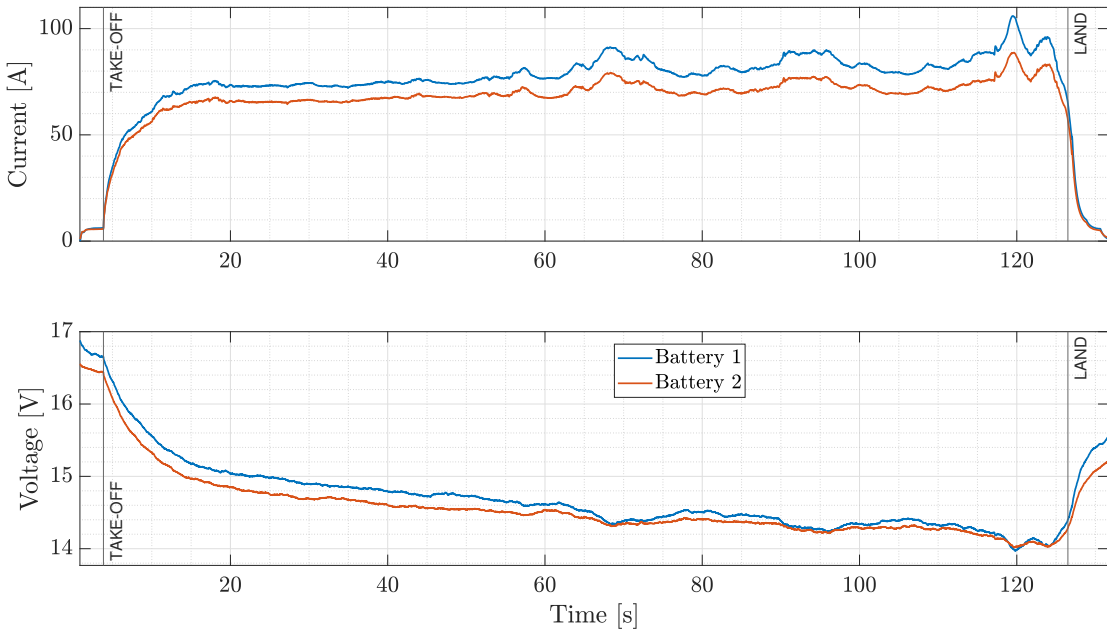


Figure 2.12: Current and voltage time histories during an endurance test with double PDB and battery.

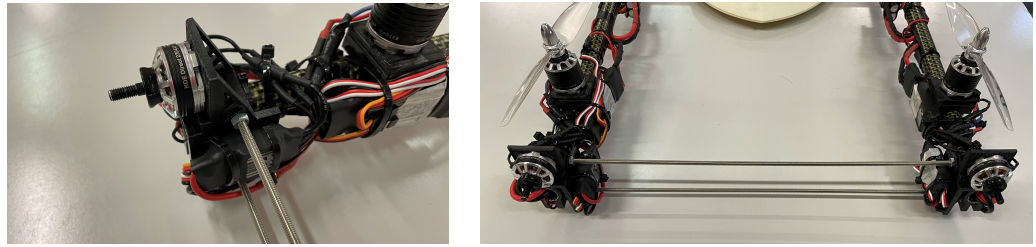
2.4 Structural problems

During the first flight the front motor booms rotate within their fuselage supports, with the consequent change of motors thrust direction; this is caused by the locking mechanism that allows some minor movements. The problem is solved by connecting the two booms with two metal rods, using the support of the horizontal motor, as shown in Figure 2.13. This modification, in addition to increase the overall stiffness, has the benefit to add weight in the front of the vehicle, moving the center of gravity to a more advanced position.

In the second test flight, the following problems arise:

- strong torsion of the fuselage: right and left booms rotate around the \mathbf{b}_2 axis in opposite directions while performing yaw maneuvers;
- vibrations of the wings.

These structural problems deeply affect the dynamics of the vehicle. In particular, the torsion of the fuselage structure causes an uncontrolled drift of the yaw angle: the rotations of the booms changes the direction of the forces of the motors mounted on them, generating two opposite components of force in the horizontal plane (the plane defined by the vectors \mathbf{b}_1 and \mathbf{b}_2). These causes a yaw moment, which is greater than the control one (that is generated by the different angular velocities between clockwise and counterclockwise motors) and hence a rotation



(a) *Detail of the connection of the rods to the motor support.*
(b) *Front motor supports connected with the rods.*

Figure 2.13: Front motor booms modification.

along the yaw axis. This situation is depicted in Figure 2.14: even if the yaw control moment tries to counter the rotation, reaching the saturation, the vehicle continues drifting.

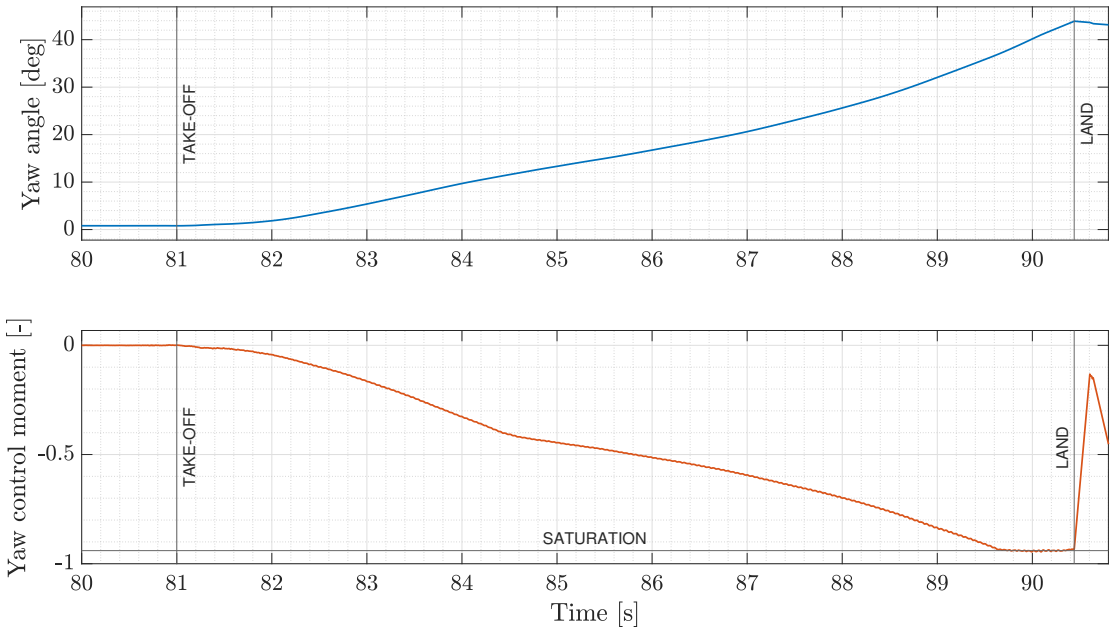


Figure 2.14: Time history of yaw angle and normalized yaw control moment.

The first modification implemented is the change of the direction of the rotations of some motors. It has been chosen in ([2]) to install, on each boom, motors spinning in the same direction.

As already mentioned, this presents a problem during yaw maneuvers causing torsion of the fuselage: as shown in Figure 2.15, the thrust of propellers on opposite booms is changed differentially; this produces a torsion of the fuselage around the b_2 axis and hence the differential rotation of the booms. When the controller increases the yaw control action, it increases the torsional effect, thus increasing

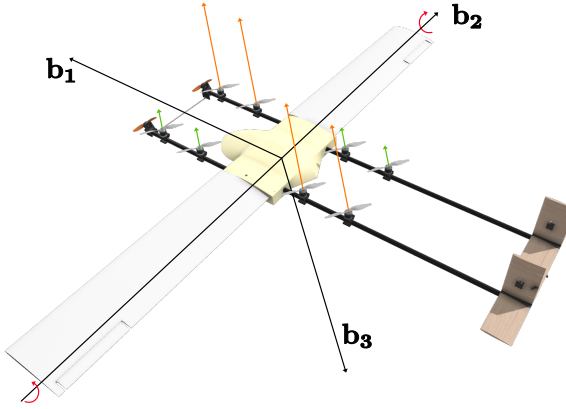


Figure 2.15: Motors forces during a yaw maneuver with original configuration of propellers.

the problem.

Hence, the propeller spin directions are changed in order to have on each boom two motors that rotate in opposite directions, as shown in Figure 2.16. With this configuration, during a yaw maneuver, the total force on each boom is equal and hence no moment along the \mathbf{b}_2 axis is produced.

Once the propeller rotations are defined, it is necessary to update the mixer matrix introduced in Chapter 1 with respect to the one developed in [2]:

$$\begin{bmatrix} T \\ L \\ M \\ N \end{bmatrix} = \begin{bmatrix} K_T & K_T \\ K_T l_f & K_T l_f & -K_T l_f & -K_T l_f & -K_T l_r & -K_T l_r & K_T l_r & K_T l_r \\ K_T l_1 & K_T l_2 & K_T l_1 & K_T l_2 & -K_T l_3 & -K_T l_4 & -K_T l_3 & -K_T l_4 \\ -K_Q & K_Q & K_Q & -K_Q & K_Q & -K_Q & -K_Q & K_Q \end{bmatrix} \begin{bmatrix} \Omega_{1a}^2 \\ \Omega_{1b}^2 \\ \Omega_{2a}^2 \\ \Omega_{2b}^2 \\ \Omega_{3a}^2 \\ \Omega_{3b}^2 \\ \Omega_{4a}^2 \\ \Omega_{4b}^2 \end{bmatrix}, \quad (2.5)$$

where the distances l_f , l_r , l_1 , l_2 , l_3 , l_4 are shown in Figure 2.16. The resultant mixer matrix χ is therefore defined as

$$\chi = \begin{bmatrix} K_T & K_T \\ K_T l_f & K_T l_f & -K_T l_f & -K_T l_f & -K_T l_r & -K_T l_r & K_T l_r & K_T l_r \\ K_T l_1 & K_T l_2 & K_T l_1 & K_T l_2 & -K_T l_3 & -K_T l_4 & -K_T l_3 & -K_T l_4 \\ -K_Q & K_Q & K_Q & -K_Q & K_Q & -K_Q & -K_Q & K_Q \end{bmatrix}. \quad (2.6)$$

As seen during the first flight tests, the fuselage has shown to be a very flexible structure.

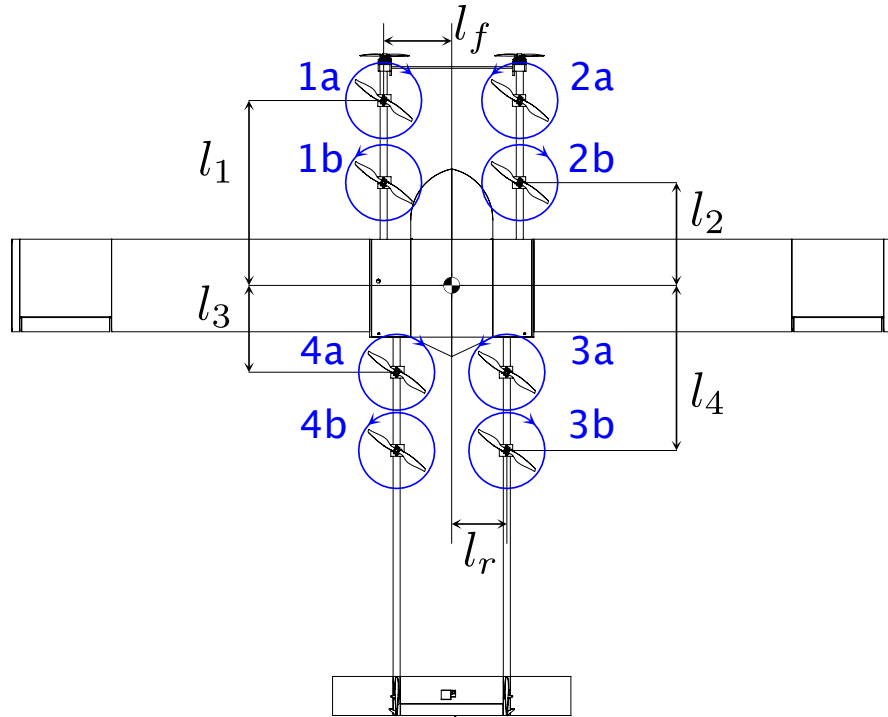


Figure 2.16: Aircraft top view, with relevant dimensions named, propellers numbering and propellers spinning directions.

It has been designed as a single piece in [1] but, due to limitations of the manufacturing process, it has been 3D printed into three separate pieces then put together with glue and screws ([2]). This has reduced the structural stiffness of the fuselage base.

Beside the modifications to the propeller spinning directions presented in Figure 2.16, a carbon plate has been added in the back of the fuselage (Figure 2.17), oriented vertically in order to maximise the inertia moment and the resultant bending stiffness respect to the \mathbf{b}_1 axis.

Last but not least, the wings present vibrations during the flights. This problem is enhanced by the fact that they are made up of two separate pieces not connected together. Then, the wings have been connected together through the spars with a simple joint blocked with a screw (Figure 2.18): with a single spar structure, the bending and torsional stiffness are greatly improved. In addition, with this modification the locking mechanisms used to connect the wings to the fuselage ([1], [2]) are no longer necessary and hence removed, saving weight.

2.5 Final configuration

To summarize, the following hardware modifications have been implemented:

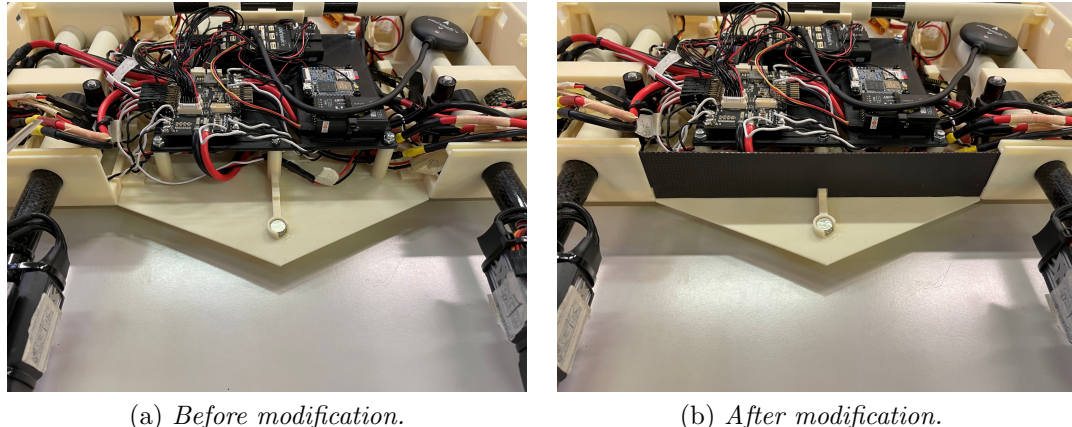
(a) *Before modification.*(b) *After modification.*

Figure 2.17: Fuselage reinforcement with a carbon fiber plate.

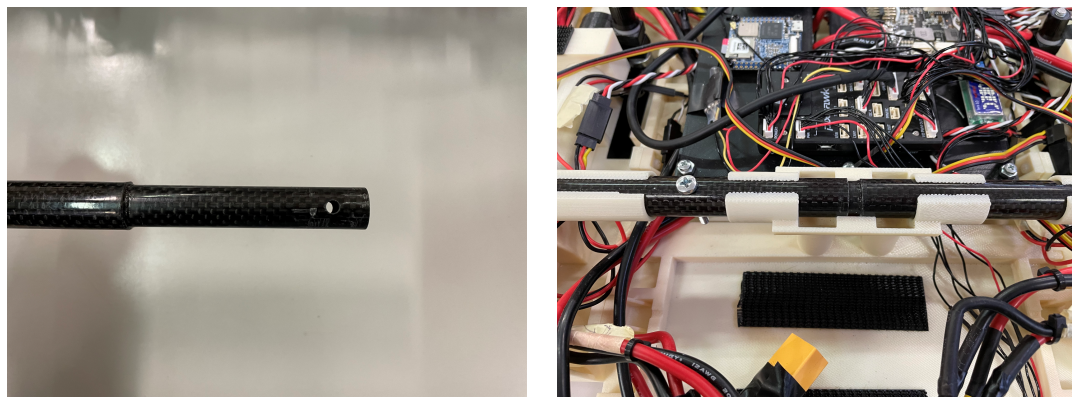
(a) *Spar joint.*(b) *Spars connection.*

Figure 2.18: Modification of the wing locking mechanism.

Parameter	Value
W_{TO}	6.4 kg
x_{CG}	-12.9 cm
x_N	-13.0 cm

Table 2.11: Aircraft mass, position of center of gravity and neutral point of the final configuration of the VTOL. Position measured from the wing leading edge along the b1 body axis.

- painted wings;
- balsa wood tail;
- new propellers for vertical motors;
- additional PDB;
- double battery;
- changed direction of rotations of the propeller;
- structural reinforcements between the forward motor support;
- connection between the wings;
- reinforcement of the fuselage with a carbon fiber plate.

With these minor modifications, the main hardware problems have been solved, allowing the vehicle to fly.

The final mass of the VTOL and the position of the center of gravity after all the modifications are summarized in Table 2.11: the final mass is 33% greater than the design value, the position of the center of gravity is almost coincident with the neutral point, hence the aircraft could be considered statically neutral. The VTOL after the hardware modifications is shown in Figure 2.19.

The CAD model and the *Simulink* model (implemented in [1] and [2]) are then updated following the modification implemented on the real aircraft.

The parameters of the dynamic modes (eigenvalues, damping and frequency) of the updated vehicle are calculated using the usual procedure ([2]) and compared with those of the old version in Table 2.12 and Table 2.13. The results from the new model are similar to the previous results: the short period, dutch roll and roll modes are all stable. The spiral mode remains unstable together with the phugoid mode.



Figure 2.19: Final configuration of the VTOL.

Mode	Previous model of [2]		Improved model	
	Real part	Imaginary part	Real part	Imaginary part
Phugoid	0.06	1.00	0.05	0.94
Short period	-4.90	3.10	-3.70	3.75
Dutch roll	-0.93	4.10	-0.77	3.23
Spiral	0.18	0.00	0.17	0.00
Roll	-20.00	0.00	-17.99	0.00

Table 2.12: Eigenvalues of the aircraft's dynamic modes during the forward flight phase at cruise speed ($V = 15\text{m/s}$), previous model from [2] and improved model.

Mode	Previous model of [2]		Improved model	
	Frequency [Hz]	Damping	Frequency [Hz]	Damping
Phugoid	1.06	-0.05	0.95	-0.05
Short period	5.80	0.84	5.27	0.70
Dutch roll	4.21	0.22	3.32	0.23
Spiral	0.17	-1.00	0.17	-1.00
Roll	20.24	1.00	17.99	1.00

Table 2.13: Frequency and damping of the aircraft's dynamic modes during the forward flight phase at cruise speed ($V = 15\text{m/s}$), previous model from [2] and improved model.

Chapter 3

Multicopter control

In this chapter the problem of controlling the eVTOL in multicopter mode is considered. First the stock controller of the PX4 autopilot is investigated (first section) and due to tuning problems it presents, a custom architecture is implemented and tuned. The second section presents the controller, the third one the procedure to tune it in simulation while the fourth one is related to the in-flight tuning. The last section presents the performance of the tuned controller.

3.1 Stock controller

The first attempt to fly the drone has been made using the stock multicopter controller provided in the PX4 autopilot ([23]): this configuration has already been used in the laboratory on several drones, even if of different sizes and configurations ([10],[13]). In the case of the VTOL the behaviour of the stock multicopter controller is different: dangerous oscillations occurred during the test flights, both as a response to a pilot command and as a response to external disturbances. It is important to notice that, during the indoor flight testing activity, the large air mass moved by the motors generates vortices that are picked up by the wings, causing oscillations. An example of the first flight tests is shown in Figure 3.1: the oscillations are divergent on the pitch axis, leading to the emergency landing of the aircraft. In Figure 3.2, instead, the response to a position command is shown: the drone is in hovering condition, oriented in the north direction, and a move-forward command is given (at $t = 147$ s and $t = 159$ s). This generates large and poorly damped oscillations on the pitch axis. Considering the results gathered in the first flight experiments it is clear that the controller needs to be tuned. It has been decided to tune the gains of the controller in simulation to reduce the risk of accidents compared to a in-flight tuning. A *Simulink* model was developed in [1] and [2]; as explained in [2], no control system has been included in this model so it is mandatory to add it. The architecture of the controller has to be reproduced precisely in *Simulink*. PX4 is an open source autopilot, the control architecture

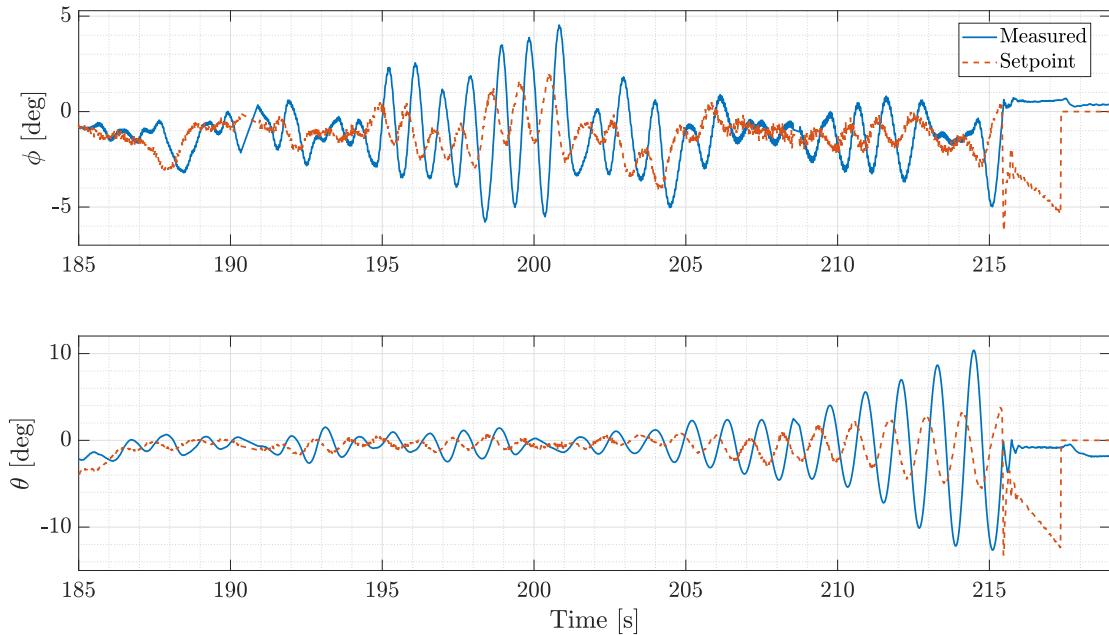


Figure 3.1: Oscillation of roll angle ϕ and pitch angle θ ; the divergence in the pitch axis is clearly visible.

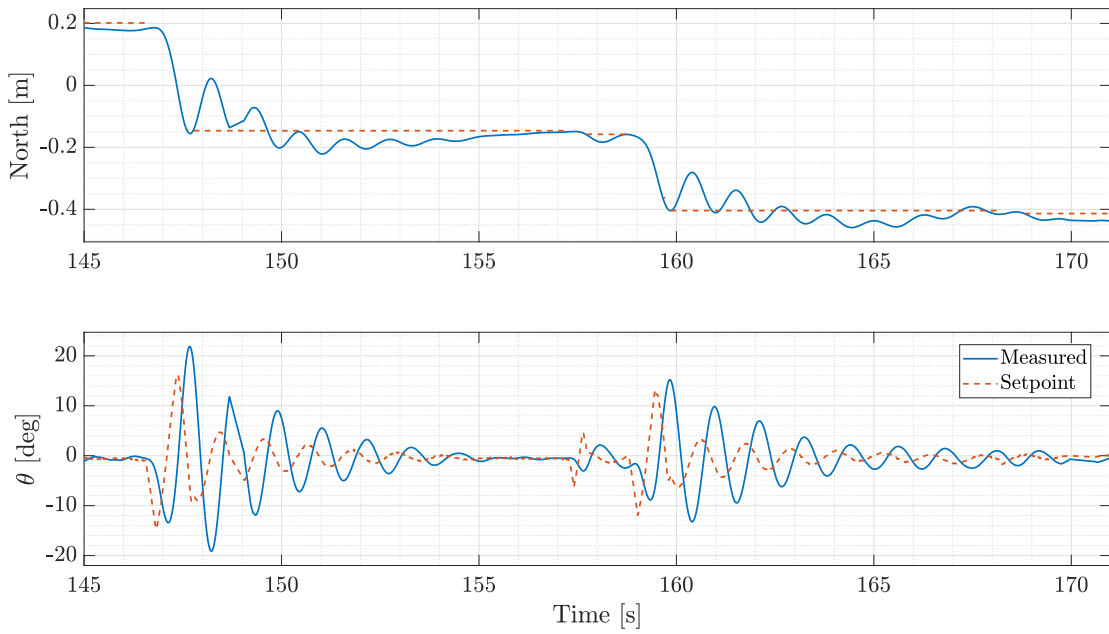


Figure 3.2: Position and pitch angle θ during a move-forward maneuver.

is explained in the documentation ([24]), but the exact structure and its high level control architecture is not known: since several normalization and scaling factors are present. This problem has already been addressed in the laboratory: reverse engineering has been made on the source code in order to exactly reproduce the controller, making possible to perform accurate simulations. The resulting model has been successfully used several time for control design purposes. Unfortunately, the obtained control scheme refers to an old version of PX4 firmware (1.7.3.beta); on the VTOL a newest version is installed (1.11.3 dev) due to a better support for VTOL configurations. Some modifications have been introduced from one version to the other, making the already developed controller *Simulink* model unusable: an attempt has been made with it but the simulated response has no match with real one. An in-depth investigation of the available documentation was made, but without results. Then, two options are available:

- reverse engineering on the new firmware, in order to correctly characterize it and build a *Simulink* model of the stock controller. This:
 - involves a difficult and long process to study the firmware starting from the source code since the available documentation ([23] and [25]) is lacking. The same work must be done on fixed-wing and transition controllers, in order to be able to simulate them;
 - allows to use a ready product: the controllers of all the configurations (multicopter, transition and fixed wing) are already implemented, tested and consolidated, only the tuning of the parameters is requested;
- design a custom controller and install it on the VTOL with SLXtoPX4 application (developed in [26]). This option:
 - presents full flexibility since any type of controller can be implemented, simulated and used;
 - allows the fixed-wing and transition controllers to be designed from scratch;
 - requires some testing since the SLXtoPX4 application has never been used for fixed-wing and VTOL configurations.

Both options have positive and negative aspects and both require a non negligible effort. With the first one, the results obtained are relative to a specific version of the firmware but may be unsuitable for future versions. The second one allows to focus entirely on the control design and the result obtained are more instructive and useful for future works, both in terms of algorithm and usage of SLXtoPX4 tool. Then, the choice fell on the second option: the multicopter, fixed-wing and transition controllers need to be designed and implemented in *Simulink*, then converted and installed on VTOL with SLXtoPX4 tool.

3.2 Multicopter controller

The selected multicopter controller architecture is made up of standard cascaded loops with PID controllers derived from [24]. Four loops are present: on the body angular rates, on the attitude angles, on the inertial velocity and on the inertial position. The structure of the controller is depicted in Figure 3.3: a proportional controller P is used for position and attitude control, while a proportional, integral and derivative PID controller is used for rates and velocity control. The final

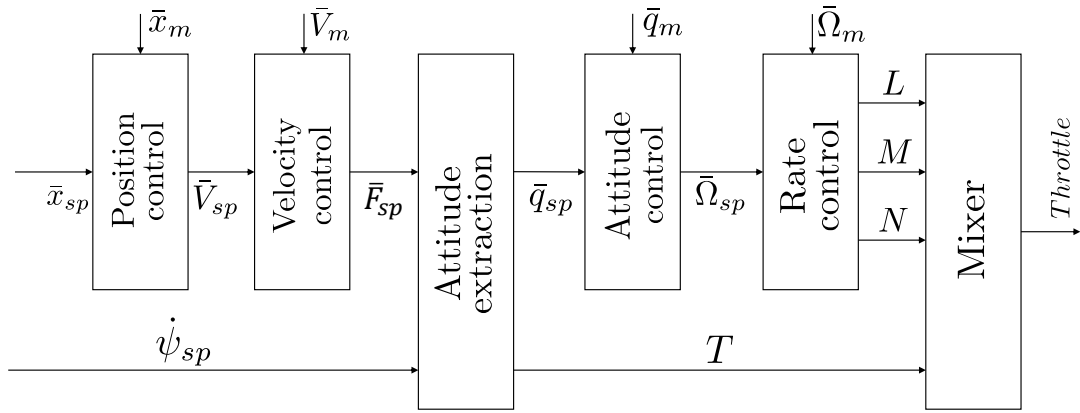


Figure 3.3: Multicopter controller.

outputs of the controller are vertical body force T and body moments L, M, N : these are converted into motors angular velocities Ω with the pseudo inverse of the mixer matrix χ (Chapter 1) and then into throttle commands th with the relation:

$$th = a\Omega^2 + b\Omega, \quad (3.1)$$

found in Chapter 2.

The attitude controller is based on [27] and makes use of quaternions ($[q_x \ q_y \ q_z \ q_w]$). The drone is an underactuated mechanical system since it has a lower number of control inputs than the number of degrees of freedom to be controlled: the force generated is oriented in the body vertical direction, so it can only accelerate along this axis. Therefore, the force setpoint \bar{F}_{sp} calculated by the velocity controller is transformed into a target orientation \bar{q}_{sp} , such that the corresponding z-axis is aligned with the desired force.

Thanks to the cascade loop structure, different flight modes are implemented. Flight modes define how the controller responds to remote control inputs, provid-

ing different levels of assistance to the pilot. This is achieved by managing the control loops activated. A full description of the flight modes is given in Appendix A for the interested reader.

The *Simulink* implementation of the controller is shown in Figure 3.4. Three main subsystem are visible:

- position controller block, that calculates the body force T and the desired attitude from position/velocity setpoint;
- attitude controller block, that calculate body moments L, M, N from attitude setpoint;
- mixer block that transforms force and moments into throttle commands.

The details of the position controller block are shown in Figure 3.5: there are the position control, velocity control and the setpoint attitude extraction subsystem. Saturation limits are introduced in order to account for the propulsion limits. An integral reset flag is added to avoid the continuous error integration by the controller when the multirotor is not flying: if the thrust command value is below 20%, the integration is stopped. There is a feed-forward term on the acceleration setpoint and the constant force contribution of the weight is considered. The *in_plane_thrust_suppression* block manages the force contribution when the drone is on ground: in this condition the force is maintained to idle value until the thrust command reaches 20%. In addition, during ALTITUDE MODE, the *in_plane_thrust_suppression* block cancels the horizontal component of the force. In Figure 3.6 the attitude controller block is depicted, composed by attitude and rate control with saturation limits and integral reset. In the end, the controller is successfully installed on the VTOL with SLXtoPX4 application.

3.2.1 Multicopter simulator

The complete simulator is depicted in Figure 3.7: the controller is connected to the VTOL model implemented in [2]. In particular, the controller uses quaternions in the form ($[q_x \ q_y \ q_z \ q_w]$), while the VTOL model the Euler angles. The setpoint is generated by the *real_set_point* block that allows to create a new trajectory or to use setpoints from past flights. State Filter blocks add noise and delay to the simulated measurements, in order to reproduce the characteristics of the real ones (Figure 3.8).

3.3 In-simulation tuning

The goal is to find a set of parameters that ensures acceptable flying qualities; in this case there is no need for high maneuverability performance. Once in flight, the parameters can be manually fine tuned; this is expected since the multirotor

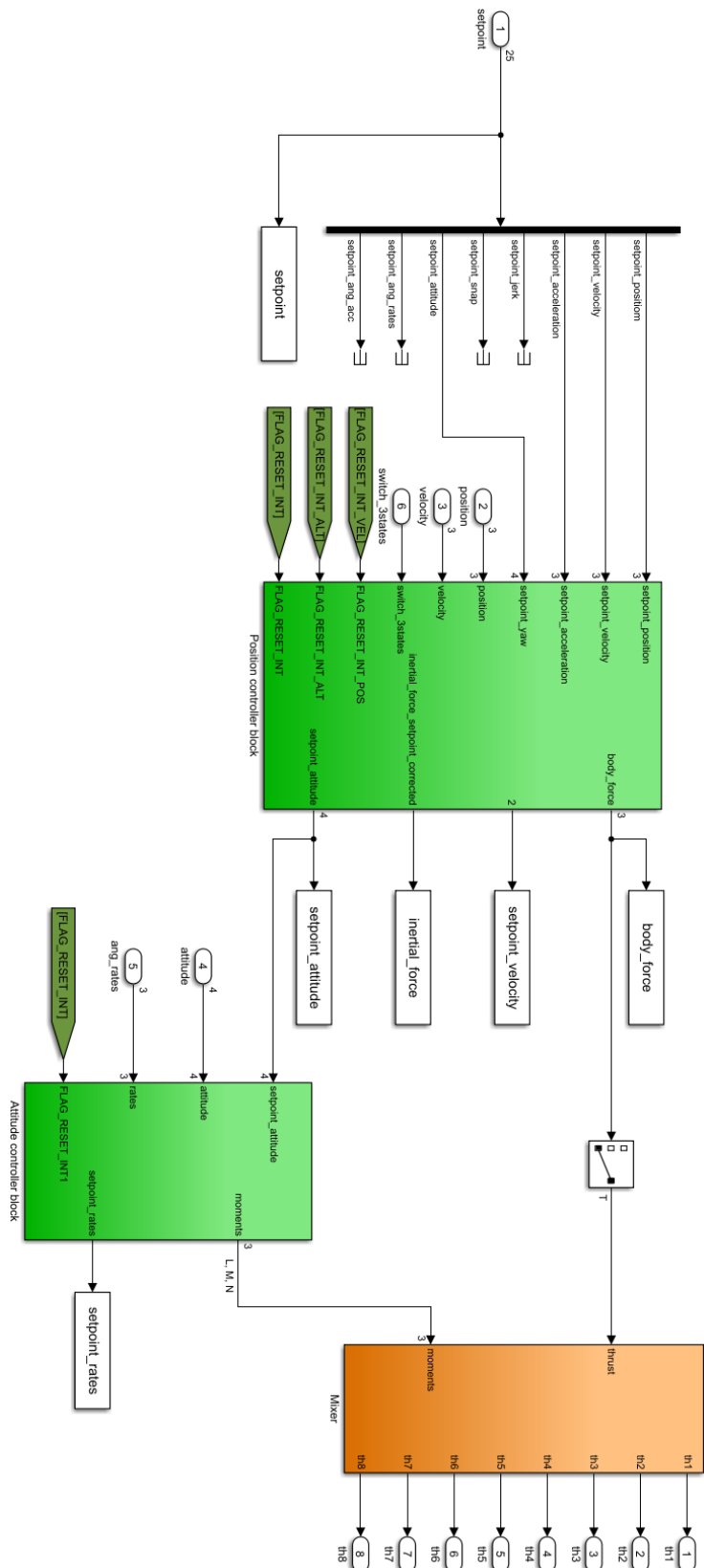


Figure 3.4: *Simulink* multicopter controller.

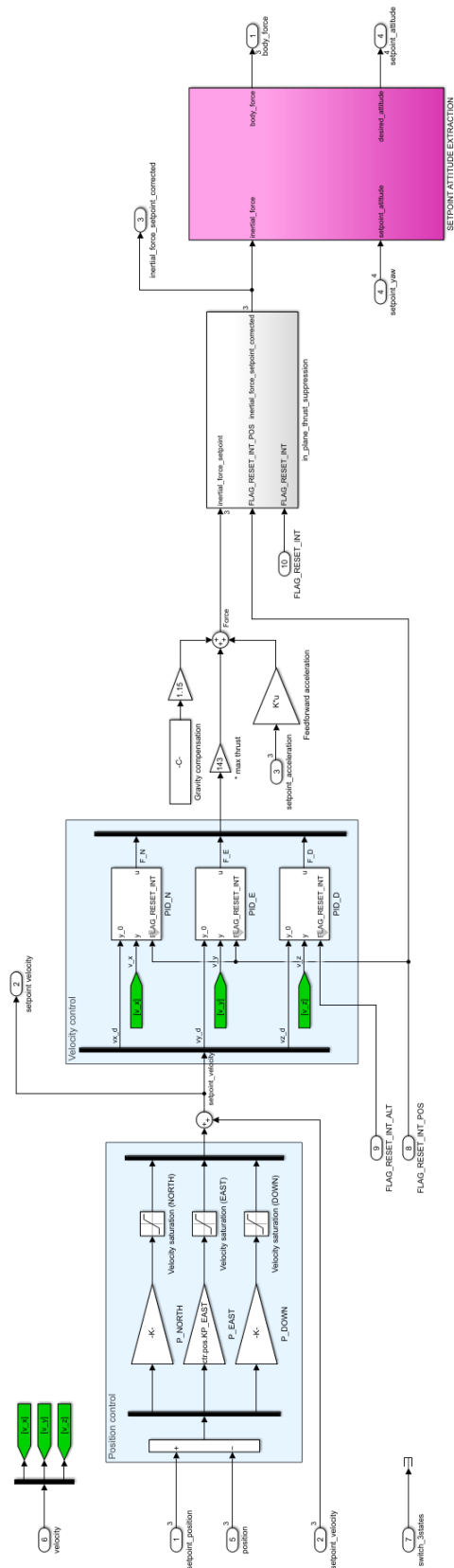


Figure 3.5: *Simulink* position control block.

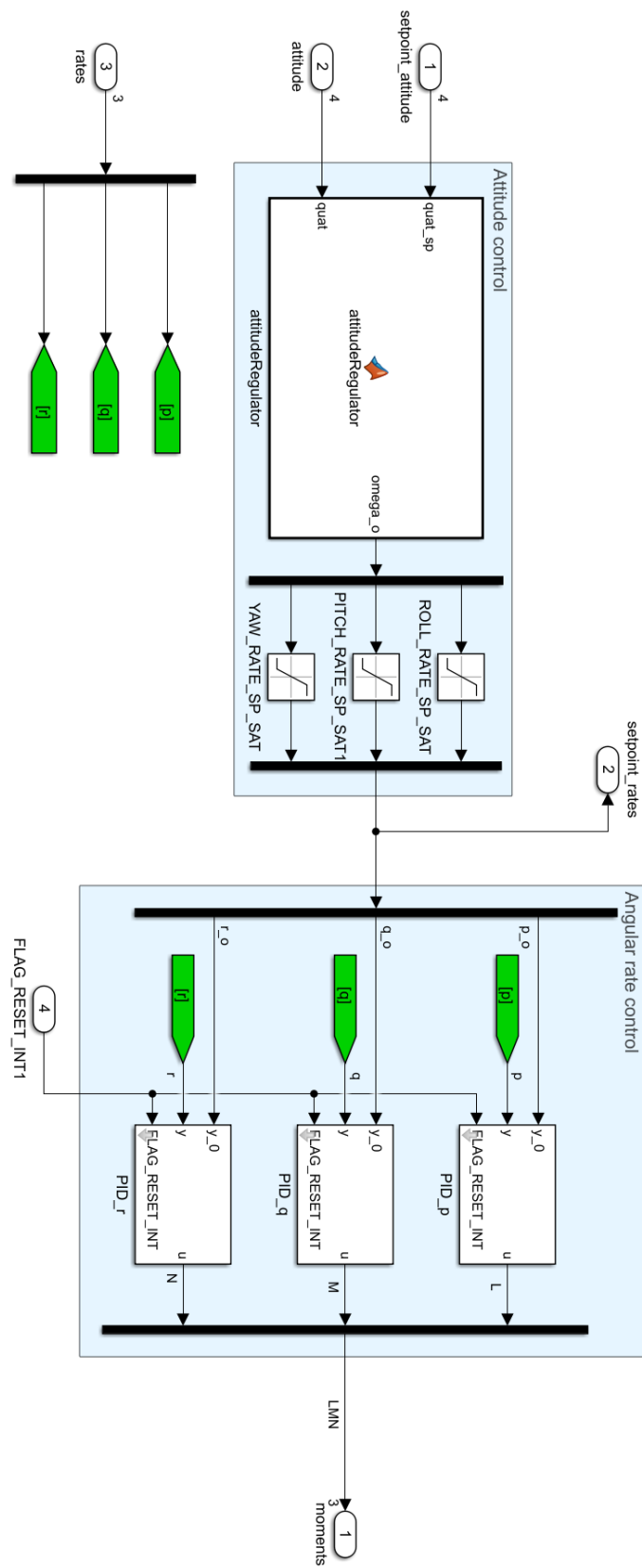


Figure 3.6: *Simulink* attitude control block.

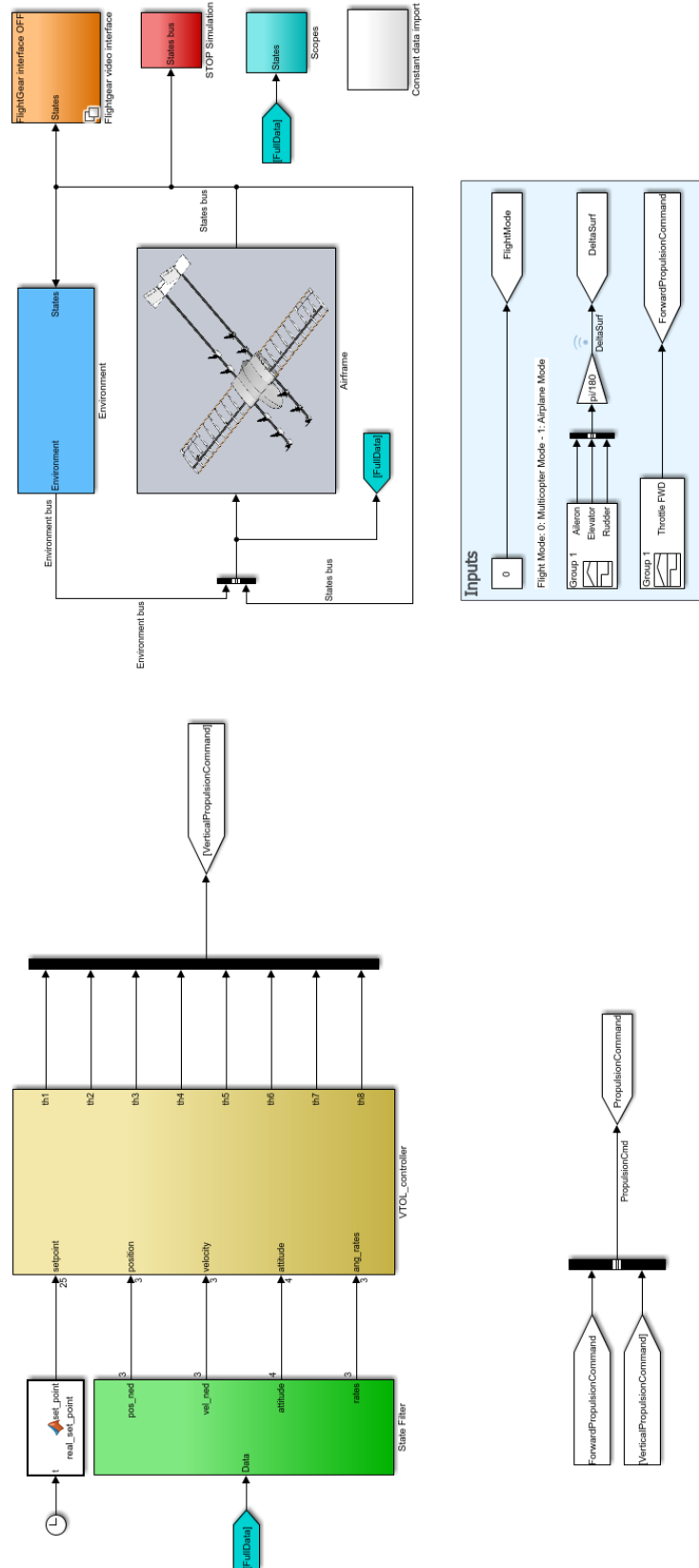


Figure 3.7: *Simulink* multicopter simulator.

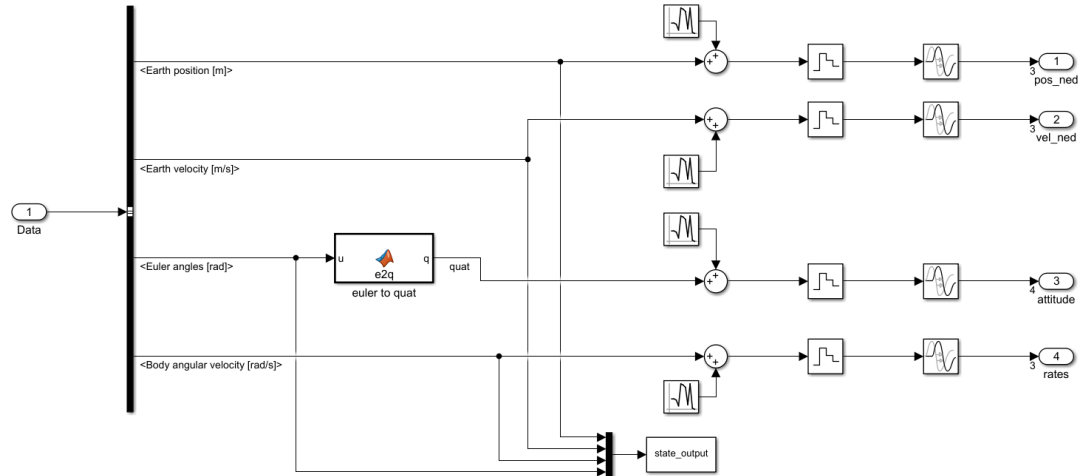


Figure 3.8: *Simulink* state filter block.

is modeled as rigid body, thus neglecting the structural model which, as seen in Chapter 2, may influence the control.

The approach used is based one the observation of the system response to a step input, considering: settling time, overshoot, oscillations and steady state error. The parameters are manually adjusted following the procedure described in [28]. Tuning is performed with a step by step procedure, in particular:

- all gains are initially set to zero;
- an axis is selected and the inner control loop on it is considered;
- the controller is tuned according to the system response to a step input along the axis of interest;
- the same procedure for the other axis;
- when all the axis are tuned, the external loop is tuned repeating the procedure one axis at a time.

In the case of angular rate controller and attitude controller, the drone is virtually constrained; only rotations about its body axis are allowed, constraining the translations. This is done by removing all the forces acting on the drone, only moments are present. This because there is no control on velocity and position, so the drone would drift and fall.

The controller parameters obtained with the tuning are summarized in Table 3.1. In Figure 3.9 are shown the step responses for roll rate, roll angle, north velocity and north position controller after the tuning of the controllers: as can be seen there are no overshoot and oscillations. The settling times are in line with the results obtained on other drones in the laboratory: in the range of tenths of a

Controller	Proportional	Integral	Derivative
Roll rate	$K_P = 9.00$	$K_I = 0.05$	$K_D = 0$
Pitch rate	$K_P = 11.00$	$K_I = 0.05$	$K_D = 0$
Yaw rate	$K_P = 8.50$	$K_I = 0.01$	$K_D = 0$
Roll angle	$K_P = 7.50$		
Pitch angle	$K_P = 3.80$		
Yaw angle	$K_P = 1.61$		
V_{North}	$K_P = 1.34$	$K_I = 0.02$	$K_D = 0$
V_{East}	$K_P = 1.34$	$K_I = 0.02$	$K_D = 0$
V_{Down}	$K_P = 1.4$	$K_I = 0.12$	$K_D = 0$
Pos_{North}	$K_P = 0.80$		
Pos_{East}	$K_P = 0.80$		
Pos_{Down}	$K_P = 0.85$		

Table 3.1: Multicopter controller gains, from tuning in simulation.

second for the attitude and rate loops and in the order of one second for position and velocity loops.

Results

The gains in Table 3.1 are implemented on the real controller and a flight test is performed: the results are worse than expected. After arming the motors (that correspond to motors in idle), the drone takes off and climbs autonomously in an abrupt way, forcing the pilot to stop the flight with the kill switch (Appendix A). The time history of the motors thrust command is analysed, with particular focus on the PWM commands (the signals given by the control unit to the ESCs to control the rotational speed of the motors). They go from a value of 1015, motor in idle, to 2015, that correspond to max thrust. The PWM commands during the test are shown in Figure 3.10; the following aspects can be notice:

- the PWM values goes from the minimum (1015) to the maximum (2015) allowable value, despite the idle command of the pilot;
- there are two separate groups of motors;
- at the same time, a group of motors is set to idle, while the other to high PWM values.

In particular, the groups are composed by motors that spin in the same direction: motor 3, motor 4, motor 5 and motor 6 spin in clockwise direction, while the others in counterclockwise direction (the motor's number is related to the FCU port at which is connected). The differentiated command between motors that spin in

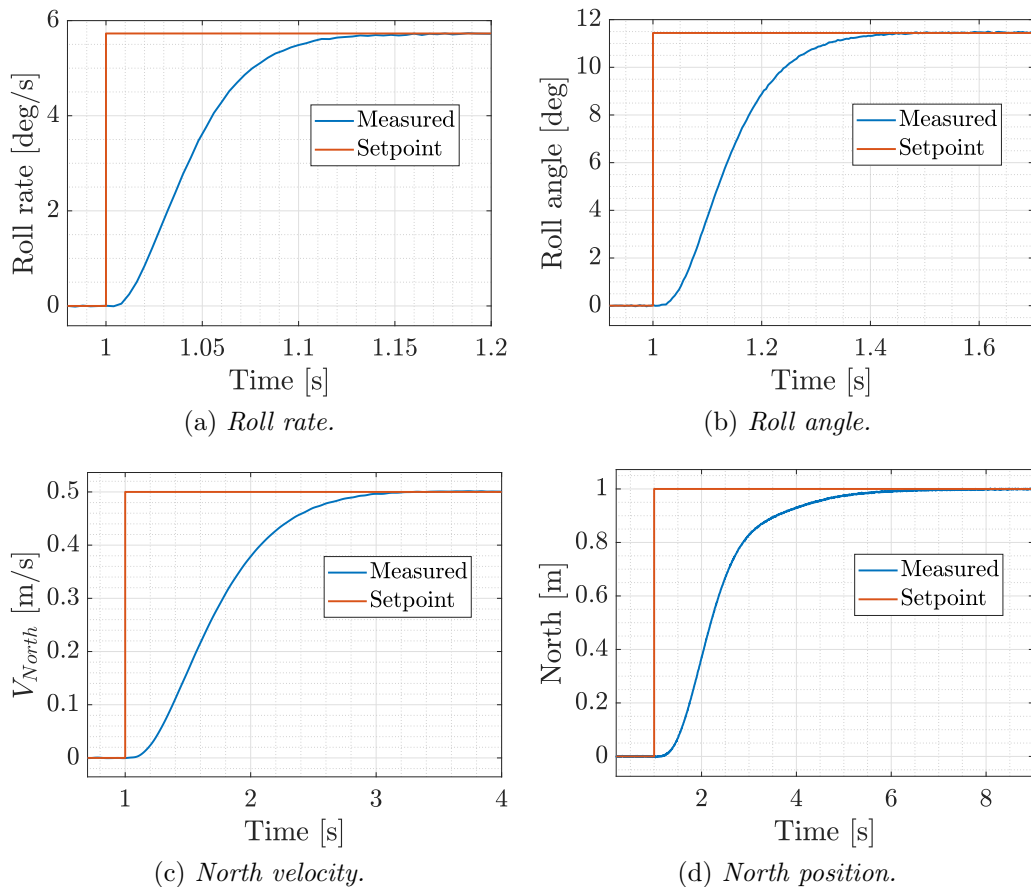


Figure 3.9: Simulated step responses with controllers tuned in simulation.

opposite direction is due to yaw control: the difference in rotation between clockwise and counterclockwise motors generate a non-zero resulting moment about the yaw axis, causing a rotation.

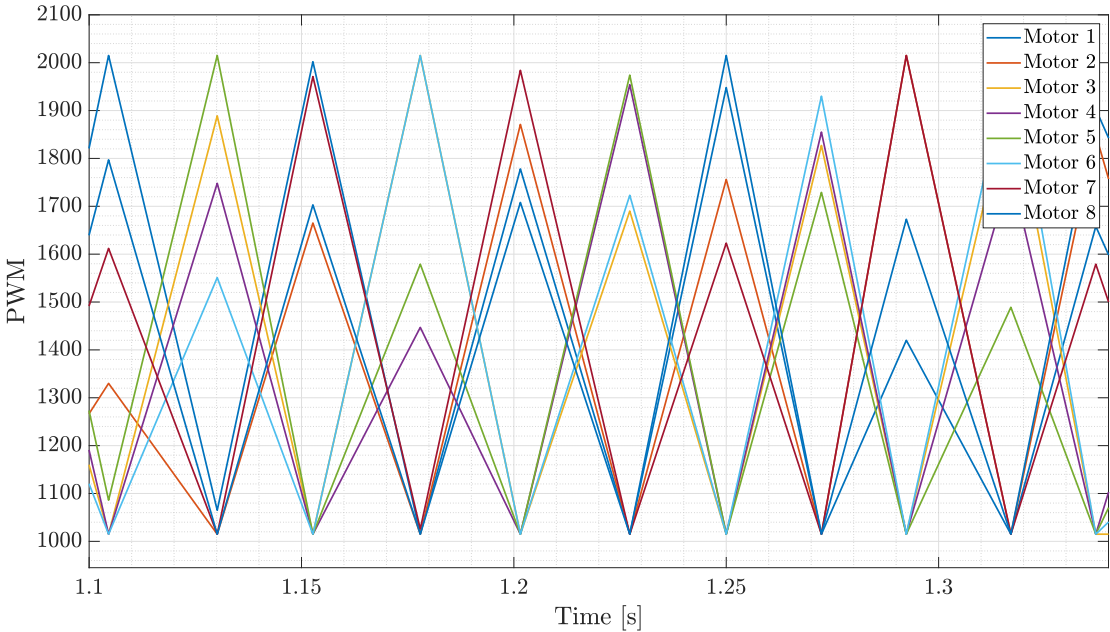


Figure 3.10: PWM motors command during the flight test with the controller gains obtained in simulation.

This yaw control action is caused by a too aggressive control: the controller reacts to the vibrations induced by the rotations of the motors, generating a chain reaction.

Typically, yaw control has no effect on altitude: the difference in rotation between the motors maintain the vertical force constant. But in this situation, to generate the large control moment required by the controller, the angular speed of the clockwise or counterclockwise motors is set to the maximum value to generate a moment about the yaw axis; this produces also a vertical force since the force of the motors that spin in the other direction can not be decreased in order to maintain the vertical equilibrium since it is already at the minimum value. So, in addition to the yaw moment, a vertical force is generated, causing the uncontrolled take off of the drone.

To verify the origin of the problem a flight is performed with the yaw control disabled (by setting to zero the control moment L). The test is performed in ALTITUDE MODE (Appendix A) in order to focus only on attitude and rate controllers. With this configuration, the problem previously encountered does not appear: the pilot can correctly arm the motors, perform a take off and fly. However, the drone results aggressive to maneuvers, making it very difficult to fly. Also strong oscillations and structural vibrations are present. So, the re-

sults obtained in simulations are not correct: the *Simulink* model is not accurate enough. Vibrations and flexibility effects are not taken into account (it is based on a rigid body), making impossible to study and predict the interactions between the controller and the structure. In Chapter 4, a more in-depth analysis about the performances of the *Simulink* model is made. It is therefore necessary to perform a in-flight manual tuning.

3.4 In-flight manual tuning

The same step by step procedure used in simulation is applied: the inner loop is the starting point, one axis at a time, then the outer loop is tuned. Thanks to the flight modes (Appendix A), it is possible to fly with different controls loop activated, acting only on the one of interest. The pilot has to perform maneuvers on the axis of interest, possibly step or doublets, that allows an easier evaluation of the system response. The controller gains are chosen according to:

- analysis of the flight data, in particular comparison of the setpoint to system response, like in simulation case;
- pilot evaluation;
- occurrence of structural vibrations.

As initial guess, small gains are chosen (about 15-20 % of the simulation parameters) and then increased slowly, 20-30% per iteration, reducing to 5-10% for final fine tuning, in order to minimize unexpected behaviors. This procedure requires an experienced pilot, fly a drone with a not tuned controller is not an easy task (especially in a limited space), and it is a time consuming process; several flights are made for each single control loop.

Results

The final gains are summarized in Table 3.2. The comparison between initial and final phase of yaw rate controller tuning is shown in Figure 3.11: the effect of the proportional term can be noticed. The effect of the integral term is evident in Figure 3.12, that shows the comparison between initial and final phases of pitch rate controller tuning. In the initial phase (Figure 3.12a), the constant error, generated by the pitch moment due to the tail weight, is not corrected. After the introduction of the integral gain (Figure 3.12b), it is corrected. Most of the time, the increase of the proportional gain is limited by the occurrence of vibrations: Figure 3.13 shows the comparison between roll rate measurement when the proportional gain of the roll angle control is increased from $K_P = 3.5$ to $K_P = 3.7$: the increase of noise, due to structural vibrations, is clearly visible. In some cases, as a result of the vibrations, an uncontrolled increase of motors

Controller	Proportional	Integral	Derivative
Roll rate	$K_P = 4.05$	$K_I = 0.05$	$K_D = 0$
Pitch rate	$K_P = 8.00$	$K_I = 1.40$	$K_D = 0$
Yaw rate	$K_P = 2.20$	$K_I = 0.25$	$K_D = 0$
Roll angle	$K_P = 3.55$		
Pitch angle	$K_P = 3.00$		
Yaw angle	$K_P = 1.20$		
V_{North}	$K_P = 0.10$	$K_I = 0.01$	$K_D = 0$
V_{East}	$K_P = 0.10$	$K_I = 0.01$	$K_D = 0$
V_{Down}	$K_P = 0.90$	$K_I = 0.15$	$K_D = 0$
Pos_{North}	$K_P = 0.60$		
Pos_{East}	$K_P = 0.60$		
Pos_{Down}	$K_P = 0.60$		

Table 3.2: Multicopter controller gains, from in-flight tuning.

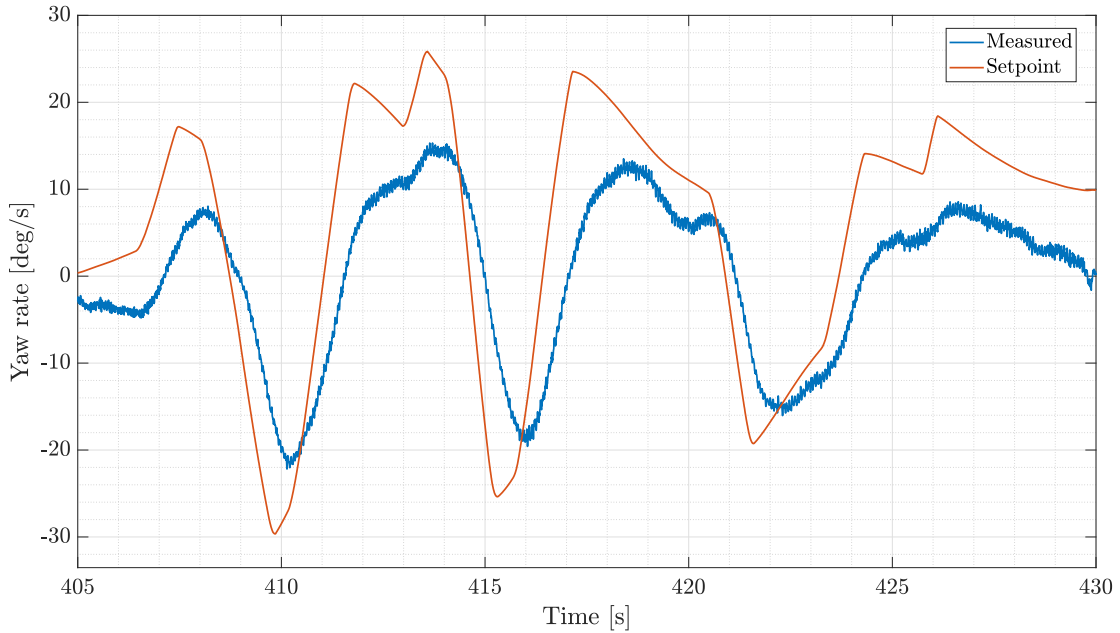
thrust is seen. This highlights the limit of the *Simulink* model: due to the flexibility of the structure, caused by configuration, size and construction limit of the VTOL, the structural dynamics has a central role in the design of the controller. The interaction between control and structural dynamics can occur with a small change of gains, causing disastrous effect.

Notch filter

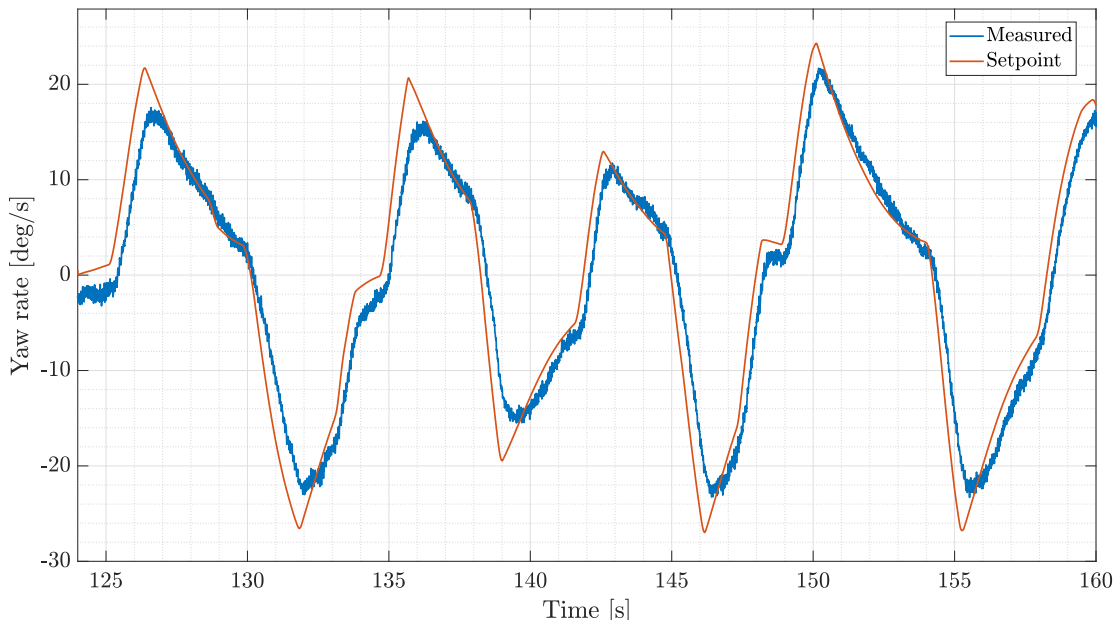
During the tuning phase, particular attention was made in the choice of the proportional gains in order to find the best compromise between tracking performance and presence of vibrations. Despite this, at the end of the tuning campaign, visible vibrations are present. From a visual analysis, they originate in the wings and then propagate to the whole vehicle. A flight is performed without wings: there are no vibrations, confirming their origin. The Power Spectral Density (PSD) of the rate measurements and of the control actions is computed using MATLAB function `pwelch`. Figure 3.14 shows the result on rate measurements: a peak is present at 91.98 rad/s, particularly pronounced in the roll rate. The same contribution is present in the PSD of the control actions. So, the bending mode of the wings generates vibrations that are read and amplified by the controller. A filter is introduced in order to exclude this contribution to the controller action; the following notch filter is implemented:

$$N(s) = \frac{s^2 + 2 \cdot g \cdot d \cdot f \cdot s + f^2}{s^2 + 2 \cdot d \cdot f \cdot s + f^2}, \quad (3.2)$$

where f is the frequency of the notch, gain g controls the notch depth and the damping ratio d controls the notch width. The filter design is carried out by



(a) *Initial phase, yaw rate gains: $K_P = 1, K_I = 0$.*



(b) *Final phase, yaw rate gains: $K_P = 2.2, K_I = 0.25$.*

Figure 3.11: Yaw rate, comparison between initial and final phase of the tuning.

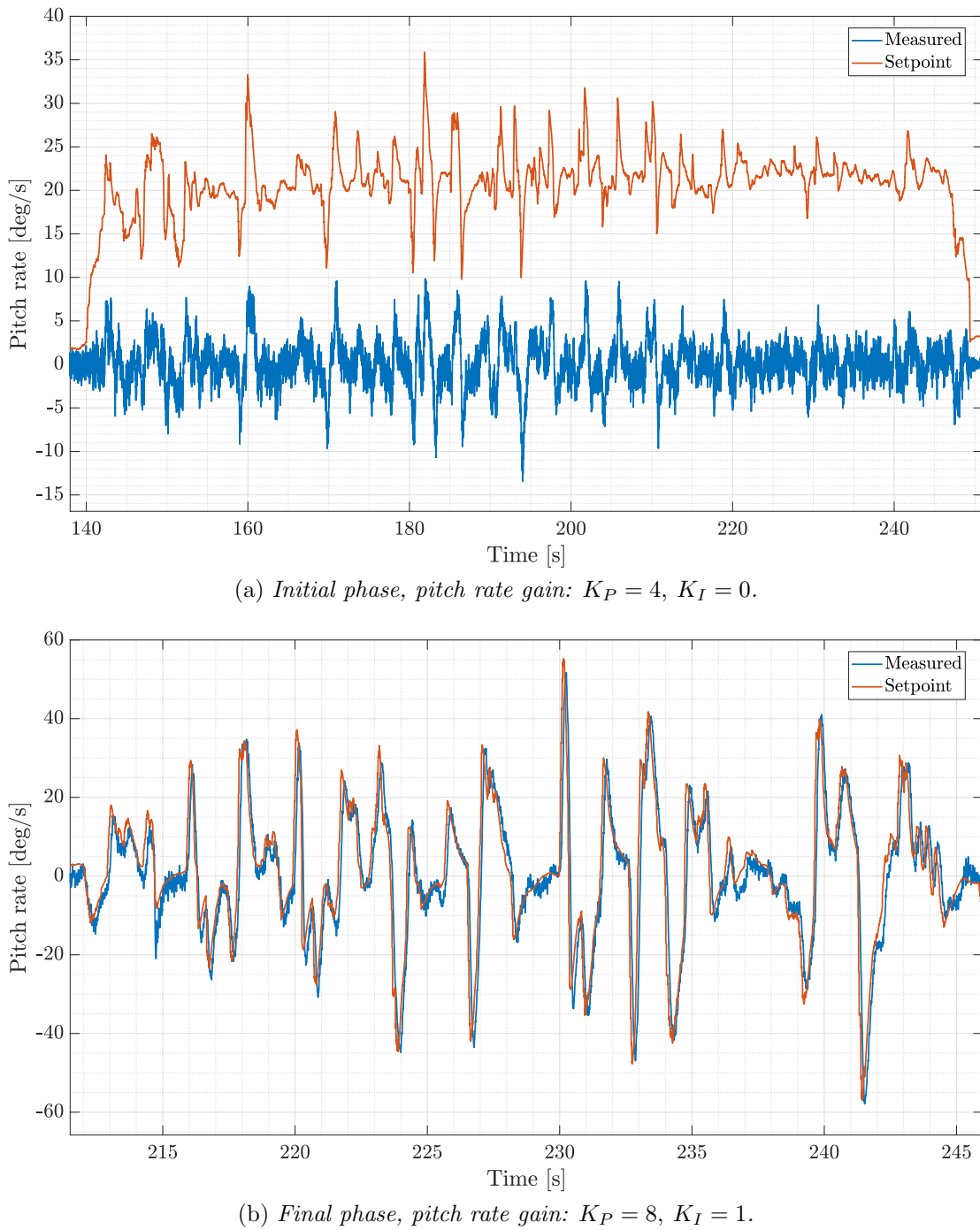


Figure 3.12: Pitch rate, comparison between initial and final phase of the tuning.

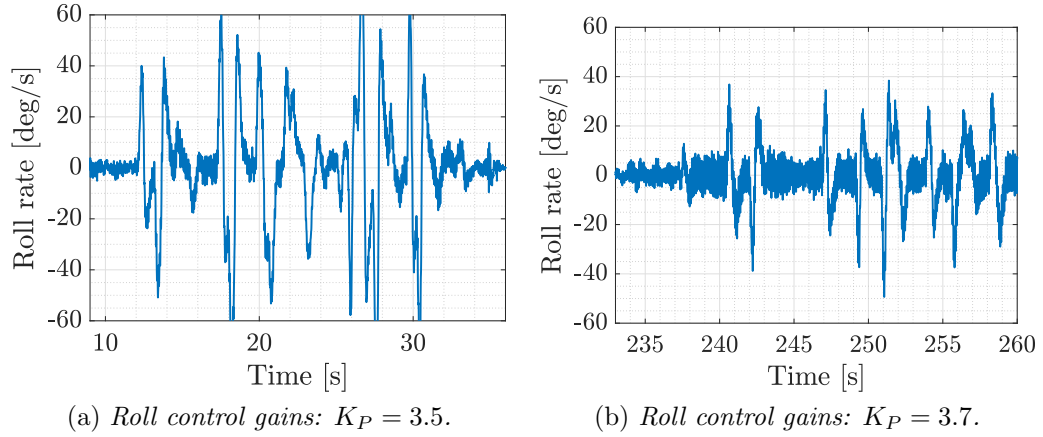


Figure 3.13: Roll rate, effect of an increase of roll angle proportional gain on noise.

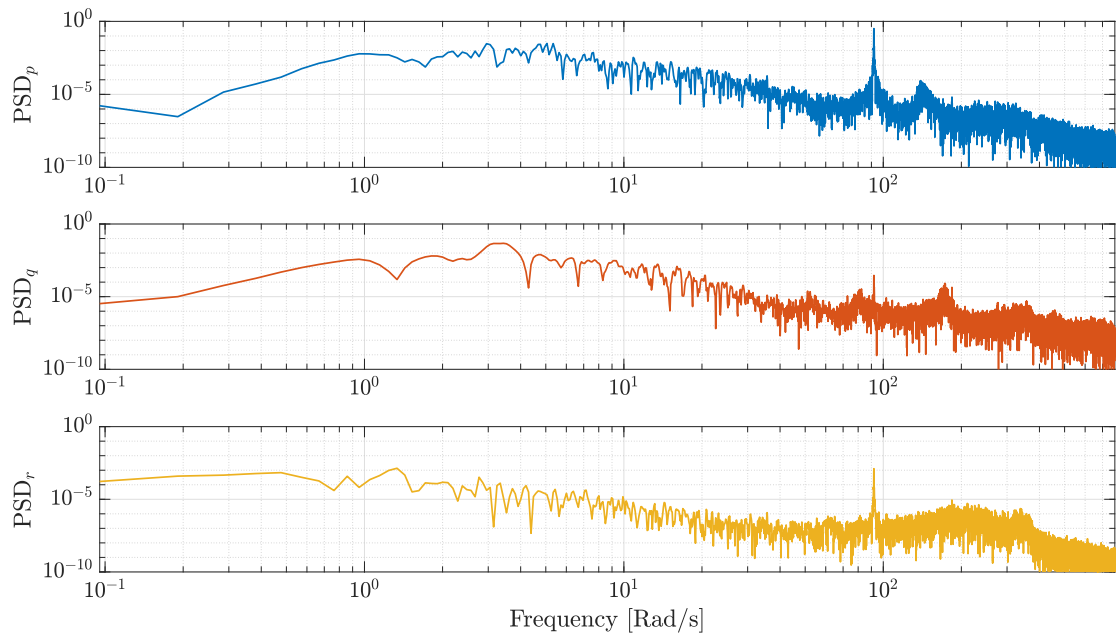


Figure 3.14: PSD of rate measurements.

f	g	d
91.98	0.0001	0.2

Table 3.3: Notch filter parameters.

studying its effect on past measurements (Figure 3.15). The Bode diagram of the final filter is depicted in Figure 3.16 and in Table 3.3 the final parameters are summarized.

The filter is then converted into discrete time (with the Tustin method) and implemented on the controller, acting only on the roll rate measurements. In Figure 3.17 the PSD of the rate measurements of a flight with the notch filter installed is depicted: the spike is no longer present. The wings vibration frequency (91.98 rad/s) can still be seen even if it is not amplified by the control action.

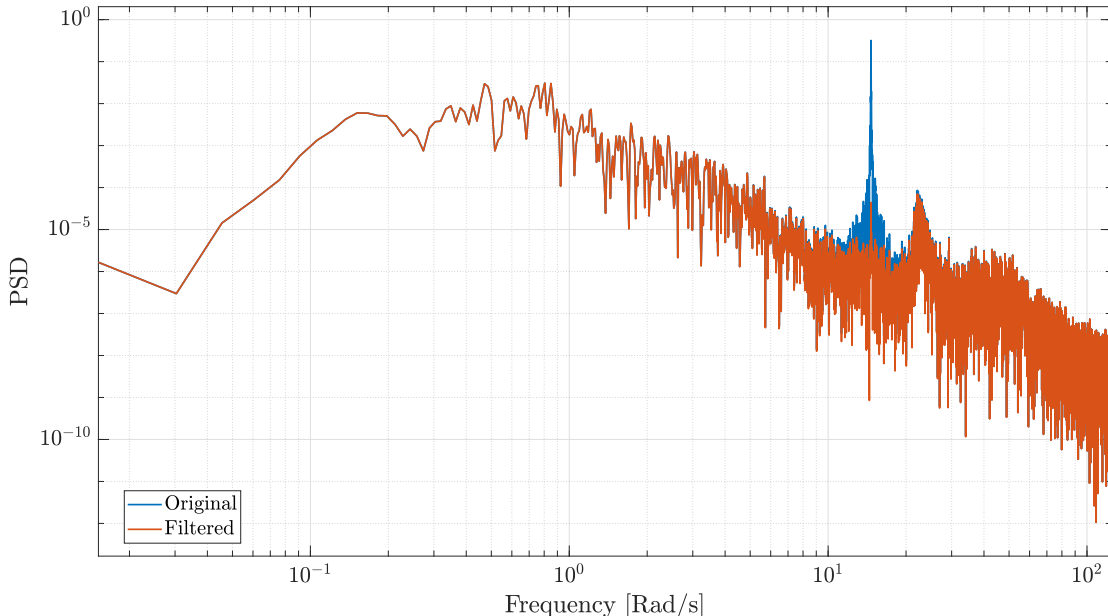


Figure 3.15: PSD of roll rate measurements, before and after filtering.

3.5 Control system performance

Several flights are performed with success in all the flight modes: the VTOL results maneuverable, easy to fly and with a good rejection of the external disturbance (the turbulence generates by the motors airflow). There are no oscillations and no dangerous behaviour are reported. In Figure 3.18 are shown the attitude angles during an hovering test of 2 min: there are no evident oscillations, despite the turbulence induced by the motor airflow. Only the yaw angle has a slow drift

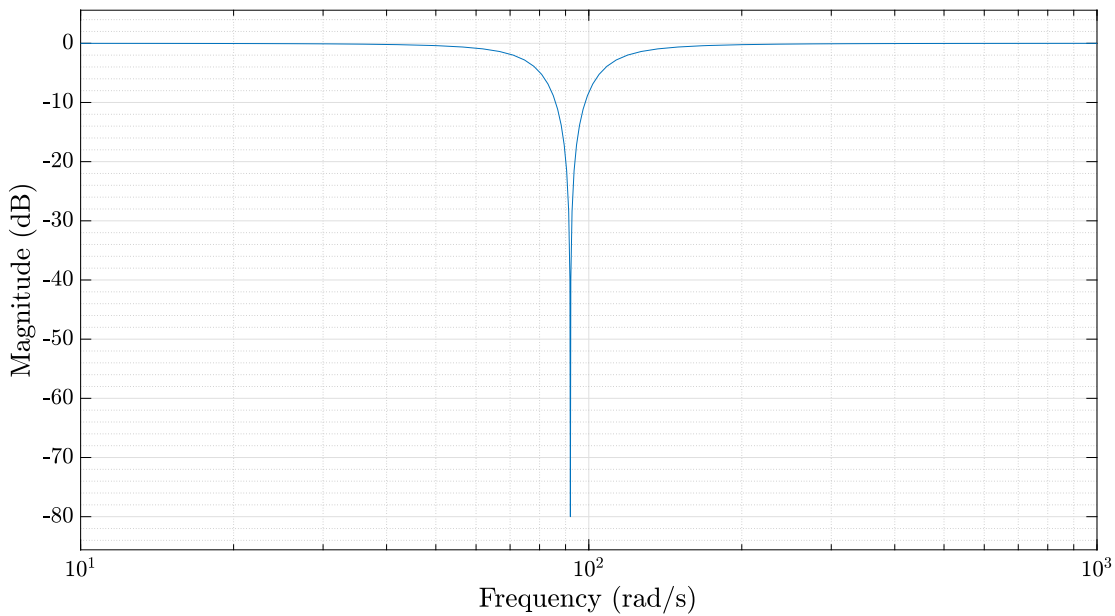


Figure 3.16: Notch filter magnitude Bode diagram.

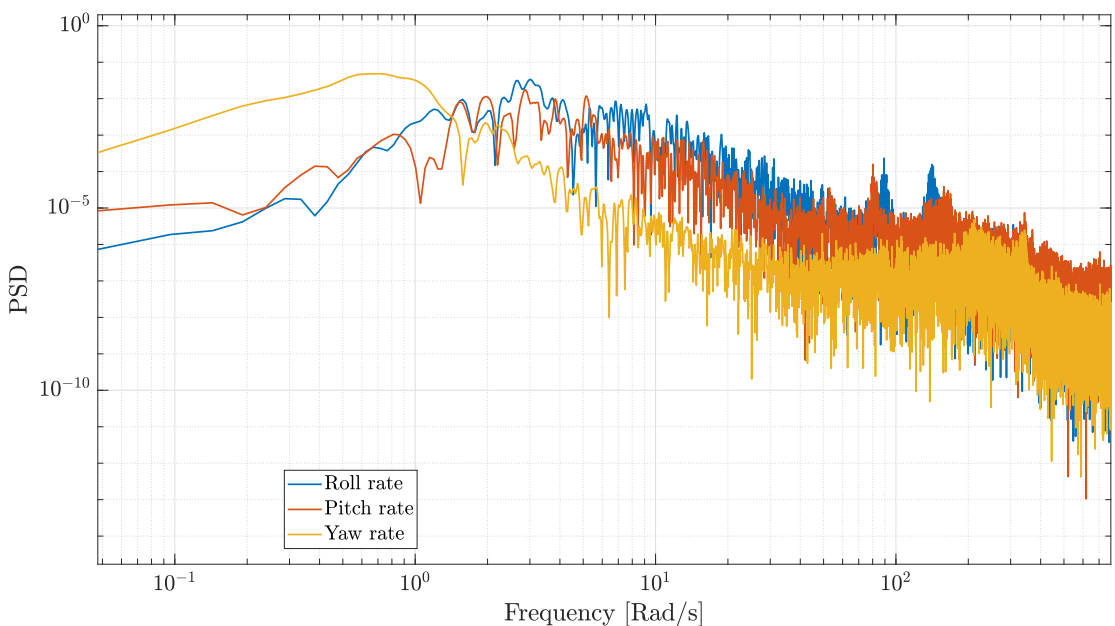


Figure 3.17: PSD of roll rate measurements of a flight with notch filter installed.

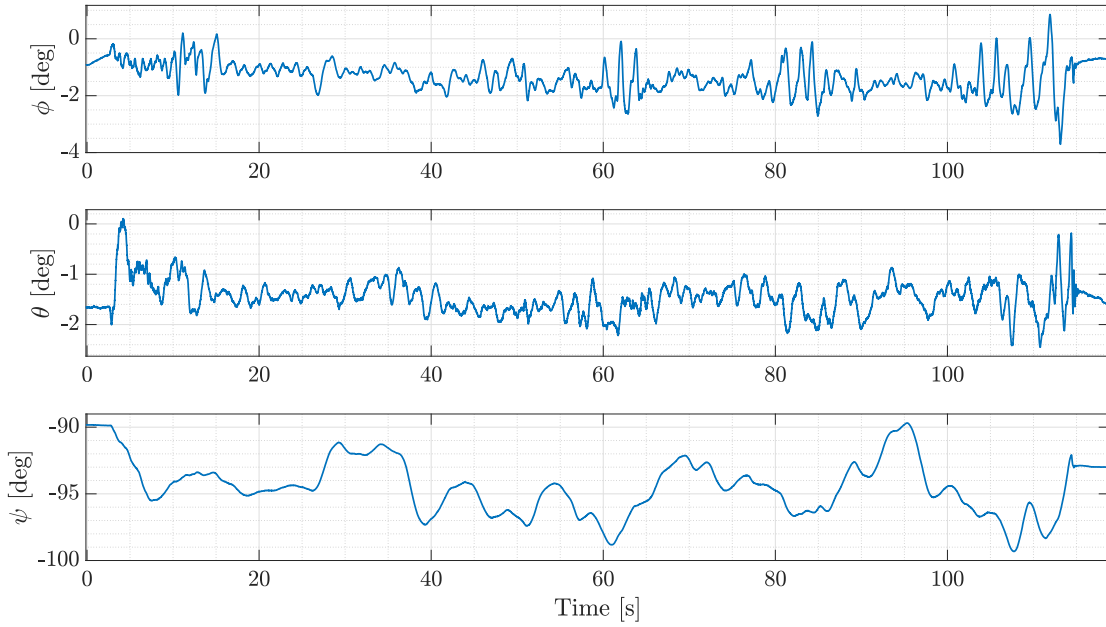


Figure 3.18: Attitude angles during an hovering test.

$(\pm 5^\circ)$.

The phase margin, gain margin and cut-off frequency of each control loop are calculated (with the multicopter dynamics model identified in Chapter 4) and summarized in Table 3.4. The phase margin and the gain margin are very large, confirming the stability of the system. The cut-off frequencies are smaller compared to other works on multirotor drones ([10]) but, considering the type of vehicle, the manual tuning procedure and the uncertainty due to the identified model, they are considered acceptable. In particular, the frequency separation between the cascade loops is guaranteed.

Controller	Phase margin	Gain margin	Cut-off frequency
Roll rate	76.8 deg	22.0 dB	9.7 rad/s
Pitch rate	63.9 deg	11.6 dB	12.5 rad/s
Yaw rate	89.0 deg	16.1 dB	2.5 rad/s
Roll angle	70.9 deg	18.9 dB	3.2 rad/s
Pitch angle	76.0 deg	16.9 dB	3.0 rad/s
Yaw angle	54.6 deg	41.0 dB	1.2 rad/s
V_{North}	67.2 deg	18.6 dB	1.2 rad/s
V_{East}	65.5 deg	20.6 dB	1.1 rad/s
V_{Down}	93.7 deg	57.2 dB	0.5 rad/s
Pos_{North}	53.5 deg	12.9 dB	0.6 rad/s
Pos_{East}	52.7 deg	12.0 dB	0.6 rad/s
Pos_{Down}	48.5 deg	38.4 dB	0.1 rad/s

Table 3.4: Multicopter controller valuation.

Chapter 4

Multicopter dynamics identification

Following the preliminary tuning of the multicopter controller, it is possible to conduct an identification campaign. We are interested in the identification of the lateral, longitudinal, directional and vertical dynamics. In particular:

- lateral: from roll moment L to roll rate p ;
- longitudinal: from pitch moment M to pitch rate q ;
- directional: from yaw moment N to yaw rate r ;
- vertical: from force T to vertical speed v_z .

The chapter is organized as follows: a short overview of the black-box model identification method used is given, then the model dynamics is identified. In the end, the identified dynamics is compared with the previous Simulink simulator with 6 DOF dynamics (see [2]) to verify its accuracy against the identified dynamics.

4.1 Black box identification

The identification is carried out with a black-box approach; the optimized version of the Predictor Based Subspace Identification method ($PBSID_{opt}$) is used. $PBSID_{opt}$ is a suitable and efficient solution to obtain an unstructured state-space model; it is a direct method, not iterative and fast computing, as presented in [13]. The typical limitation is that it provides a model representation that is not physically-motivated.

The implementation of $PBSID_{opt}$ used in this thesis is part of the PBSID Toolbox developed by Technische Universiteit Delft researchers as an implementation of utilities for system identification with PBSID algorithms in the MATLAB environment ([29]). $PBSID_{opt}$ allows to choose the order n of the unstructured model,

the parameters p and f (past and future horizon), the regularization method and the constraint on the presence of direct feedthrough (D matrix of the state space model).

This approach has been used in [10] and deeply analysed in [13] for longitudinal and lateral dynamics. The analysis is focused on the subspace identification problem, with the aim to understand the role of the constraints on the model structure and of the regularization method. The approach used is based on a sensitivity analysis of the estimated models to choose $PBSID_{opt}$ parameters (n, p, f) considering different options or constraints; multiple validation criterion both in time-domain and in frequency-domain are used. The analysis is performed in a pragmatic sense; any assumption and design choice is motivated by the support of experimental evidence. The following conclusions are made and they are used, in the present work, as reference points:

- best cross-validation results in terms of Variance Accounted For (VAF, a validation index that will be introduced in Section 4.3) are obtained for model order n larger than the order of the physical model for lateral dynamics. The singular values criterion, according with the order n can be selected by spotting noticeable gap between the plotted singular values, is supported by the experimental evidence;
- the accuracy of the estimates gradually improves for increasing values of the parameters p and f , as the black-box model is able to better approximate the zero located at the origin. Maximum bias and efficiency index have a trend converging to a minimum for large horizon parameters values;
- Tikhonov regularization method ([30]) has an important role on the asymptotic variance of $PBSID_{opt}$ estimate; in fact, the least squares problem becomes heavily ill-conditioned when large past horizon value is chosen. This issue is present also when direct feedthrough in the model is neglected;
- with the application of the regularization method, the accuracy of the estimated model is considerably improved for a choice of p and f large enough; the efficiency index obtained by constraining the direct feedthrough indicates significant lower asymptotic variance.

4.2 Experiments description

For safety reasons, the experiments are carried out in close-loop conditions; the position control is active to stabilize the drone around hover. The excitation signal (force or moment) is injected by adding it to the control actions of the controller, just before the mixer matrix. Different types of excitation signal are considered for an in-depth investigation:

- Pseudo Random Binary Sequence (PRBS): it consists in step commands of constant amplitude but having width and sign that is randomly generated, able to excite a wide range of frequencies in a short time window (Figure 4.2);
- frequency sweep: it is a periodic excitation with a linearly-increasing frequency from a minimum to a maximum over a long time interval while maintaining a constant amplitude (Figure 4.7);
- manually piloted maneuvers: representative of a more realistic situation, they are used only for model validation. Validation flights are performed in ALTITUDE MODE (Appendix A); the hovering condition is perturbed with oscillations around the lateral and longitudinal axis independently. The quality of the validation data is better when only the interested dynamics is excited while the others not ([13]). Figure 4.1 shows a flight for longitudinal dynamics validation and a suitable time-window.

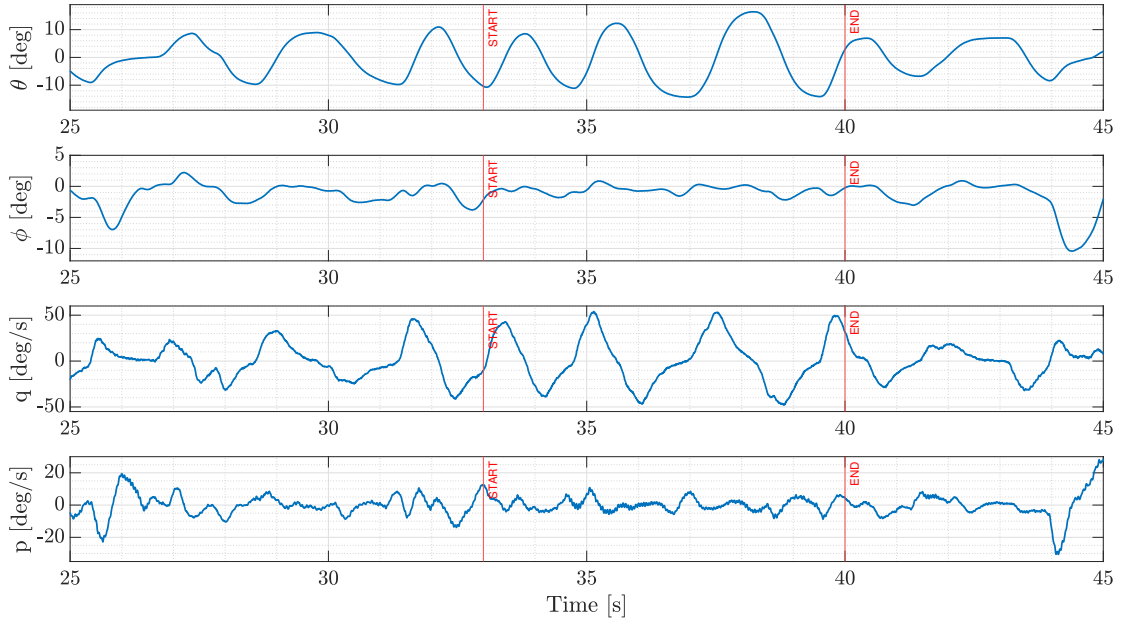


Figure 4.1: Data time-histories (pitch angle θ , roll angle ϕ , pitch rate q and roll rate p) of longitudinal dynamics validation fight test; a suitable time-window is chosen where the lateral quantities are small.

The flight tests (in the PRBS and frequency sweep cases) are carried out in OFF-BOARD MODE (Appendix A) and consist in: take-off, hovering, automated excitation of the relevant dynamics, recover of hovering condition and landing. The excitation signals utilized are described in Table 4.1 and Table 4.2: the values used are chosen according to past experience ([10],[31]) and then adjusted by observation of the behaviour of the vehicle during the test. The duration of the tests

Dynamics	Max frequency	Amplitude	Duration
Lateral	20 rad/s	10 % L_{max}	20 s
Longitudinal	20 rad/s	10 % M_{max}	20 s
Directional	15 rad/s	20 % N_{max}	20 s
Vertical	10 rad/s	7 % F_{max}	20 s

Table 4.1: PRBS excitation signals.

Dynamics	Min frequency	Max frequency	Amplitude	Duration
Lateral	0.3 rad/s	10 rad/s	10 % L_{max}	30 s
Longitudinal	0.3 rad/s	10 rad/s	10 % M_{max}	30 s

Table 4.2: Frequency sweep excitation signals.

is limited by the discharge of the batteries: during the excitation a significant voltage drop occurs. The data collected are:

- excitation signals injected into control systems (L, M, N, F),
- total input command given to actuators ($L_{tot}, M_{tot}, N_{tot}, F_{tot}$),
- body rates (p, q, r) and vertical velocity (v_z).

In Figure 4.2 the data of a lateral dynamics identification test are depicted.

PRBS and frequency sweep excitation signals are used for identification dataset while, for validation purpose, manually piloted maneuvers and PRBS (different dataset from the one used for system identification) are used.

These are preprocessed in order to eliminate offsets and trends induced by feedback (by removing the mean value) and to remove delay (only in identification phase), estimated with the MATLAB function *delayest*.

4.3 Identification

Different combinations of $PBSID_{opt}$ parameters (n, p, f) are tested and evaluated for each dynamics according to time-domain and frequency-domain requirements in order to improve the identified model. Two criteria are used in this process:

- the simulated response of the estimated model is compared with the data collected during a validation experiment and evaluated with Variance Accounted For (VAF) index defined as

$$VAF = \max \left(1 - \frac{Var[y_m - y_{est}]}{Var[y_m]}, 0 \right) 100 \%, \quad (4.1)$$

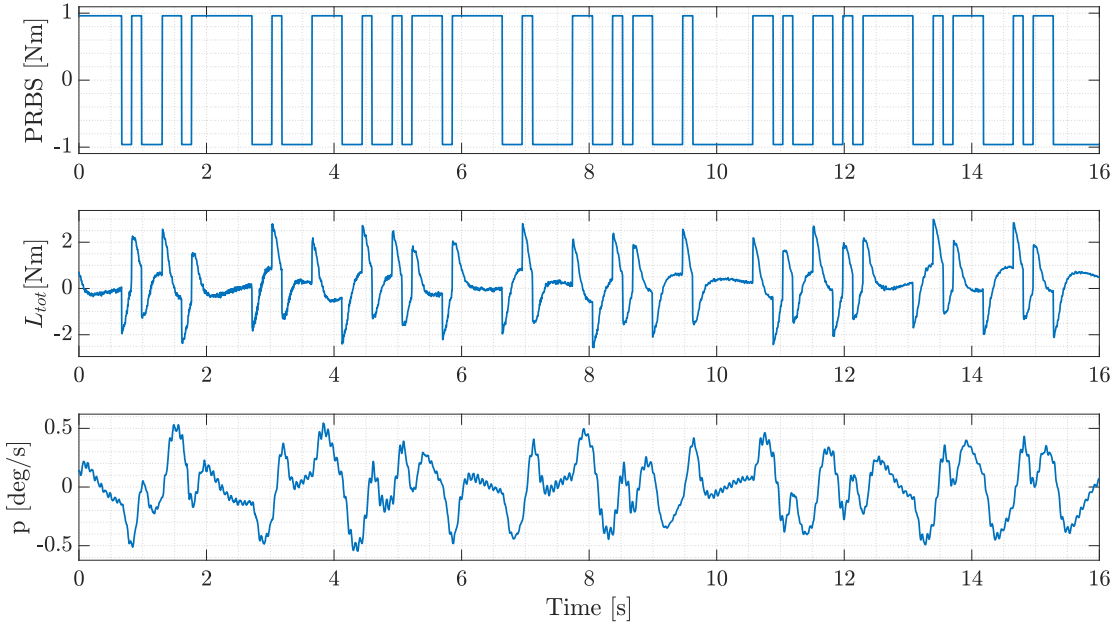


Figure 4.2: Excitation signal, total input command L_{tot} and roll rate p during an identification test.

where y_m are the measured values and y_{est} the estimated values. It is limited between 0 and 100: the larger the VAF, the better the model.

- The frequency response function (FRF) of the transfer functions of the estimated model is compared with the nonparametric estimate and the linear model (Chapter 1).

The set of parameters that produces the higher VAF and approximates better the frequency response of the nonparametric estimate is selected.

In all the tests the Tikhonov regularization method, using the Generalized Cross Validation (GCV) criterion ([32]), is applied ([13]). According to the linearized model explained in Chapter 1, all the dynamics of interest have no direct feedthrough, so matrix D is constrained to zero.

4.3.1 Longitudinal dynamics

Several trials with different combinations of $PBSID_{opt}$ parameters are made: for each model order n from 2 to 10, values of the p and f (chosen equal) ranging from 10 to 250 are considered. The range of the parameters is chosen in order to limit model complexity and according to convergence results obtained in [13]. The VAF on PRBS experiment (VAF_{PRBS}) and manually piloted maneuvers (VAF_{pilot}) are calculated; the best results are selected and evaluated in the frequency domain. PRBS excitation signal is used for the identification dataset.

	Model order n	Past horizon p	Future horizon f
Model 1	2	30	30
Model 2	6	20	20
Model 3	5	170	170

Table 4.3: Different model structures for longitudinal dynamics obtained with PRBS experiment.

Two main cases are obtained based on the order of the model:

- in the case of $n \leq 4$, acceptable values of VAF are obtained only for manually piloted maneuvers data and for horizon parameters < 40 ; in the case of PRBS validation dataset, the VAF is always low for any value of p and f . The comparison between validation on manually piloted maneuvers dataset and PRBS dataset is shown in Figure 4.3 in the case of $n = 2$ and $p = f = 30$; $VAF_{pilot} = 89\%$ and $VAF_{PRBS} = 34\%$ are obtained.
- for model orders $n > 4$ and low values of horizon parameters ($p, f < 30$), VAF_{pilot} is high ($> 90\%$) while VAF_{PRBS} has lower value ($< 40\%$). An example is depicted in Figure 4.4 for model order $n = 6$: it is possible to notice that, for a model characterized by $n = 6$ and $p = f = 20$, the VAF values are similar to the one mentioned in the previous bullet.
For model orders $n > 4$ and higher values of horizon parameters ($p, f > 30$), VAF_{pilot} decreases a little bit and settles at a constant value larger than 80% while VAF_{PRBS} increases up to a constant value larger than 60% (in Figure 4.4 the trend for model order $n = 6$).

The result with the best compromise between VAF_{pilot} and VAF_{PRBS} is obtained with model order $n = 5$ and horizon parameters $p = f = 170$ ($VAF_{pilot} = 85\%$ and $VAF_{PRBS} = 72\%$). However, two other models which maximize the VAF_{pilot} and the VAF_{PRBS} are selected for a further comparison. Table 4.3 shows them together with the model with the best compromise.

The three models are then studied in the frequency domain: the frequency response function of the estimated models is evaluated and compared to the non-parametric estimate. Exploiting the linearized model derived in Chapter 1, it is known that the transfer function is of non-zero type. From this information some considerations on the frequency response can be made. It is known that the zero in the origin can not be found because subspace identification methods always provide an unstructured model in discrete-time whose transfer functions do not have zeros or poles on the frontier of the closed unit circle ([13]). The expected shape of the frequency response function's magnitude is with a positive slope at low frequency (due to the zero at the origin) and then a change of slope due to

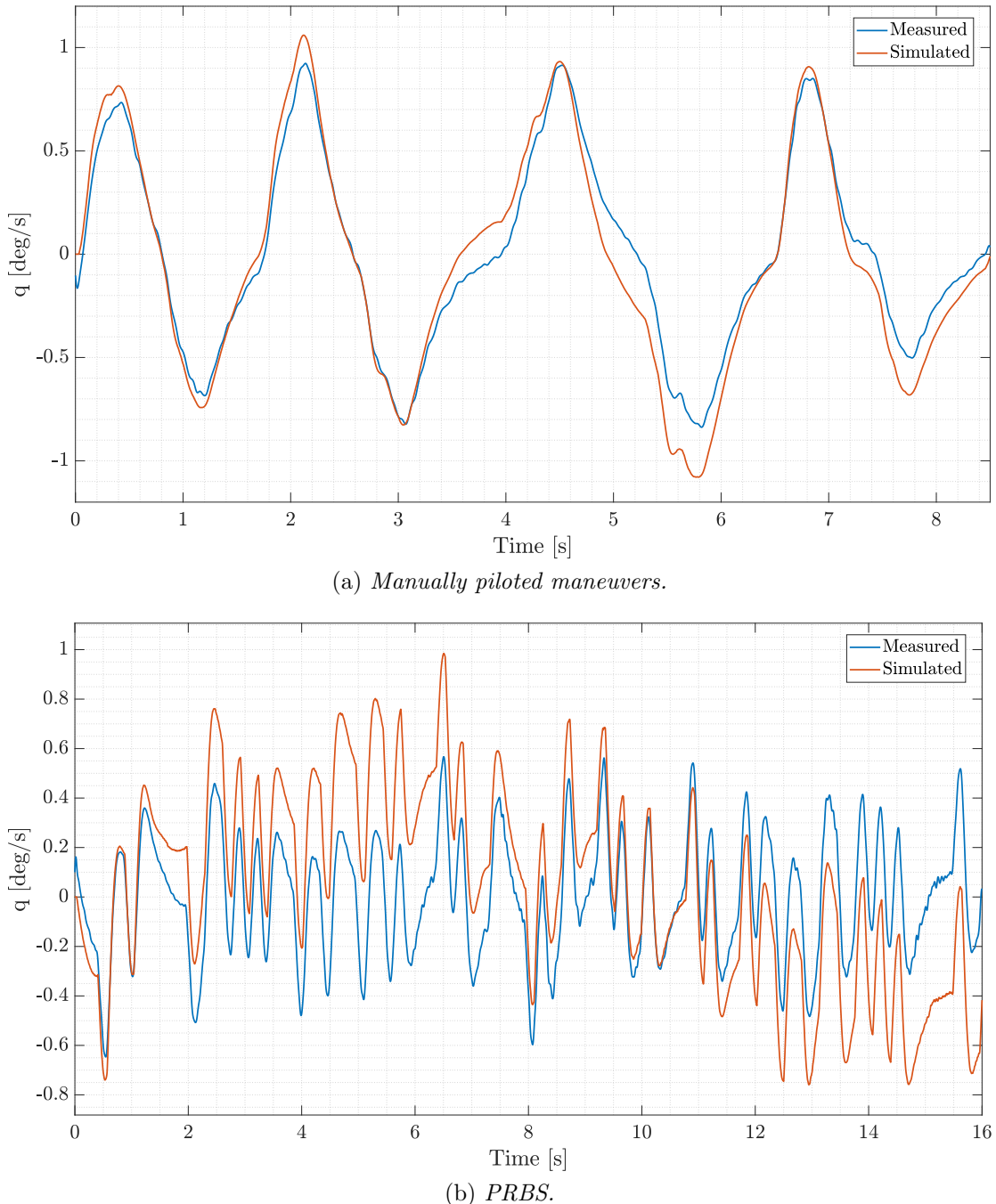


Figure 4.3: Time-domain validation for longitudinal model with $n = 2$ and $p = f = 30$.

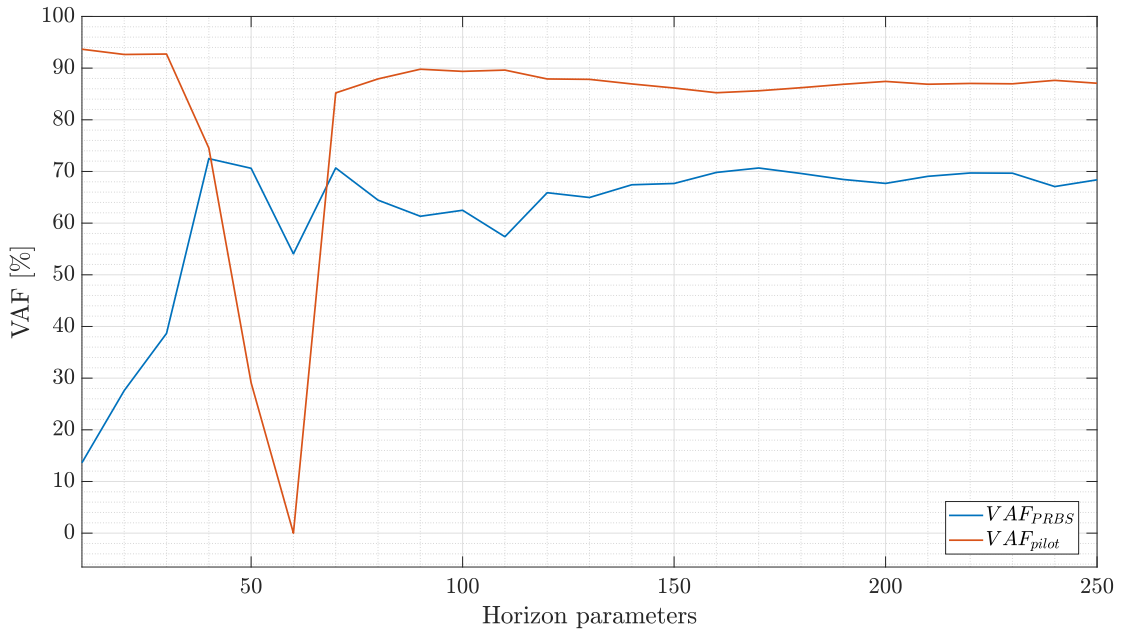


Figure 4.4: VAF index for model order $n = 6$ and increasing horizon parameter p and f .

the poles. Figure 4.5 shows the frequency response of the three models compared to the non-parametric estimate (the non-parametric estimate is obtained using MATLAB function *spaavf* from PBSID Toolbox ([29]), with a smoothing over frequencies method with averaging factor $N = 3$).

The following points can be noticed:

- very good accuracy is obtained in all the three models in the 2-30 rad/s frequency range;
- the non-parametric frequency response function has a change of slope, in accordance with non-zero type transfer function;
- below 2 rad/s:
 - model 3 catches the slope change, even if at some radian per second of difference compared to the non parametric estimate;
 - model 1 and model 2 have no slope change.

From these considerations it is possible to better understand the time-domain results. Model 1 and Model 2 have an accurate description of the model dynamics in the 2-30 rad/s frequency range, but this is obtained with a wrong structure of the system (with low frequency poles): outside this frequency range the model responses are incorrect. Since PRBS has a wider frequency content with respect to the pilot excitation, also the low frequency contribution is excited causing

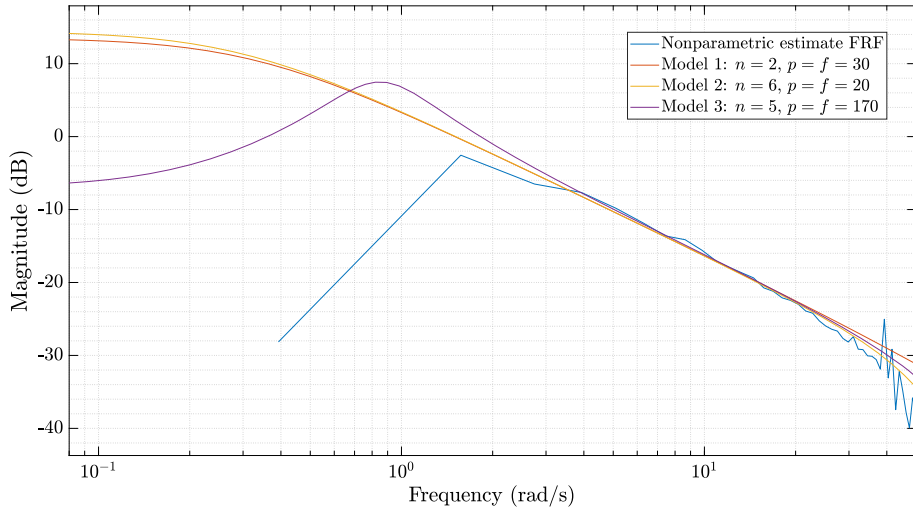


Figure 4.5: Frequency response of the non-parametric estimate, Model 1, Model 2 and Model 3.

an inaccurate response; consequently, VAF_{PRBS} is lower than VAF_{pilot} as seen previously. The low frequency contribution that causes a poor accuracy in the response of the estimated system is clearly visible in Figure 4.3b. To confirm this conclusion, a high-pass filter is applied to the measured and simulated outputs in order to remove the low-frequency contribution ($< 2\text{rad/s}$): the VAF_{PRBS} is now greater than 95%, confirming the poor description of the low frequency dynamics. These models are then discarded.

On the other side, Model 3 has a more accurate description of the model dynamics on a wider bandwidth; both VAF_{pilot} and VAF_{PRBS} have acceptable values. A further analysis is conducted in order to better characterize the low frequency response: other combination with high model order n and high horizon parameter p and f are tested, but in all the cases the change of slope is found at some radian per second of difference compared to the non parametric estimate. Then the values presented in Table 4.3 are used.

The identification data are analyzed with the coherence function which indicates whether the system has been satisfactorily excited across the entire frequency range of interest (calculated with MATLAB function *spaavf*, with averaging factor $N = 3$). It is represented in Figure 4.6a: according to [13], it is common practice to consider a system satisfactorily excited for values of the coherence function greater than 0.6. Considering the obtained results, in the case at hand the frequency validity range is $2 - 30 \text{ rad/s}$, that is the range in which all the three models have very high accuracy. Below 2 rad/s frequency, a poor excitation is obtained, making it impossible to correctly catch the characteristics of the system.

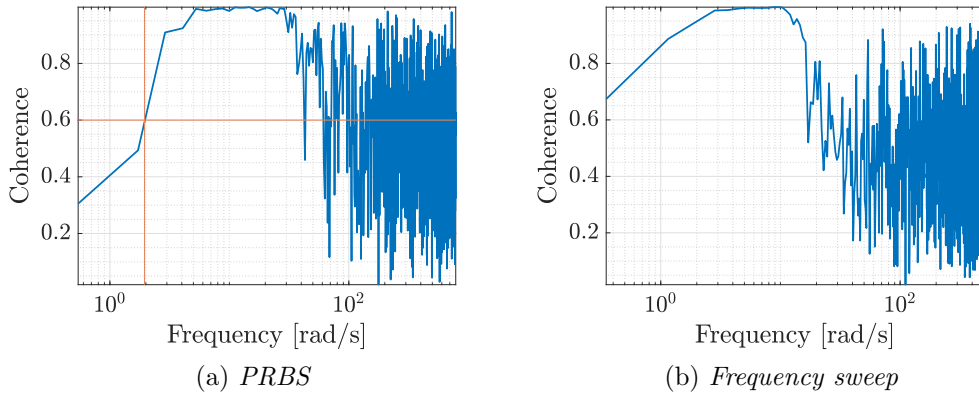


Figure 4.6: Coherence function of non-parametric frequency response function estimate.

For a better description of the low frequency response, an experiment that correctly excites this frequency range is needed. For this purpose other flight test experiments are carried out, this time using the frequency sweep excitation signals (Figure 4.7) described in Table 4.2. The obtained coherence function is shown in

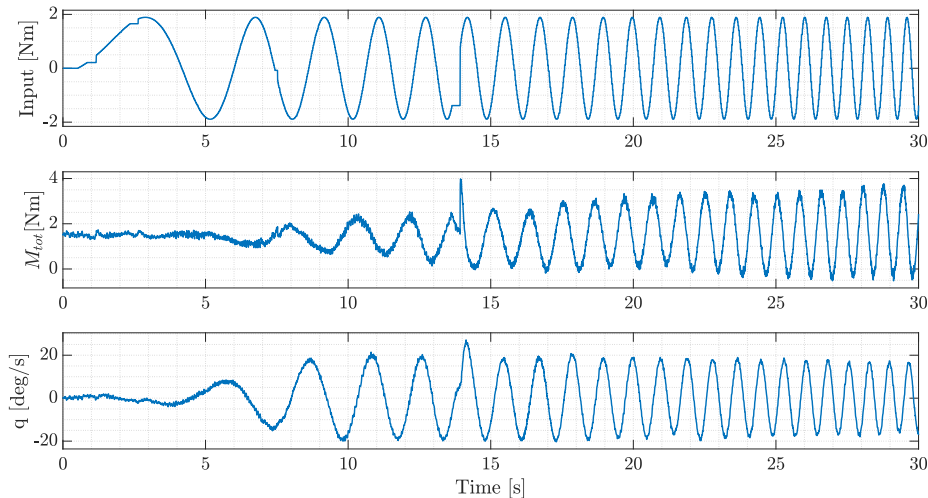


Figure 4.7: Excitation signal, total input command M_{tot} and pitch rate q during an identification test with frequency sweep excitation signal.

Figure 4.6b: the system has been excited at a lower frequency compared to the previous case. The same approach used for the PRBS signal is applied; in all the combination tested, the VAF values obtained (both of pilot maneuver data and PRBS validation data) are better compared to the PRBS case, in particular several configurations of model order and horizon parameters ensure $VAF_{pilot} > 90\%$

	Model order n	Horizon parameters p and f	VAF_{PRBS}	VAF_{pilot}
Model 4	8	50	90	83
Model 5	7	50	91	82
Model 6	6	50	92	79
Model 7	5	170	92	75

Table 4.4: Different longitudinal models obtained with frequency sweep experiment.

and $VAF_{PRBS} > 75$ (all with system order $n > 5$ and $p = f > 50$). The principal cases are reported in Table 4.4. All these models catch the change of slope (Figure 4.8); the one that is closer to the non-parametric estimate is Model 4 which is therefore chosen as definitive model. In Figure 4.9 the validation results obtained with Model 4 are shown.

The model order chosen is larger than the one of the physical structured model, in accordance with [13] conclusions. It is worth mentioning that in this case the choice is not supported by the singular values criterion.

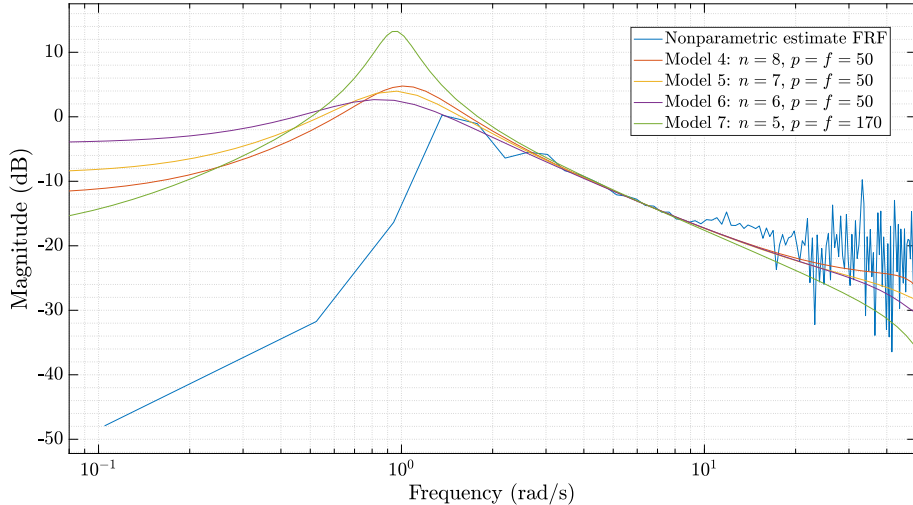


Figure 4.8: Frequency response of the non-parametric estimate, Model 4, Model 5, Model 6 and Model 7.

The low frequency excitation is conditioned by the experiment duration and the controller action. In [33], a long duration test is recommended in order to excite the system at low frequencies, but the duration of the experiment has to be selected taking also into account the batteries limits. Moreover, the closed-loop nature of the experiment affects the results: in Figure 4.7 it can be noted that the low frequency excitation is completely cancelled by the controller action: no

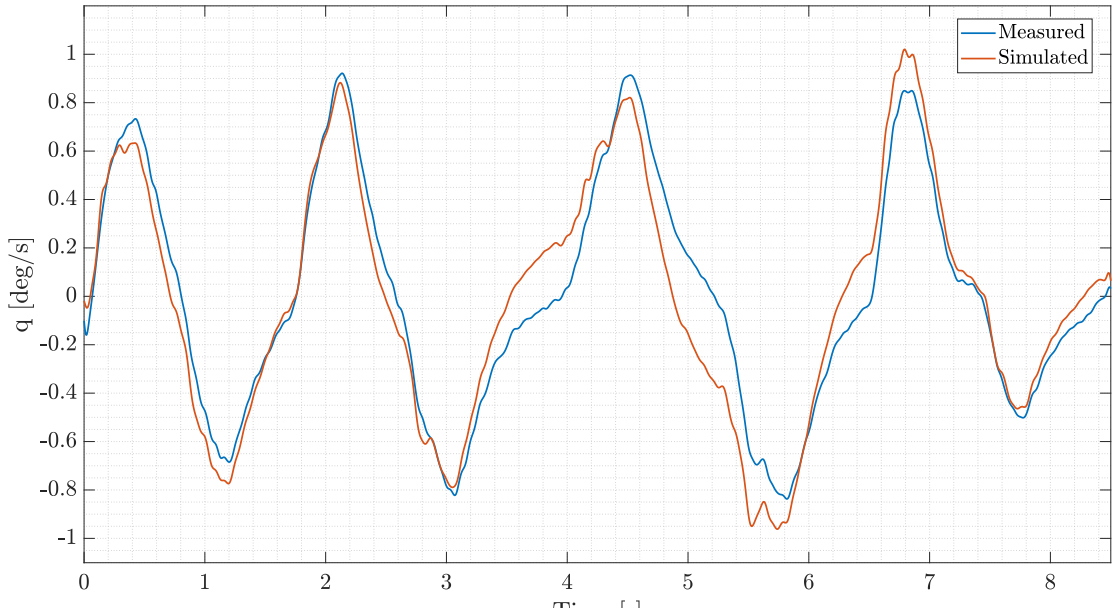
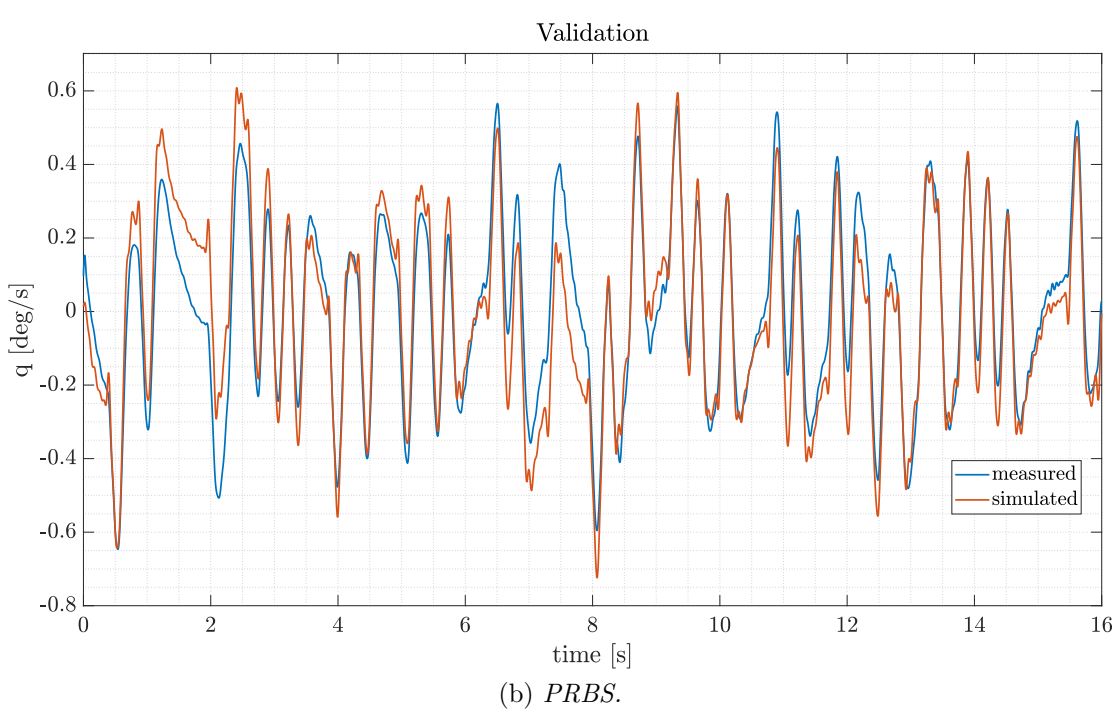
(a) *Manually piloted maneuvers.*(b) *PRBS.*

Figure 4.9: Time-domain validation for Model 4, longitudinal dynamics.

Model order n	Horizon parameters p and f	VAF_{PRBS}	VAF_{pilot}
3	90	81 %	84 %

Table 4.5: Lateral dynamics model and VAF results.

pitch rate is obtained.

A better description of the low frequency dynamics can be obtained with the $PBSID_{opt} - H_\infty$ method [13]. However, considering the VAF obtained and the comparison with the existing simulator that will be presented in Section 4.5, the identified dynamics identified with this method are considered satisfactory.

4.3.2 Lateral dynamics

The same approach is applied to the lateral dynamics identification. The best result is obtained with the frequency sweep input (Table 4.2) and summarized in Table 4.5. The validation of the identified model is shown in Figure 4.10 with a PRBS validation dataset. In this case the order of the model is $n = 3$, the same of the structured model and in agreement with the singular values criterion (Figure 4.11): a gap can be spotted at value 3 and 6; the VAF results obtained with $n = 3$ are better.

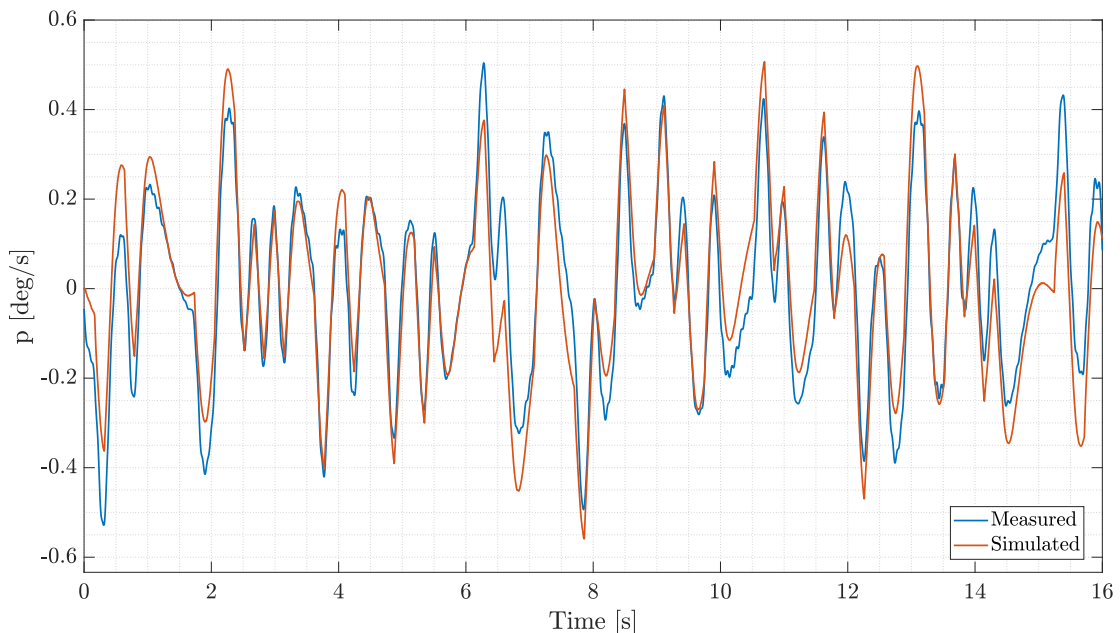


Figure 4.10: Time-domain validation for lateral dynamics on PRBS dataset.

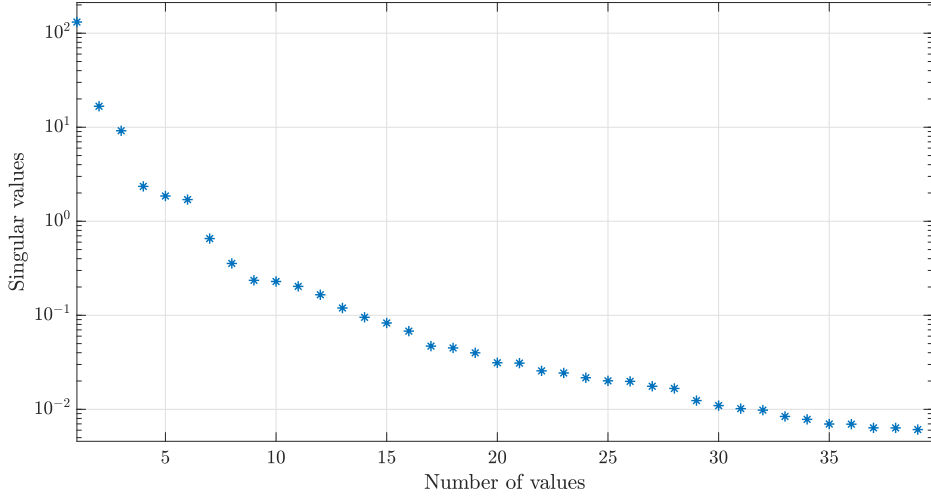


Figure 4.11: Singular values decomposition; a gap can be spotted between the first three values and the others.

Dynamics	Model order n	Horizon parameters p and f	VAF_{PRBS}
Directional	3	20	86 %
Vertical	4	30	65 %

Table 4.6: Directional and vertical dynamics models and VAF_{PRBS} results.

4.3.3 Directional and vertical dynamics

Directional and vertical dynamics are identified with the PRBS dataset; the parameters of the excitation signals are summarized in Table 4.1. The model parameters are selected to maximize the VAF_{PRBS} : several combinations of model order and horizon parameters are tested; the selected ones are summarized in Table 4.6, together with the obtained VAF_{PRBS} .

4.4 Updated simulator model

The identified dynamics is therefore used to build an updated *Simulink* model of the VTOL (Figure 4.12). The input motors' throttles th given by the multi-copter controller (propulsion command input) are converted into motors' angular rotations Ω with the relation described in Chapter 2:

$$\Omega = \frac{-b + \sqrt{(b^2 + 4 a t h)}}{(2 a)}, \quad (4.2)$$

then into force and moments, expressed in body frame, with the mixer matrix χ defined in Chapter 2. The moments L, M, N are converted into body rates p, q, r using the identified dynamics. The body force is converted into NED frame: the identified model is used only for the vertical component, the horizontal components are treated with the second law of motion. The weight contribution is added on the vertical axis. In Figure 4.13 the complete simulator is shown: the VTOL_multicopter_controller is added, that is the same controller used in the real VTOL, designed in Chapter 3.

4.5 Simulator validation

In this Section the old simulator ([2]), based on the six degrees of freedom dynamic equations (implemented with the *Simulink* built-in block) and the new one, based on the identified dynamics, are compared performing the same commands.

The 6-DOF simulator has been used for the initial tuning of the multicopter controller and, as shown in Chapter 3, it produced wrong results: the controller gains obtained through the simulator were too aggressive, leading to a loss of control and the crash of the aircraft.

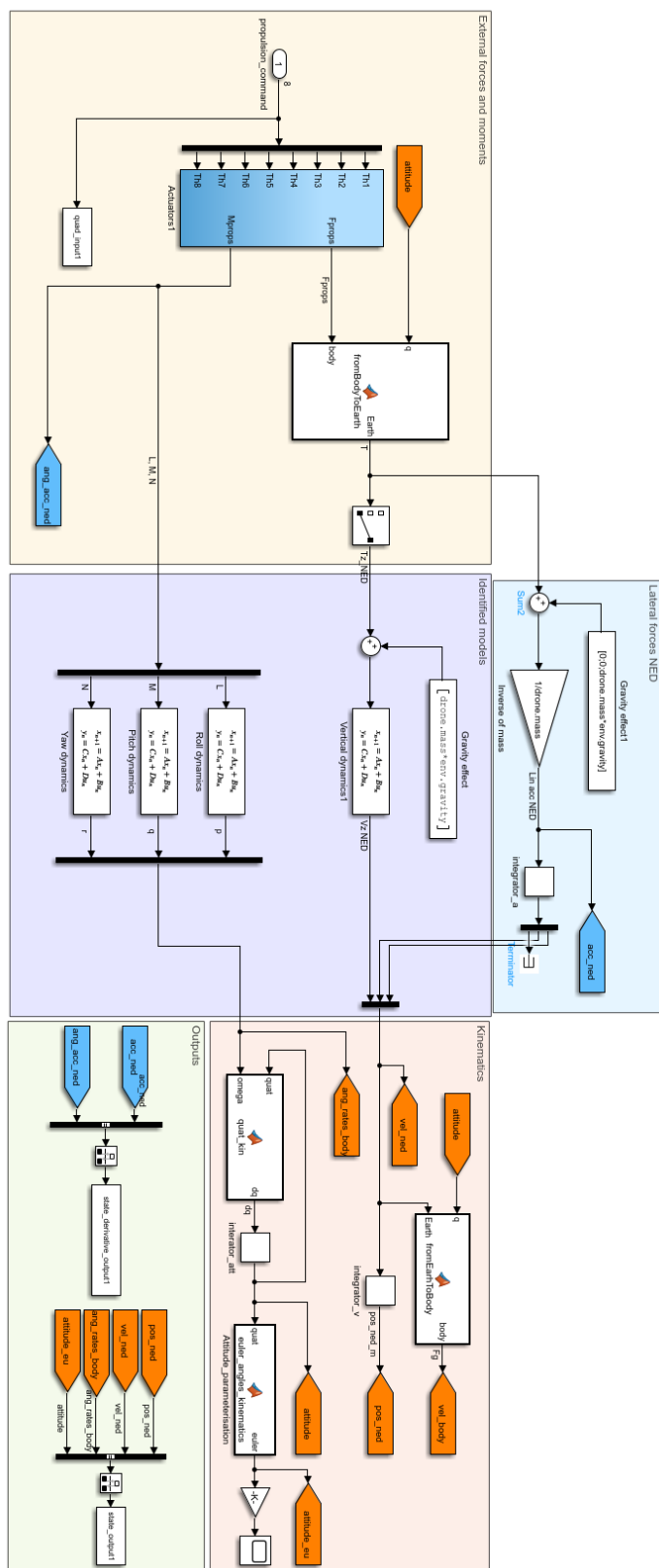
It is therefore mandatory to assess the behaviour of the simulator for future works. A real flight has been performed and the same command time history has been given in input to both simulators (6-DOF and identified dynamics) to check their accuracy.

The comparison is performed using the controller developed in Chapter 3 with the gains obtained through flight experiments; the only difference between the simulators is the dynamics inside the airframe block of Figure 4.12.

The time responses obtained giving the same setpoint (with *real_set_point* block, Figure 4.13) are compared and evaluated with the VAF index. The flight is performed in OFFBOARD MODE (Appendix A): the command given is a setpoint in inertial position and yaw angle ψ . Maneuvers in all the directions are performed; the flight test consists in:

- smooth take-off and climb to 1 m height from ground;
- vertical step command of 0.5 m;
- vertical step of -0.5 m;
- lateral step of -1.5 m;
- lateral step of 1.5 m;
- smooth yaw angle ψ command, from 0° to -90° ;
- longitudinal step of -1.5 m;

Figure 4.12: *Simulink* VTOL model with identified dynamics.



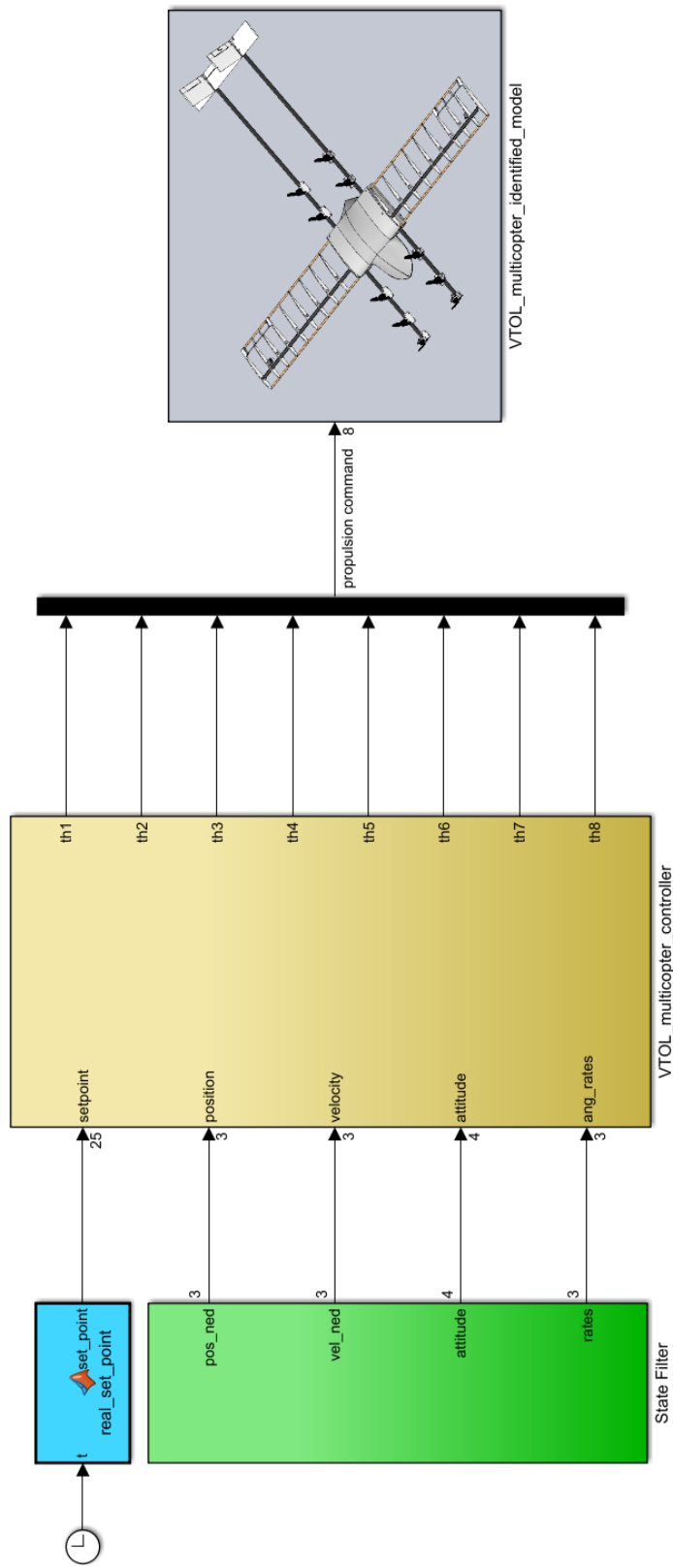


Figure 4.13: *Simulink* VTOL simulator with identified dynamics.

- longitudinal step of 1.5 m;
- landing.

The results obtained are presented in the following: the position in inertial frame is shown in Figure 4.14 (the drone is initially oriented in the north direction). Figure 4.15 shows the velocities in the inertial frame, Figure 4.16 the attitude angles and Figure 4.17 the angular rates. The VAF values, calculated between true measurements and simulated ones, are summarized in Table 4.7. As expected, the performances of the new simulator are excellent: all the measurements faithfully follow the real trend. Unexpectedly, given the tuning problems, also the old simulator's performances are great, comparable to that of the new one: in most cases the results match.

Some considerations can be made looking at the position measurements: the initial and final offset in the vertical position between real flight and simulations (Figure 4.14) is due to the fact that, in reality, the vehicle takes off from a matress 10 cm thick. On the north axis, no maneuver is performed; the oscillations visible in the flight data are caused by turbulence produced by the rotors: the eight motors generate a huge airflow that, being indoor and not having space to disperse, generates vortices that are picked up by the wings, causing oscillations. This indicates that also the other measurements are affected by this effect so, comparing the simulations with a flight in calm air, the match would be better. For this reason the VAF value calculated on the north axis' measurements is not considered. In order to consider the turbulence effect, the VAF of attitude and rates measurements are calculated only during maneuvers.

The good results obtained with the new simulator are an additional validation of the identified model and of the methodology used.

Starting from the comparison of the two simulators with real flight experiments, some considerations can be made on the 6-DOF one:

- the simulator accurately reproduces the mission, with performance comparable to the new simulator;
- on the other side: the controller parameters obtained with the tuning on this model are incorrect for the real model.

This opposite behaviour can be explained by the fact that the maneuvers of the considered flight test do not excite the structural dynamics of the aircraft; in the case of the controller tuning, instead, the structural dynamics can not be neglected then, the gains obtained in simulation produced bad results. In small multicopters the structural dynamics contribution is negligible (see as example [10], [34], [31]) and during the design phase it has not been taken into account. However, in the case at hand, the size and the configuration are different: the structural dynamics has an important role, mainly due to the fuselage. Low structural stiffness causes non-negligible bending and torsion that cannot be neglected during the design of the controller.

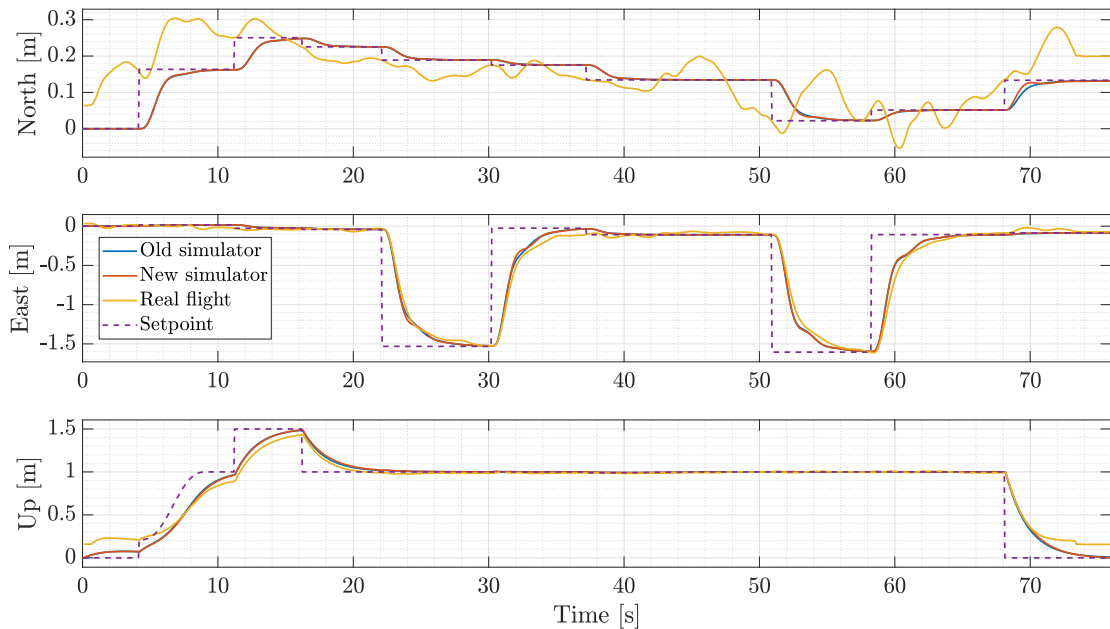


Figure 4.14: Position measurements.

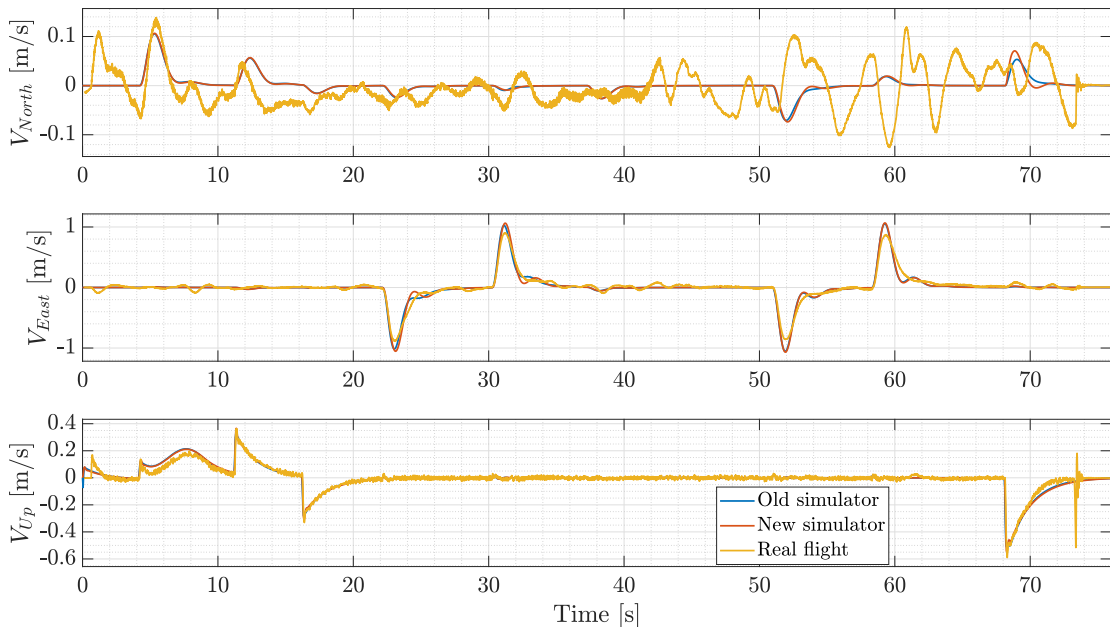


Figure 4.15: Velocity measurements.

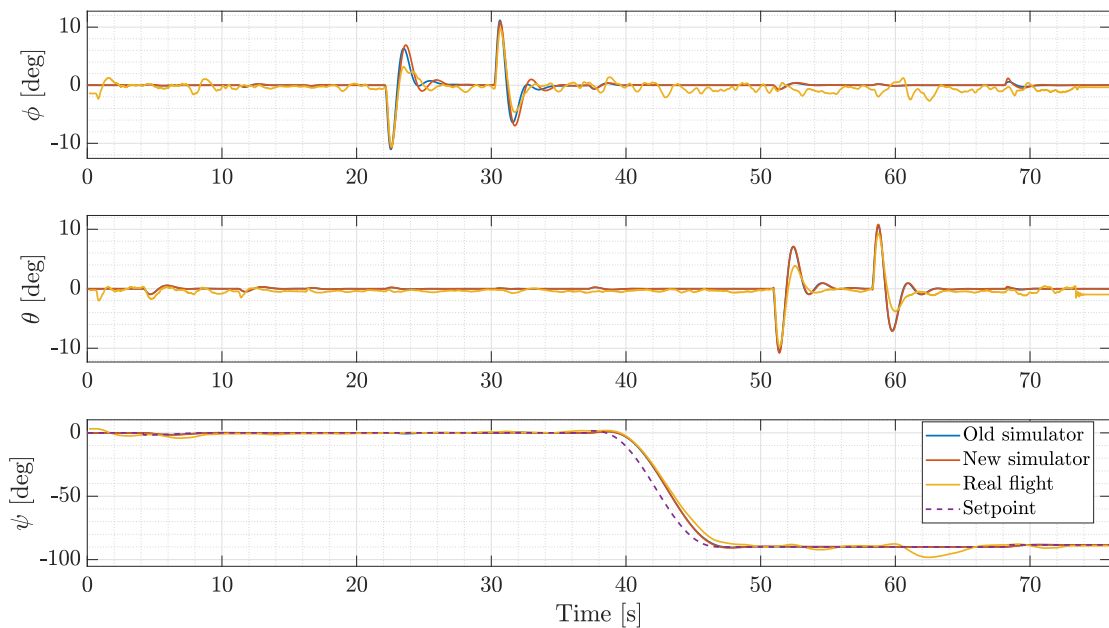


Figure 4.16: Attitude measurements.

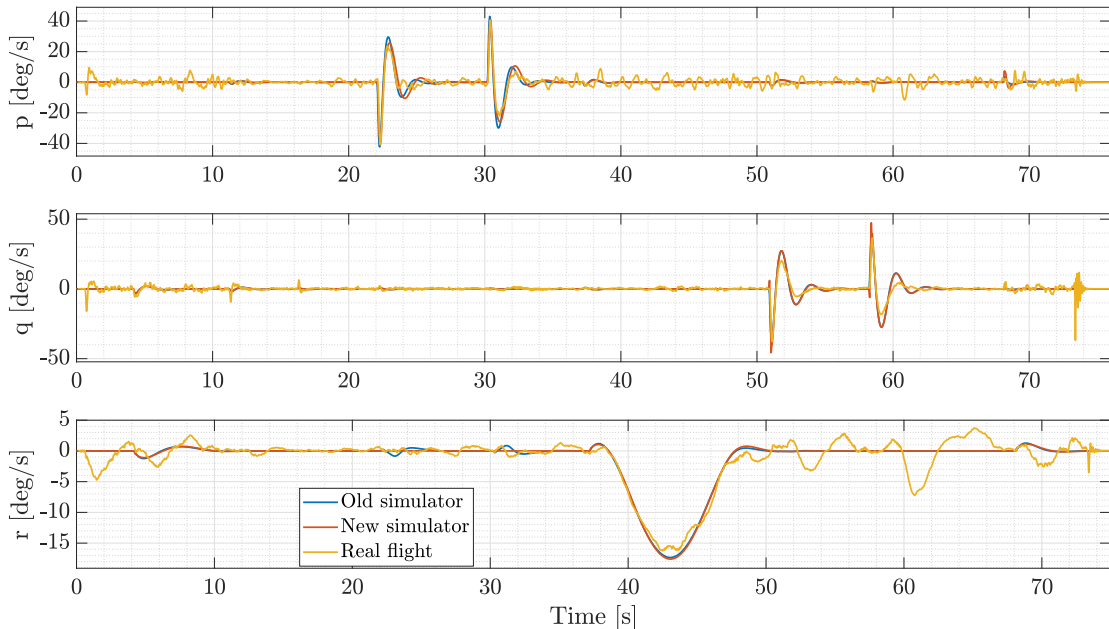


Figure 4.17: Angular rates measurements.

	VAF old simulator	VAF new simulator
North	32.1 %	33.5 %
East	99.1 %	99.1 %
Up	98.1 %	98.2 %
V_{North}	0 %	0 %
V_{East}	94.4 %	93.9 %
V_{Up}	94.9 %	95.8 %
Roll angle θ	76.5 %	77.5 %
Pitch angle ϕ	81.5 %	83.2 %
Yaw angle ψ	99.7 %	99.7 %
Roll rate p	78.0 %	85.2 %
Pitch rate q	78.5 %	78.3 %
Yaw rate r	96.1 %	95.4 %

Table 4.7: VAF values of old and new simulator compared to a real flight.

Chapter 5

Fixed-wing controller

In this chapter, the fixed-wing control system is presented. The chapter is organised into two main sections.

The first one is attitude control: a general PID cascade loop is used, with turn coordination constraint and controller action scaled with velocity.

Then the simultaneous control of altitude and airspeed is presented. This task is carried out by a Total Energy Control System (TECS): two algorithms are implemented and evaluated.

5.1 Fixed-wing attitude controller

In this section the attitude control system of the VTOL in fixed-wing phase is presented in detail. The main structure is derived from [24]. Longitudinal and lateral dynamics are assumed to be uncoupled. The variables that have to be controlled are roll angle ϕ , pitch angle θ and yaw rate $\dot{\psi}$.

5.1.1 Roll and pitch control

The controller structure is a PID cascade loop (Figure 5.1). Roll and pitch controllers have the same structure: the outer loop computes the error between the attitude setpoint ϕ_{sp}, θ_{sp} and the estimated attitude ϕ, θ respectively. That, multiplied by proportional gain P , generates an Euler angles derivatives setpoint $\dot{\phi}_{sp}, \dot{\theta}_{sp}$. This is converted into body rate setpoint p_{sp}, q_{sp} with the matrix E (defined in the first Chapter, Section 1.2). The inner loop then computes the error in rates and uses proportional and integral controller (PI) to generate the desired deflection of the control surfaces δ_a, δ_e (aileron and elevator respectively).

The yaw controller, instead, generates its yaw rate setpoint using the turn coordination constraint in order to minimize the lateral acceleration.

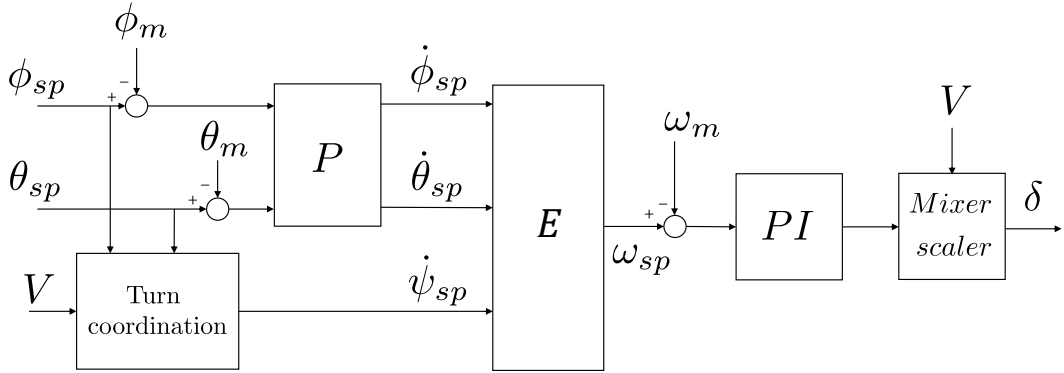


Figure 5.1: Fixed-wing attitude control architecture: ω is the body rates vector, δ the control surfaces deflections vector ($\delta = [\delta_a, \delta_e, \delta_r]$) and V the airspeed.

5.1.2 Yaw rate control: turn coordination

Analysing the turn maneuver in Figure 5.2, the horizontal resultant equilibrium is:

$$F_{lift} \sin \phi = m\dot{\psi}^2 R = mV\dot{\psi}, \quad (5.1)$$

where F_{lift} is the lift, R the turn radius, V the aircraft speed and m the aircraft mass. The vertical component must be equal to the gravity force:

$$F_{lift} \cos \phi = mg; \quad (5.2)$$

dividing equation (5.1) by equation (5.2) yields:

$$\dot{\psi} = \frac{g}{V} \tan \phi. \quad (5.3)$$

Considering a general case with pitch angle θ :

$$\dot{\psi} = \frac{g}{V} \tan \phi \cos \theta, \quad (5.4)$$

that is the yaw rate for which the coordinated turn can be achieved.

A scaling factor K_{scaler} is introduced to moderate the control action according to the airspeed V : the effectiveness of the moving surfaces depends on airspeed (their action is based on the dynamic pressure): at high speed they are moved

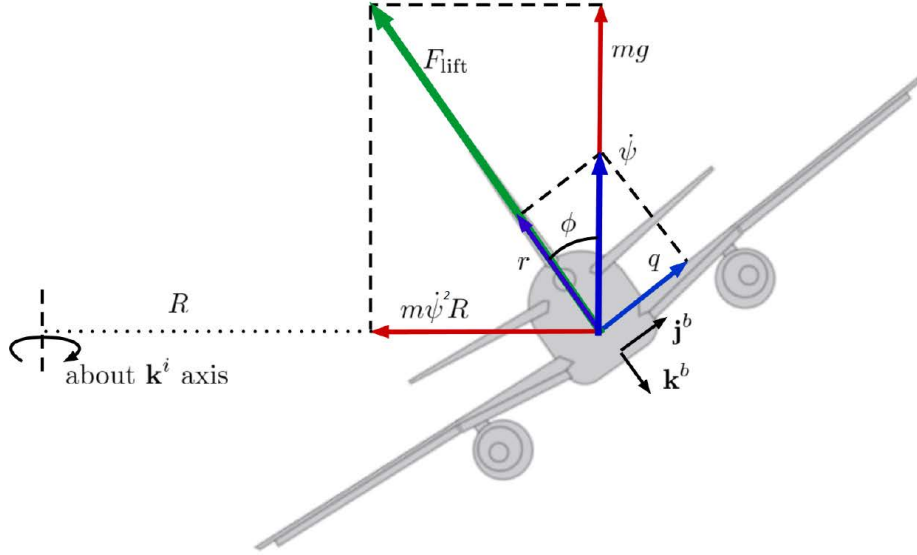


Figure 5.2: Forces during a turn, from [35].

Rudder	Elevator	Aileron
50° Left	60° Down	35° Down
55° Right	-50° Up	-45° Up

Table 5.1: Maximum measured surfaces deflections.

less and at low speed are moved more to provide the same control action. The scaling equation is:

$$K_{scaler}(V) = \frac{V_a}{V}, \quad (5.5)$$

where V_a is the cruise speed (15 m/s) at which the controller is tuned. Saturation limits on the deflection of the control surfaces are introduced according to the maximum measured surfaces deflections, summarized in Table 5.1.

5.1.3 Simulations and controller evaluation

The fixed-wing attitude controller is implemented in *Simulink* according to the logic presented in this Section (Figure 5.3). With the fixed-wing *Simulink* model implemented in [2] it is therefore possible to simulate the fixed-wing flight. The controller has been tuned manually in simulation, according to the response to step and doublet inputs. Several maneuvers are tested: the aircraft responds correctly and without oscillations to the attitude commands. The results of a complete flight mission, composed by coordinated turns, climb and descent maneuvers, are shown in Figure 6.12. In addition, the unstable spiral mode that appeared in the

simulation performed in [2] is suppressed, allowing to complete the mission.

The *Simulink* controller is then successfully converted into C++ code and imported in the PX-4 firmware with the SLXtoPX4 application ([26]). As in the multicopter case, different flight modes have been implemented (Appendix A). It is therefore possible to conduct some practical ground tests for a first check of the operation of the real aircraft (the tests are conducted in ATTITUDE MODE):

- the control surfaces respond correctly to the given radio commands;
- the control surfaces move in the right direction in order to maintain the given null attitude setpoint while rotating manually the aircraft around its axis;
- there are no interactions between the controller and the vibration induced by the motors: the vehicle has been anchored to the ground and all the motors have been turned on, with no effects on the control surfaces;
- the pitot tube airspeed sensor is tested using a fan to generate an air flow: the obtained measure is very noisy, then a low pass filter to preprocess the data is introduced. The result is shown in Figure 5.4: the fan is located at 0.5 m from the sensor and activated at two different speeds.

All the results are positive; the controller has been implemented and installed correctly, the ground test is passed. At a later time it will be tested in flight.

5.2 Total energy control system (TECS)

Simultaneous control of true airspeed and height is not a trivial task. The aircraft's responses in altitude and speed are coupled: an increase in thrust will generally increase both the airspeed and the altitude, while a nose-up elevator command will result in increasing altitude and decreasing speed.

Conventional SISO controllers do not account for this and just assign one actuator to each control variable, typically using elevator for altitude control and thrust for speed control ([36]).

This leads to a lack of capability to provide integral flight envelope protection and to prevent control coupling problems ([37]).

TECS offers a solution by representing the problem in terms of energies rather than in terms of the original setpoints. The control problem is therefore decoupled by transforming the initial setpoints into energy quantities which can be controlled independently. Thrust is used to regulate the specific total energy of the vehicle and pitch to maintain a specific balance between potential (height) and kinetic (speed) energy. This solution was designed and successfully tested by NASA on a B737 airplane in 1987 ([38]).

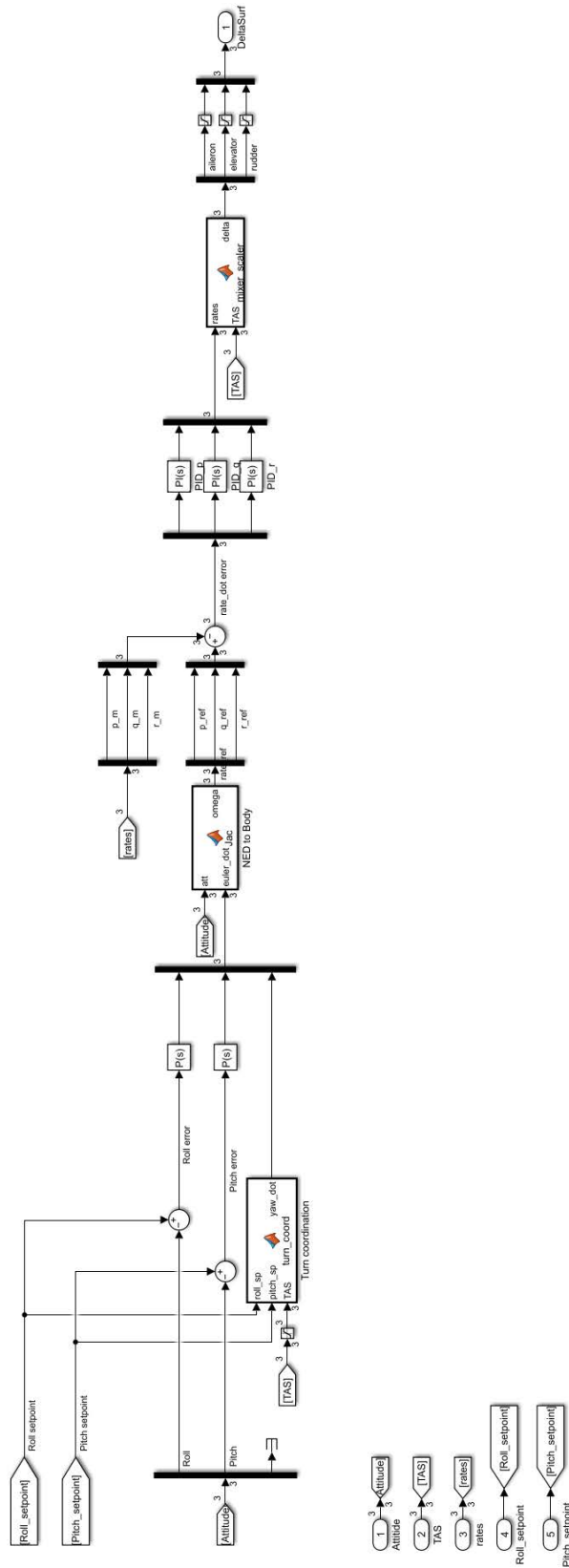


Figure 5.3: *Simulink* fixed-wing attitude controller.

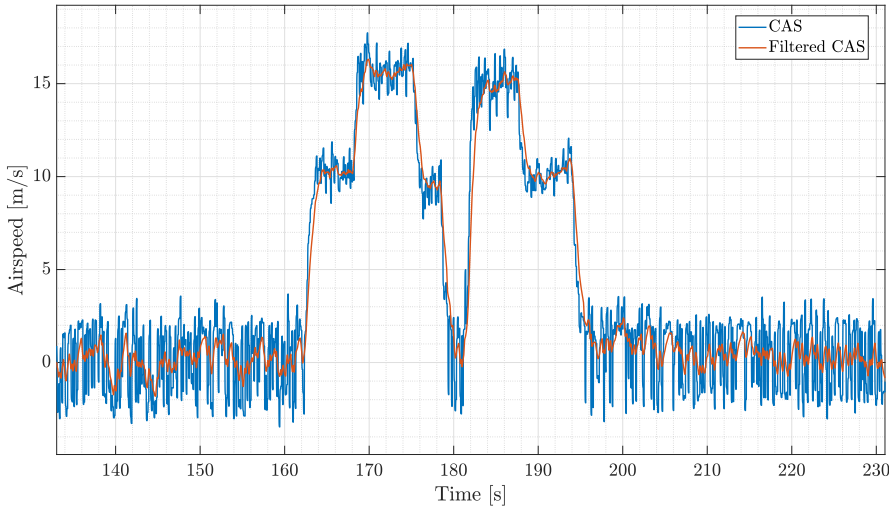


Figure 5.4: Pitot tube airspeed measurement during on-ground testing.

5.2.1 Controller algorithm

The following analysis is derived from [39].

The total energy of an aircraft is expressed as the sum of kinetic and potential energy

$$E_T = \frac{1}{2}mV^2 + mgH; \quad (5.6)$$

taking the derivative of E_T with respect to time leads to the total energy rate (assuming constant mass):

$$\dot{E}_T = mV\dot{V} + mg\dot{H}. \quad (5.7)$$

Dividing equation (5.7) by mgV the specific energy rate is obtain:

$$\dot{E} = \frac{\dot{V}}{g} + \frac{\dot{H}}{V} = \frac{\dot{V}}{g} + \sin \gamma, \quad (5.8)$$

where γ is the flight path angle. Assuming small γ :

$$\dot{E} \approx \frac{\dot{V}}{g} + \gamma. \quad (5.9)$$

From the point mass airplane force equations it follows that, for small flight path angles:

$$T - D = mg\left(\frac{\dot{V}}{g} + \sin \gamma\right) \approx mg\left(\frac{\dot{V}}{g} + \gamma\right), \quad (5.10)$$

where T and D are the thrust and drag. In level flight, initial thrust T is trimmed against the drag D and a change in thrust command results thus in:

$$\Delta T_c = mg \left(\frac{\dot{V}_e}{g} + \gamma_e \right), \quad (5.11)$$

where the subscript e refers to the error in that variable.

From equations (5.9) and (5.11) it follows that:

$$\Delta T_c \propto \dot{E}_e, \quad (5.12)$$

where \dot{E}_e is the specific energy rate error, defined as:

$$\dot{E}_e = \gamma_e + \frac{\dot{V}_e}{g}. \quad (5.13)$$

Then, a change in thrust will proportionally alter the specific energy rate of the airplane, increasing the sum of the airplane flight path angle and the acceleration along the flight path.

Elevator control, on the other hand, is with good approximation energy conservative: thus it is used to exchange potential energy for kinetic energy and and *vice versa*. To this end, a specific energy balance rate is defined as:

$$\dot{L} = \gamma - \frac{\dot{V}}{g}. \quad (5.14)$$

Summing up, thrust setpoint is used for total energy control and elevator is considered for energy distribution control.

From this, we can formulate a simple control law, using proportional and integral control feedback:

$$\frac{T_c}{mg} = \frac{K_{TI}}{s} \dot{E}_e - K_{TP} \dot{E}; \quad (5.15)$$

$$\theta_c = \frac{K_{EI}}{s} \dot{L}_e - K_{EP} \dot{L}; \quad (5.16)$$

where

$$\dot{E}_e = (\gamma_{sp} - \gamma) + \left(\frac{\dot{V}_{sp}}{g} - \frac{\dot{V}}{g} \right); \quad (5.17)$$

$$\dot{E} = \gamma + \frac{\dot{V}}{g}; \quad (5.18)$$

$$\dot{L}_e = (\gamma_{sp} - \gamma) - \left(\frac{\dot{V}_{sp}}{g} + \frac{\dot{V}}{g} \right); \quad (5.19)$$

$$\dot{L} = \gamma - \frac{\dot{V}}{g}. \quad (5.20)$$

The control outputs are the normalized thrust $\frac{T_c}{mg}$ and the pitch angle θ_c . Subscript sp indicates the setpoint and subscript e the error in that variable. For the

proportional terms only \dot{E} and \dot{L} feedbacks are used instead of the error signals, to avoid the creation of unwanted zeros in the system transfer functions. This smoothens the transient response and eliminates undesirable response overshoots in the command response. The main structure of the algorithm is shown in Figure 5.5.

The gains K_{TI} , K_{TP} and K_{EI} , K_{EP} are designed to yield identical dynamics for energy rate error \dot{E}_e and energy distribution rate error \dot{L}_e , for either a flight path angle command or a longitudinal acceleration command. The MIMO control law allows precise thrust and elevator control coordination to achieve decoupled command responses. As a result, a flight path angle command will not cause a significant speed deviation and vice versa.

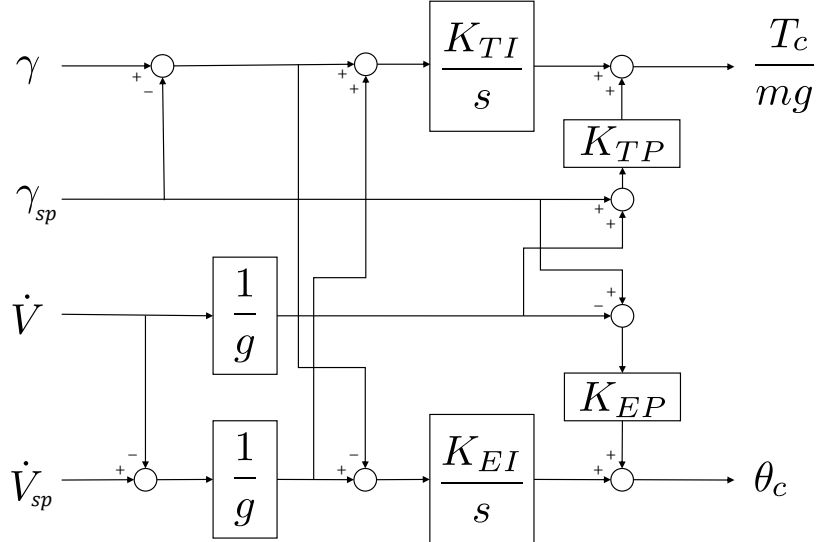


Figure 5.5: TECS algorithm structure.

In anticipation of the transition phase, where large variations occur in short time and a reactive controller action is mandatory, a slightly different version of TECS controller is implemented (identified as $TECS_m$): both the proportional and integral parts of the controller work on the error signal. It is design according to [40], in which the overshoot is used to get rapid response and limited to an acceptable range by adjusting the tuning parameters.

Both structures are implemented, tested in simulation and evaluated.

The *Simulink* implementation of the TECS (Figure 5.6) and $TECS_m$ (Figure 5.7) algorithms additionally includes anti-windup protection on the thrust command.

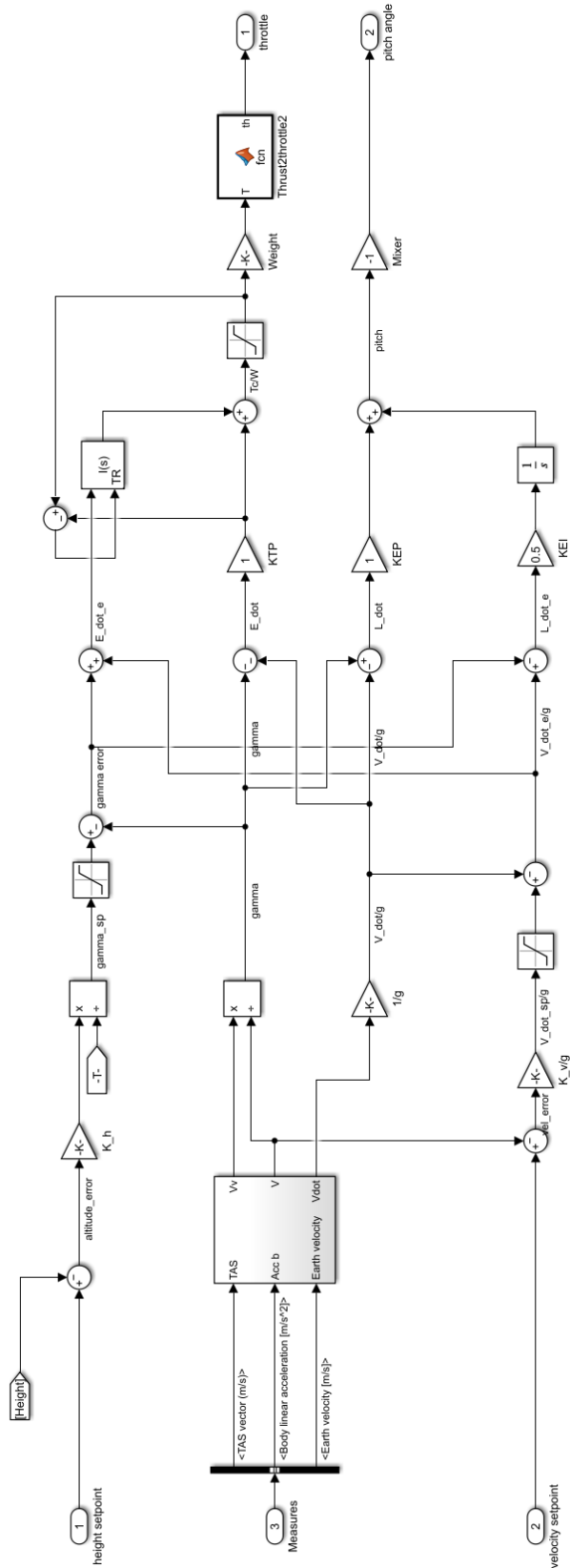


Figure 5.6: *Simulink* TECS model: core algorithm and outer loop.

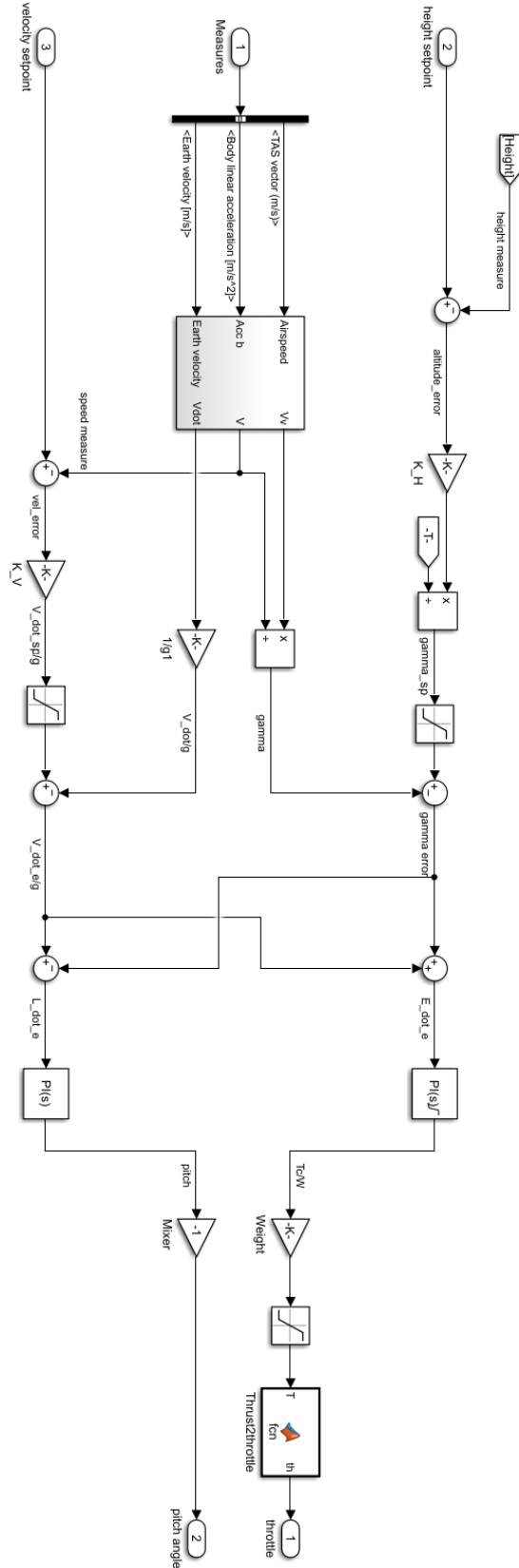


Figure 5.7: *Simulink TEC_{S_m}* model: core algorithm and outer loop.

5.2.2 Controller input and output

Since, from a control point of view, the interest is in altitude H_{sp} and speed V_{sp} , the flight path angle γ_{sp} and the normalised longitudinal acceleration $\frac{\dot{V}_{sp}}{g}$ are computed externally, as can be seen in Figure 5.6 and Figure 5.7. The computation is performed using a proportional controller on height and velocity error:

$$\dot{V}_{sp} = K_v (V_{sp} - V), \quad (5.21)$$

$$\dot{H}_{sp} = K_H (H_{sp} - H), \quad (5.22)$$

$$\gamma_{sp} = \frac{\dot{H}_{sp}}{V}. \quad (5.23)$$

Speed and altitude errors need to be weighted equally in order to achieve decoupled control and efficient energy management during simultaneous flight path and speed maneuvers. Thus the gains K_v and K_H should be selected equal ([39]). These commands, \dot{V}_{sp} and γ_{sp} , must be limited according to the aircraft performance in order to stay within a safe flight envelope.

For the input measurement \dot{V} it is suggested ([35]), in order to avoid to compute the derivative of noisy airspeed sensor measurements, to take the acceleration measurement on the \mathbf{b}_1 axis and subtract the contribution given by gravity:

$$\dot{V} = a_x - g \sin \theta. \quad (5.24)$$

The outputs of the TECS controller consists of a normalized thrust $\frac{T_c}{mg}$ and a pitch angle θ_c . The latter is given in input into the attitude controller (Section 5.1). Thus, the performance of TECS is directly affected by the performance of the pitch control loop.

The normalized thrust, after the multiplication with the aircraft weight, is converted into throttle command δ_t according to the following relations:

$$\Omega = \sqrt{\frac{T_c}{K_T n_{motors}}}; \quad (5.25)$$

$$\delta_t = \frac{(\Omega - q_{fwd})}{m_{fwd}}; \quad (5.26)$$

where Ω is the angular speed of the motors. The coefficients K_T , q_{fwd} and m_{fwd} have been computed in [2].

Gain	Thrust	Pitch
Integral	$K_{TI} = 1$	$K_{EI} = 1$
Proportional	$K_{TP} = 0.5$	$K_{EP} = 0.5$

Table 5.2: TECS gains.

Gain	Thrust	Pitch
Integral	$K_{TI} = 1.5$	$K_{EI} = 1.5$
Proportional	$K_{TP} = 2$	$K_{EP} = 2$

Table 5.3: $TECS_m$ gains.

5.2.3 Controller tuning

For both controllers the parameters are manually tuned in simulation in order to produce suitable performance responses to command signals.

The first step is the tuning of the core algorithm, by giving step demand in γ_{sp} and \dot{V}_{sp} . Then the outer loop is closed and tuned as well. The main constraint is that the gain must yield identical dynamics for energy rate error \dot{E}_e and energy distribution rate error \dot{L}_e in order to ensure coordinated response: this translates into $K_{TI} = K_{TP}$, $K_{EI} = K_{EP}$ and $K_v = K_H$ ([39]). The initial values used are the one indicated in [39] for the TECS algorithm and [40] for the $TECS_m$ algorithm. The final values are summed up in Table 5.2, Table 5.3 and Table 5.4.

The discovered parameters can be finely tuned in flight if necessary: the tuning of control parameters for small UAV is often done manually in flight ([36]).

5.2.4 Controller evaluation

Both TECS controllers are tested in simulation: step changes in airspeed and altitude are tested, as well as combined maneuvers ([36]). The goal is to assess the performance in terms of tracking capabilities and decoupling. All simulations are performed starting from a trim condition at cruise speed.

Specifically:

- airspeed increase (Figure 5.8): an altitude change of 0.30 m for the TECS controller and 0.09 m for the $TECS_m$ controller is obtained for an airspeed

	Velocity	Height
Gain	$K_v = 1.5$	$K_H = 1.5$

Table 5.4: Outer loop gains.

step input of 2 m/s. Both controllers have a settling time around 30 s. TECS has a small overshoot (0.01 m/s). In the initial part $TECS_m$ has a faster response.

- Airspeed decrease (Figure 5.9): an altitude change of 0.38 m for the TECS controller and 0.11 m for the $TECS_m$ controller is obtained for an airspeed step input of -2 m/s. Both controllers have a settling time around 30 s. No overshoot is present. In the initial part $TECS_m$ has a faster response.
- Climb (Figure 5.10): an altitude step input of 10 m causes an airspeed change of 0.03 m/s for the TECS controller and 0.15 m/s for the $TECS_m$ controller. Both controllers have a settling time around 30 s. TECS response presents overshoot (0.70 m). In the initial part $TECS_m$ has a faster response.
- Descent (Figure 5.11): an altitude step demand of -10 m causes an airspeed change of 0.01 m/s for the TECS controller and 0.03 m/s for the $TECS_m$ controller. Both controllers have a settling time around 30 s. TECS response presents overshoot (0.44 m). In the initial part $TECS_m$ has a faster response.
- Climb and airspeed decrease (Figure 5.12): for an airspeed step demand of -1 m/s and an altitude step of 5 m is obtained a settling time for the two quantities for both controllers around 30 s. Small overshoot is present in altitude (0.20 m) for the TECS controller. In the initial part $TECS_m$ have a faster response.
- Descent and airspeed increase (Figure 5.13): for an airspeed step demand of +1 m/s and an altitude step of -5 m is obtained a settling time for the two quantities for both controllers around 30 s. Small overshoot is present in altitude (0.24 m) for the TECS controller. In the initial $TECS_m$ has a faster response.

Considering the reference values provided in [39], both algorithms provide good performance in term of decoupling between velocity control and altitude control. This performance is deeply affected by the dynamics of engine and elevator actuation: a different time response can cause larger coupling effect. In these simulations the dynamics of the motor (identified in Chapter 2) is used and the elevator servo mechanism is considered instantaneous.

Both controllers track successfully the altitude and airspeed setpoint: the settling time is in line with the result obtained with this type of architecture, as presented in [39] and [36]. There are no oscillations, only a very small overshoot in the case of TECS. The $TECS_m$ controller is more reactive in the initial part of the response: this can be seen also in the throttle and elevator deflection commands.

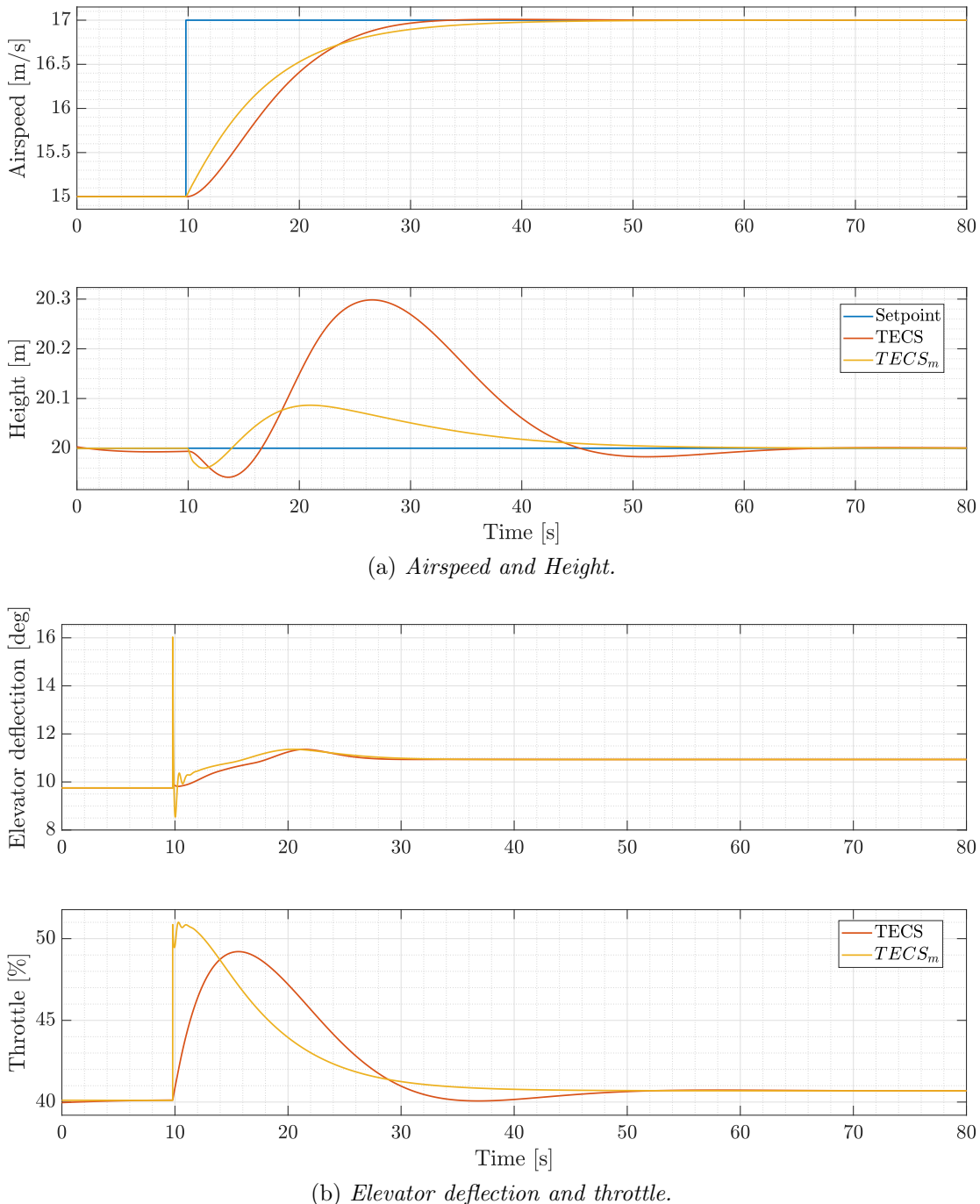


Figure 5.8: Simulation of a 2 m/s speed increase: physical quantities.

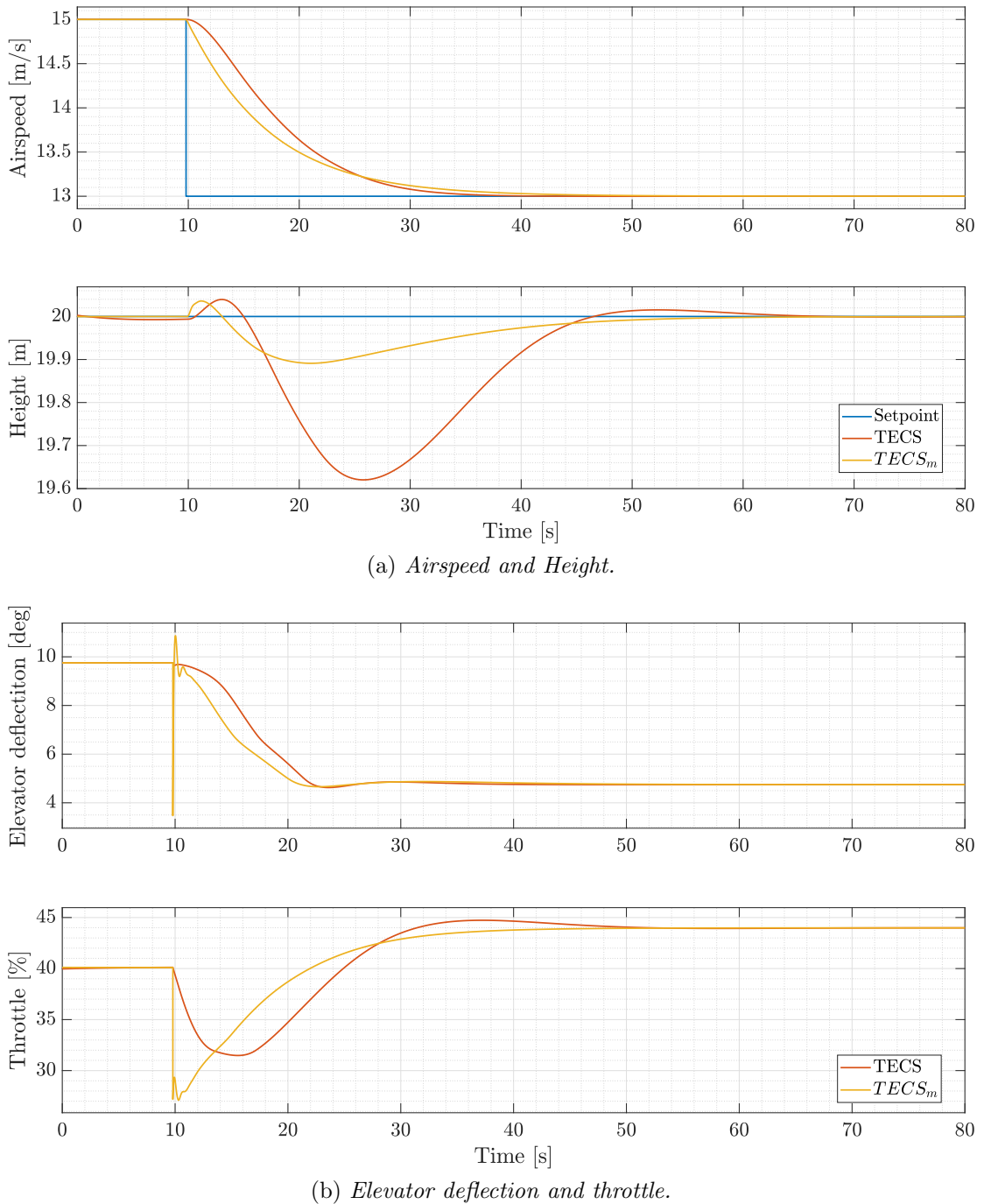


Figure 5.9: Simulation of a 2 m/s speed decrease: physical quantities.

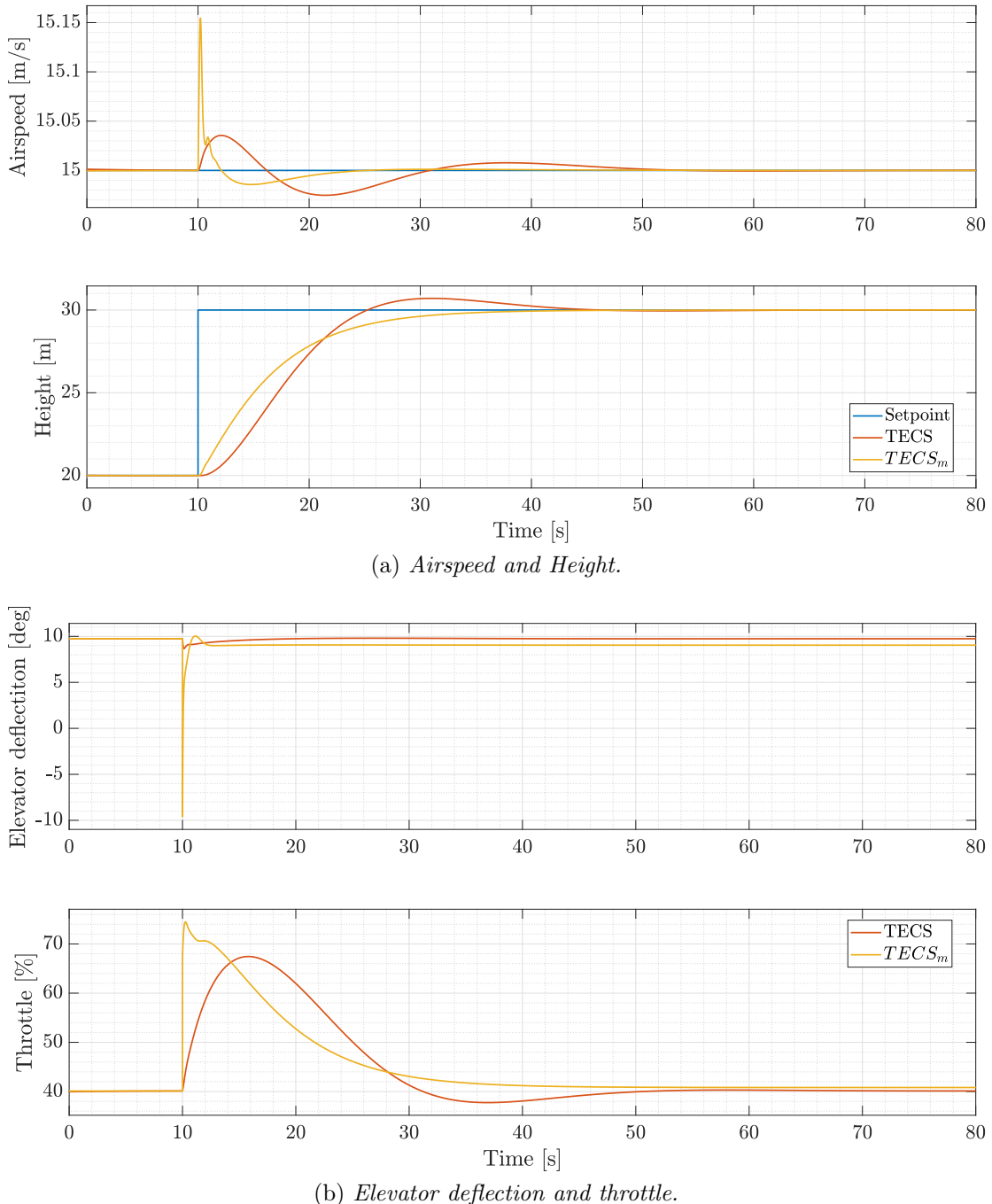


Figure 5.10: Simulation of a 10 m climb manoeuvre: physical quantities.

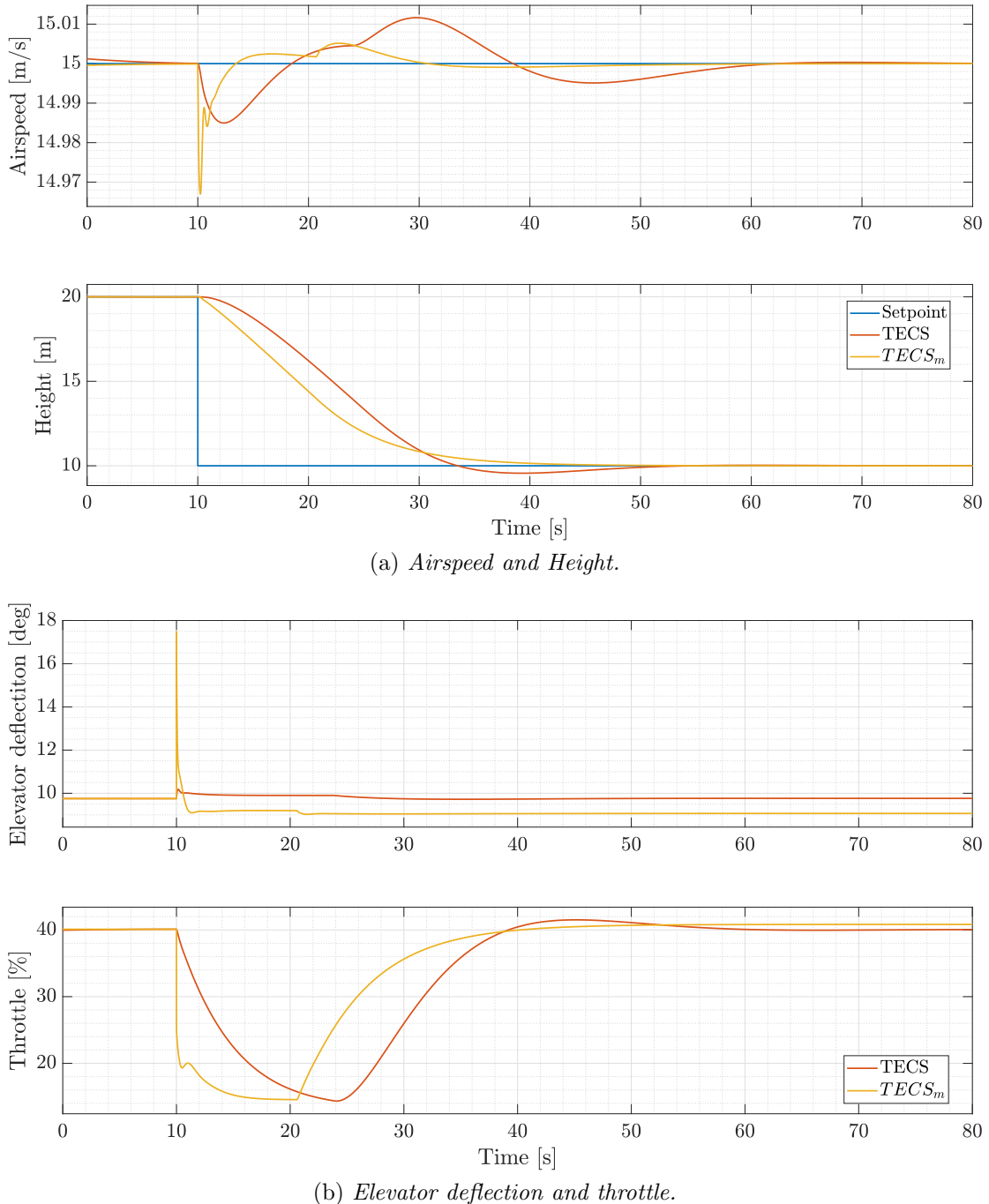


Figure 5.11: Simulation of a 10 m descent manoeuvre: physical quantities.

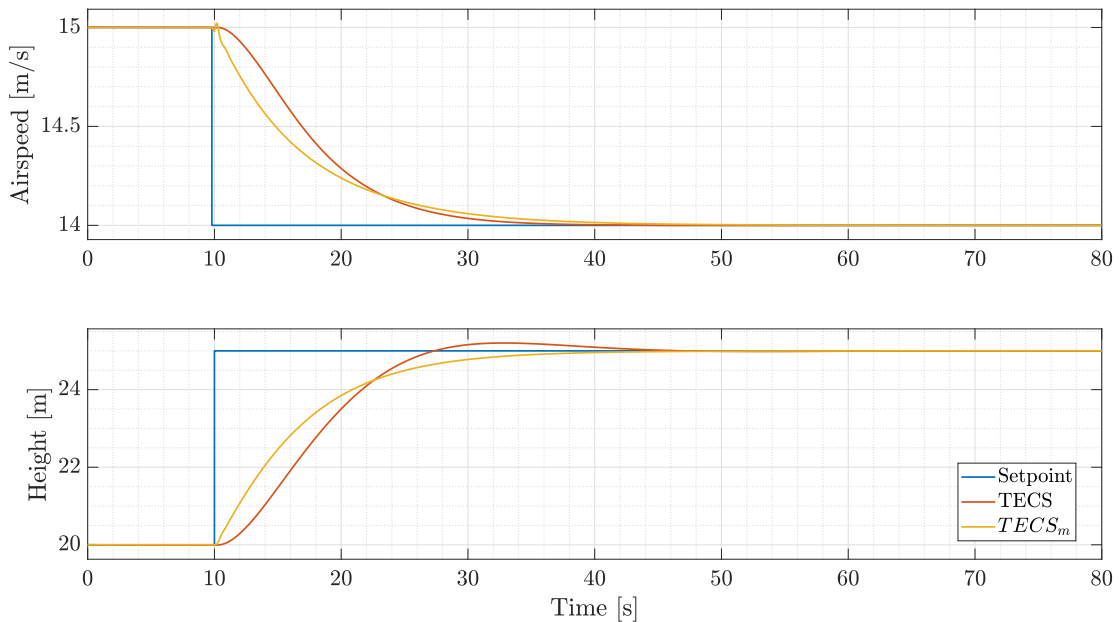


Figure 5.12: Simulation of a combined manoeuvre: 5 m climb and 1 m/s speed decrease.

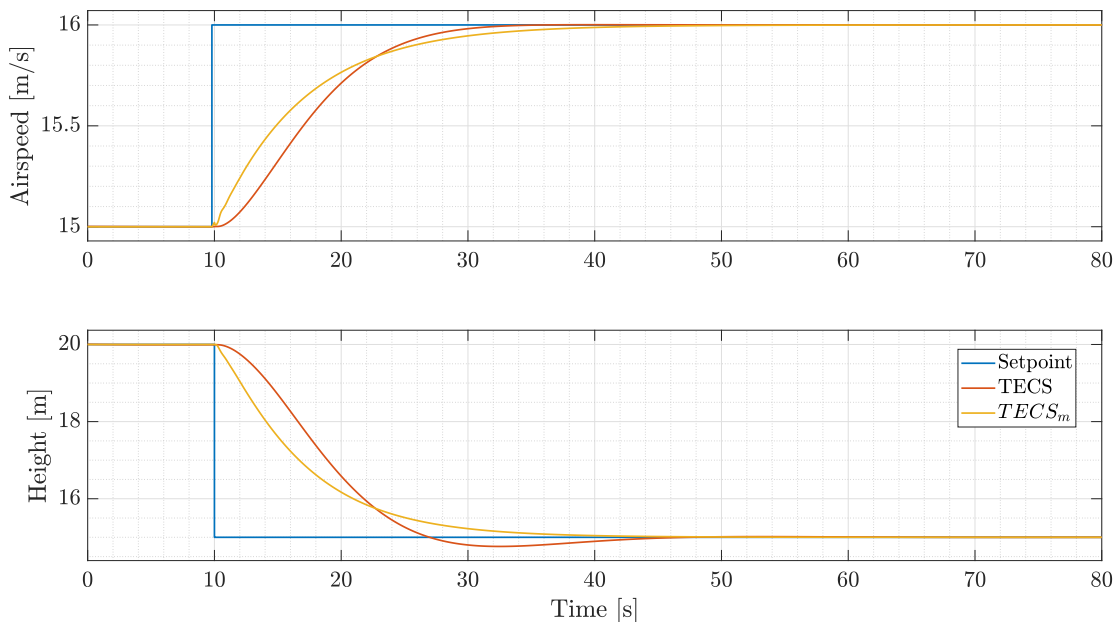


Figure 5.13: Simulation of a combined manoeuvre: 5 m descent and 1 m/s speed increase.

	Airspeed loss	Altitude loss	Oscillations	Settling time
TECS	0.35 m/s	0.76 m	YES	38 s
$TECS_m$	0.13 m/s	0.22 m	NO	24 s

Table 5.5: Airspeed and altitude loss during a trim recover simulation.

In particular, some spikes are present in these quantities; a saturation limit on the rate of the control input can be added to limit this effect ([36]). In addition to the tracking performance, the controller influences the system's phugoid dynamics ([37]): the potential oscillations in altitude and velocity are controlled, hence the phogid mode is automatically suppressed if triggered.

Both the controller presented are suitable for the control of the fixed-wing longitudinal dynamics.

During the transition phase the VTOL passes from multicopter mode to fixed-wing mode in a few seconds: the fixed-wing controller has to trim the aircraft as soon as a predetermined speed is reached in the shorter possible time. In order to asses the ability of the airplane to deal with the transition phase, a similar condition is simulated. The simulation is initialized at $v_{cruise} = 15$ m/s and at 20 m height: the controller has to maintain them, but starting with level attitude, null throttle and null elevator deflection. The result are depicted in Figure 5.14. The performance of $TECS_m$ controller is better compared to the standard TECS (Table 5.5): the loss of airspeed and height and the settling time are significantly smaller.

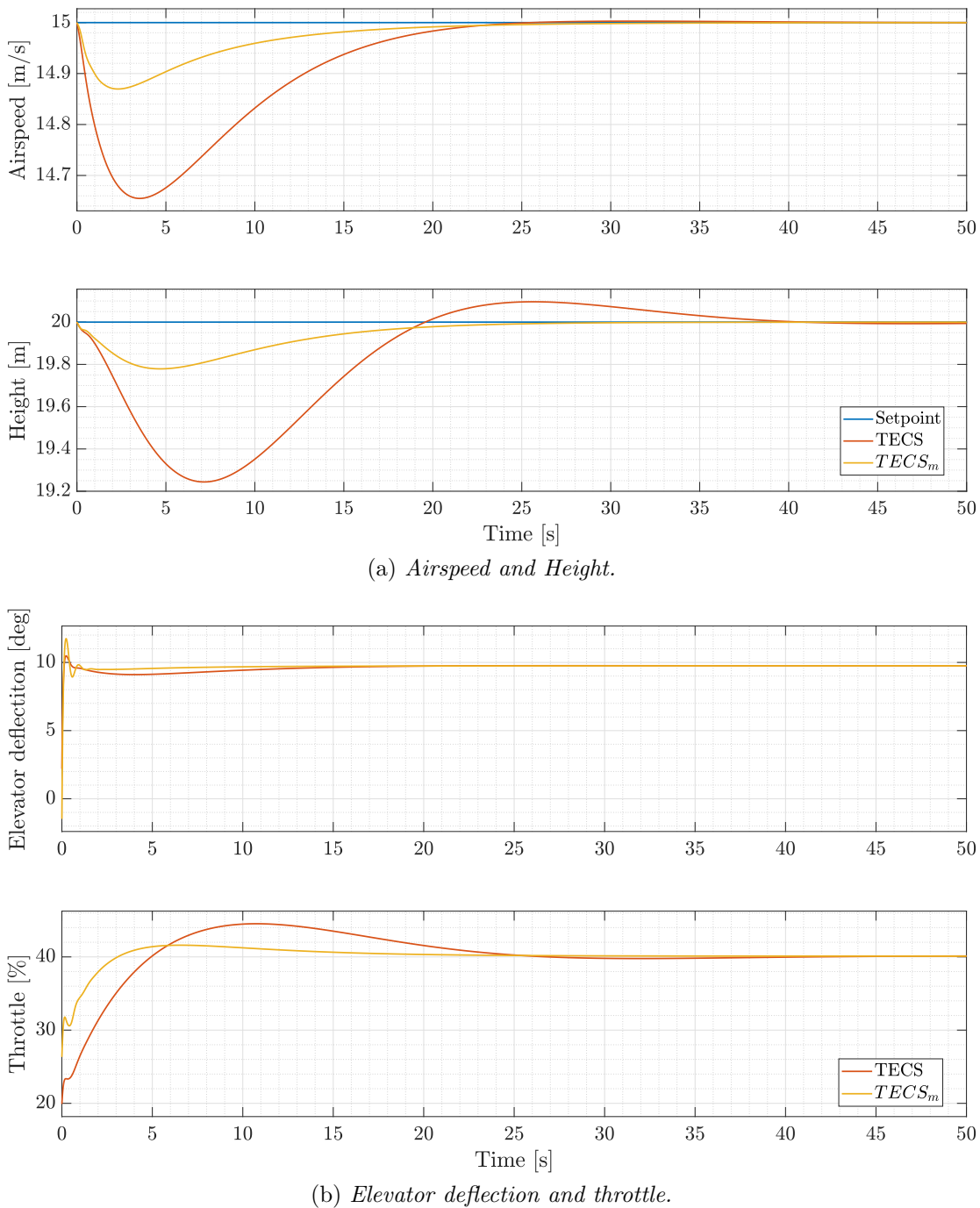


Figure 5.14: Trim recover simulation: physical quantities.

Chapter 6

Transition controller

The transition is the flight phase during which the VTOL passes from multicopter mode into fixed-wing mode and *vice versa*. In this chapter the problem of controlling the VTOL during the transition phase is considered.

First the possible ways to perform the transition from multicopter mode into fixed-wing mode and the main goals are described. In the second section the selected strategy is implemented, simulated and analysed. Then, a possible solution to perform the transition from fixed-wing mode to multicopter mode (back transition) is presented. In the last section, the logic to manage all the phases of a complete mission is presented, together with the result of an indoor flight test.

6.1 Transition

The transition from multicopter mode to fixed-wing mode is done by accelerating forward; the speed increases, the wings start producing lift that will gradually replace the vertical force produced by the vertical motors in order to ensure equilibrium in the longitudinal plane. There are several ways to do this; the main have been summarized in [2]. Two main distinctions have been made: the first is the starting point (from a hover condition or from a climb/descent condition); the second is how the forward acceleration is achieved (by using only the forward motor while keeping a level attitude or like a normal multicopter, by pitching the VTOL forward). From these distinctions four strategies have been designed:

- 1st strategy:
 - starting condition: hover;
 - forward acceleration strategy: forward motors, keeping level attitude.
- 2nd strategy:
 - starting condition: hover;

- forward acceleration strategy: multicopter mode, pitching the VTOL forward.
- 3rd strategy:
 - starting condition: climb;
 - forward acceleration strategy: forward motors, keeping level attitude.
- 4th strategy:
 - starting condition: climb;
 - forward acceleration strategy: multicopter mode, pitching the VTOL forward.

6.1.1 Selected strategy

The choice fell on the first one: in all the other options the pitching forward manoeuvre and the climbing manoeuvre cause a negative angle of attack condition. Hence the wings generate negative lift that must be balanced by an additional thrust produced by the vertical motors. In addition, the aerodynamic model developed in [2] is valid only for small angles of attack; an accurate simulation is then not possible.

6.1.2 Goals

The main goal is to pass from hovering condition to the cruise condition ($v = 15$ m/s) in fixed-wing configuration. This must be done quickly, smoothly, without oscillations and especially without altitude changes.

The tasks to be carried out by the multicopter controller and by the fixed-wing controller are, respectively, the following:

- multicopter controller:
 - maintain constant altitude;
 - maintain level attitude;
- fixed wing controller:
 - maintain constant altitude;
 - maintain level attitude;
 - airspeed control.

The multicopter controller tasks are carried out with ALTITUDE MODE (Appendix A); this flight mode satisfies all the tasks requested. Also for fixed-wing controller the ALTITUDE MODE is used, but the pitch setpoint calculated by TECS is ignored. Thanks to this flight mode, the thrust of the vertical motors is automatically reduced when lift increases.

6.2 Implementation

The adopted strategy is described by the following steps:

1. hovering condition; null airspeed, level attitude. Multicopter control ON (in POSITION MODE).
2. Transition switch is activated.
3. Multicopter control switches to ALTITUDE MODE.
4. The fixed-wing controller is turned ON (in ALTITUDE) with a velocity setpoint of 15 m/s. Forward motors are activated at full throttle and the VTOL starts to accelerate.
5. Level attitude setpoint is maintained both from vertical motors and control surfaces, splitting the required control effort among the two controllers.
6. Airspeed and lift increase; at the same time multicopter vertical force decreases.
7. Once the stall speed is reached the fixed-wing controller takes full control. Multicopter control is turned OFF since the weight of the VTOL is fully balanced by the lift. Attitude (pitch setpoint) now is managed by TECS.
8. The VTOL continues to accelerate up to v_{cruise} .
9. Transition is completed.

In particular, the following actions are needed in order to correctly mix the contribution of the controllers during the transition phase:

- A** The command surfaces deflections are weighted as functions of airspeed with the scaling factor K_{FW} (Figure 6.1), that is defined as:

$$K_{FW} = \frac{V}{V_{stall}} \quad (6.1)$$

and limited between 0 and 1. So, the control surfaces have reduced authority at low speed and full authority at speed above the stall speed.

- B** The multicopter control moments are weighted as functions of airspeed with the scaling factor K_{MC} (Figure 6.1), that is defined as:

$$K_{MC} = 1 - \frac{V}{V_{stall}} \quad (6.2)$$

and limited between 0 and 1. So, the multicopter controller has full authority at low speed, that decrease with the increase of the speed. Above the stall speed it is turned off.

- C** Instead of ignoring the pitch setpoint calculated by TECS, the energy balance rate \dot{L}_e is set to zero for airspeed smaller than stall speed: the TECS algorithm returns a null pitch angle. When the stall speed is reached this quantity returns to its real value and the pitch setpoint necessary to fly in fixed-wing mode in that condition is calculated. This is done by the scaling factor K_{PITCH} (Figure 6.1). The value does not go instantly to one, but starts rising just before the stall speed.

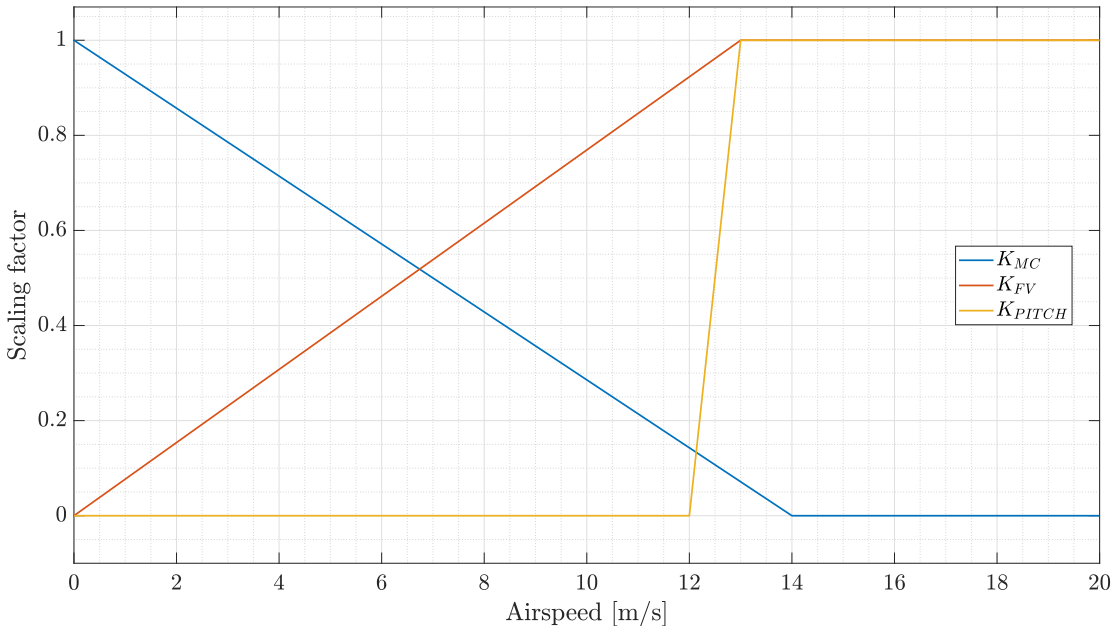


Figure 6.1: Scaling factors.

6.2.1 Simulation results

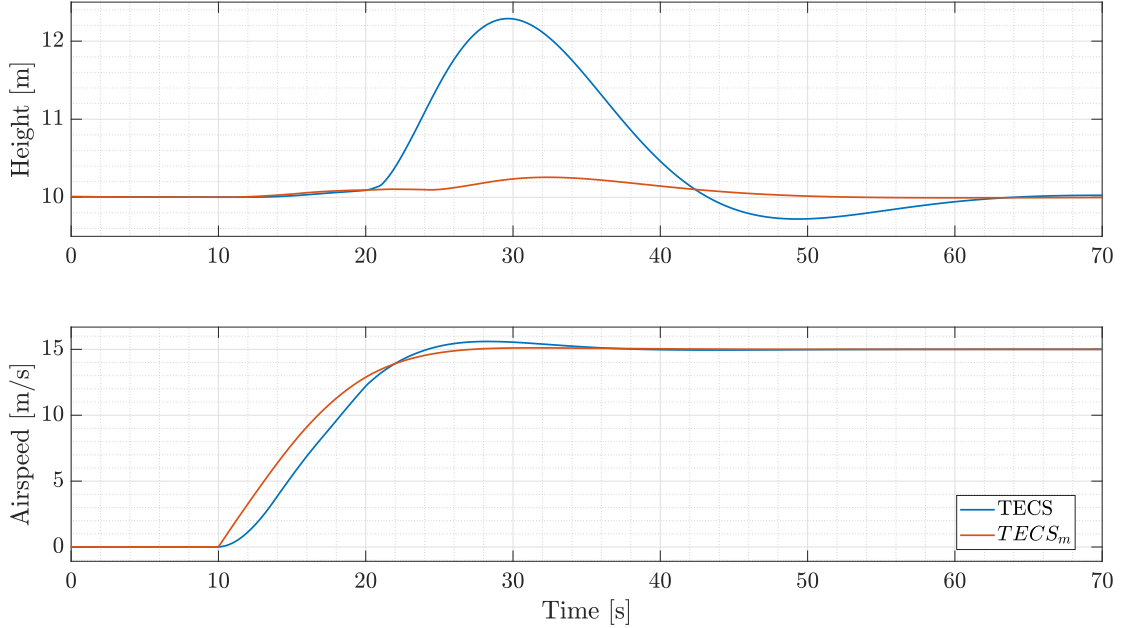
The simulation results obtained using the strategy described in the previous section are depicted in Figure 6.2; the transition command is given at 10 s from the simulation start. Both the TECS algorithms presented in Section 5.2.1 have been

	Altitude loss	Altitude gain	Time required
TECS	0.28 m	2.29 m	> 60 s
$TECS_m$	NO	0.25 m	40 s

Table 6.1: Transition performance comparison.

tested. $TECS_m$ has much better performance: the altitude oscillations and required time are smaller (Table 6.1), confirming the result of the simulation shown in Figure 5.14. The required time considered in Table 6.1 refers to the time necessary to reach the fixed-wing configuration, the desired airspeed and altitude. If only the first two conditions are considered, the required time is equal to 15 s. The performance is calculated considering a motors thrust reduced by 25 % with respect to the one calculated on the test-bed (in [2]). In fact, during the flights in multicopter configuration, a performance reduction has been encountered, due to the elements (ESCs) mounted under the motors, that reduce the propeller disk area.

In the following analysis only the $TECS_m$ algorithm is considered, given the fact that it shows better performance. Figure 6.3 shows the trend of lift and multi-

Figure 6.2: Height and airspeed during transition for TECS and $TECS_m$ controllers.

copter vertical force during the manoeuvre: with increasing airspeed, lift gradually replaces the propulsive force, to maintain the vertical equilibrium.

Same considerations can be made on the moments (Figure 6.4): the aerodynamic pitching moment that is generated is initially balanced by the multicopter control action. With the increase of the speed, the multicopter controller loses authority, so the aerodynamic moment produced by the wing is controlled and cancelled by the elevator deflection. The final value of the propulsive moment is due to the forward motors, that are mounted with an offset on the pitch axis; it is correctly balanced by the aerodynamic moment.

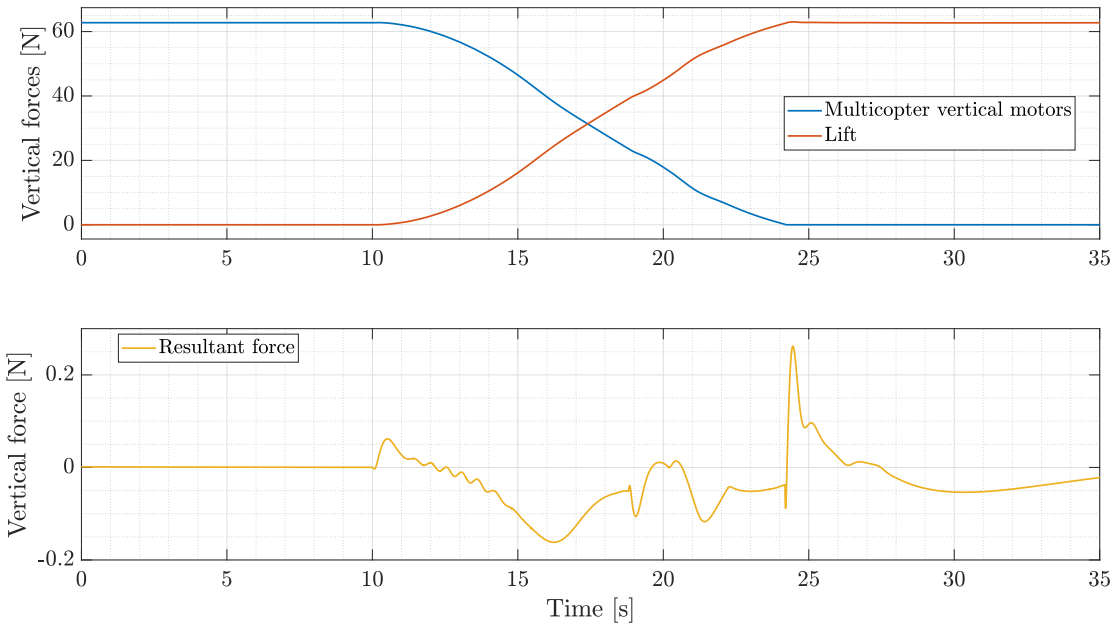


Figure 6.3: Vertical forces during transition.

During the transition no control on position is active: both controllers are in ALTITUDE MODE. A small drift in position occurs, as shown in Figure 6.5; the simulated value is almost irrelevant but, in the real case, it can be much larger due to wind and gusts. So, the less time is spent to perform the transition, the better.

Forward motors throttle and elevator deflection are shown in Figure 6.6.

6.2.2 Analysis

The actions implemented in Section 6.2 are the result of several simulations. In the following a more specific analysis on the choices made is done.

Action **A** and **B** are introduced in order to take into account the limits of the control actions: at low speed the effect of the command surfaces is irrelevant while at high speed the multicopter control action is less effective. So, more authority

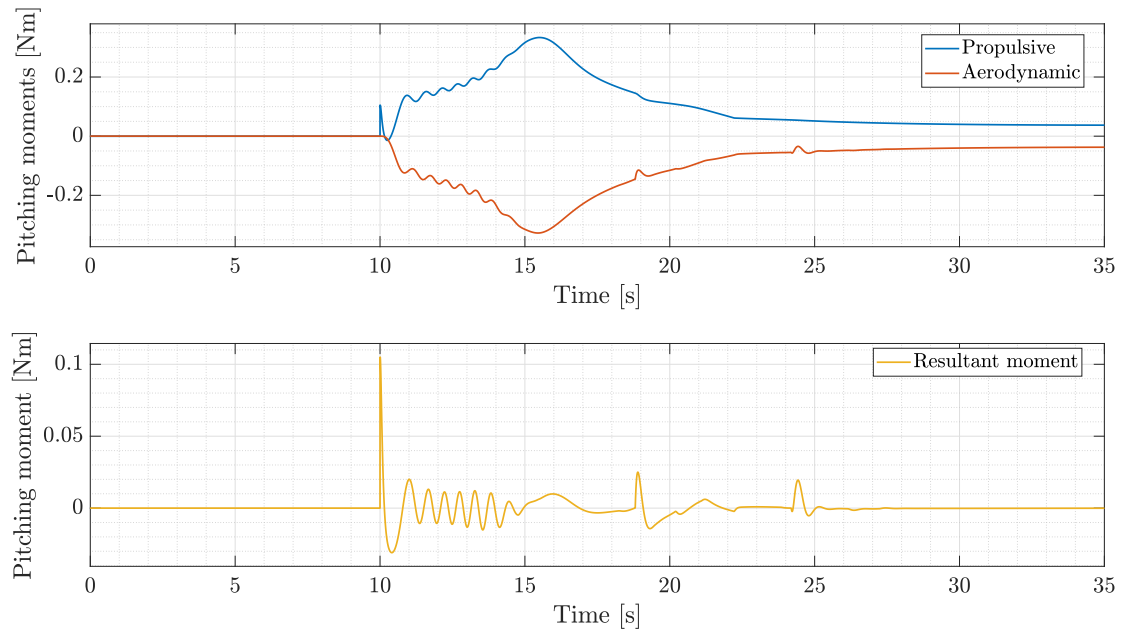


Figure 6.4: Pitching moments during transition.

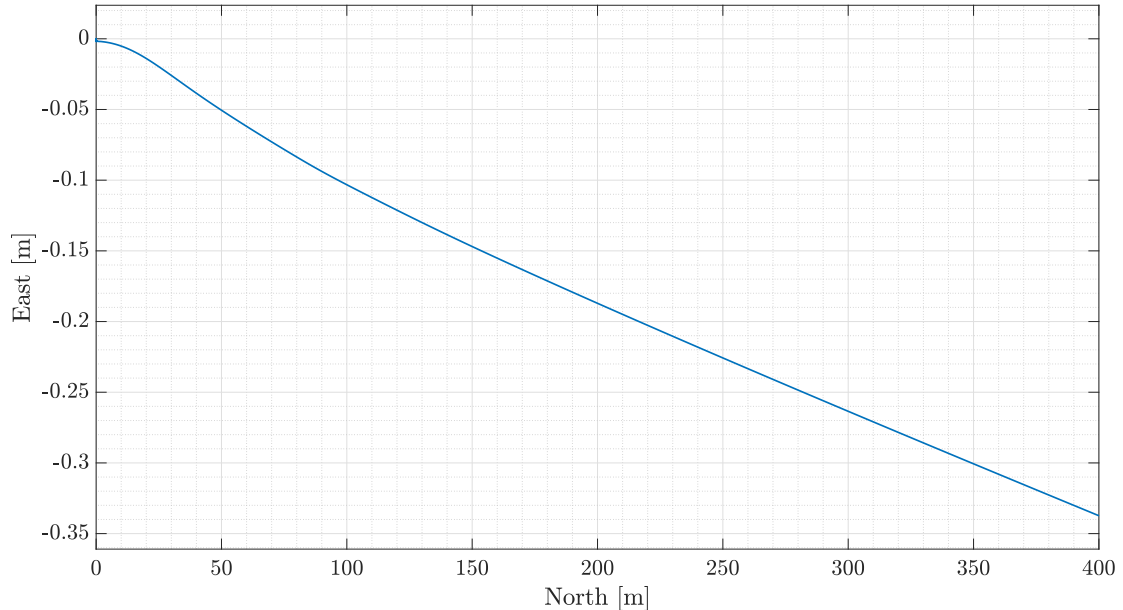


Figure 6.5: Horizontal position during transition.

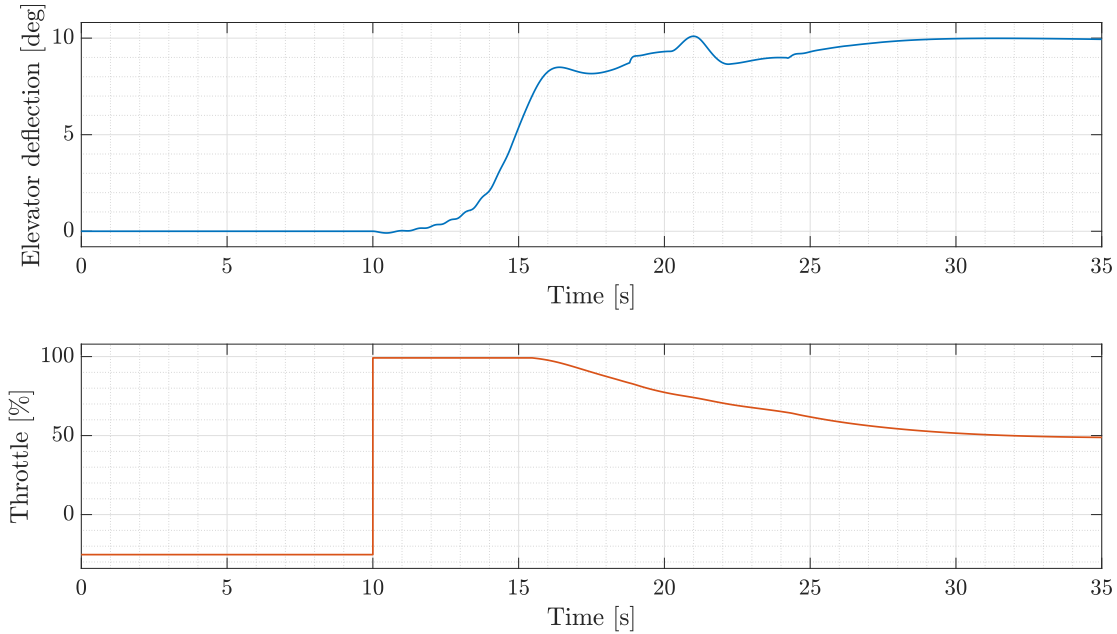


Figure 6.6: Elevator deflection and forward motors throttle during transition.

is given to the control logic that is more effective for that condition of airspeed using the scaling factors K_{FW} and K_{MC} , avoiding situations of contrast between the two controllers.

Without action **A**, strong oscillations in the elevator deflection occur. This reflects on dangerous oscillation in attitude. The elevator deflection is presented in Figure 6.7: in the first part of the manoeuvre it abruptly oscillates between max and min value. In Figure 6.8 the oscillation in pitch angle are evident.

From the figure it can also be notice that the chosen strategy guarantees a smooth transition, without any oscillation.

Action **C** keeps level attitude during the first part of the transition phase. The level attitude constraint is used to avoid negative angles of attack (in case of pitch-down manoeuvre) but also to maintain the multicopter vertical motors force perpendicular to the horizontal plane. A positive pitch angle causes a negative horizontal force component that contrasts the acceleration in the forward direction.

Without K_{PITCH} the transition fails. Other shapes of K_{PITCH} have been tested, e.g., K_{PITCH_m} null at hover and then increasing linearly to unit value for airspeed equal to stall speed. The results of altitude and airspeed are depicted in Figure 6.9. At a first glance this approach seems to work well, better than the chosen strategy. But strange coupling phenomena occur: the fixed wing controller calculates the pitch angle necessary to fly with the reduced weight of the aircraft. This leads to a new equilibrium condition in which the two contributions collaborate:

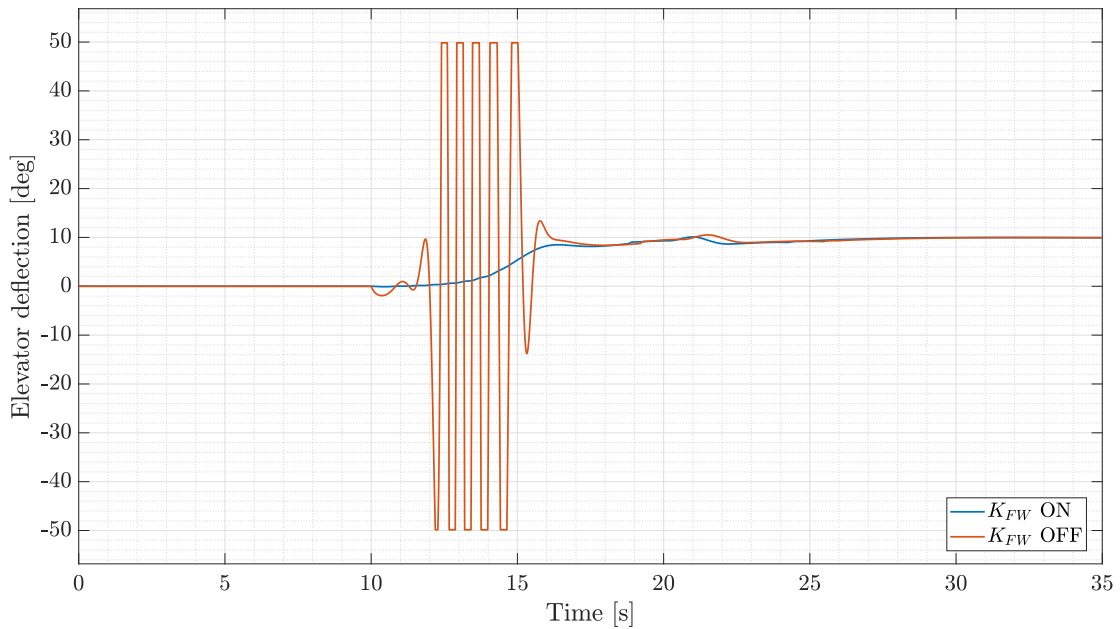


Figure 6.7: Elevator deflection during transition: action **A** activated and deactivated.

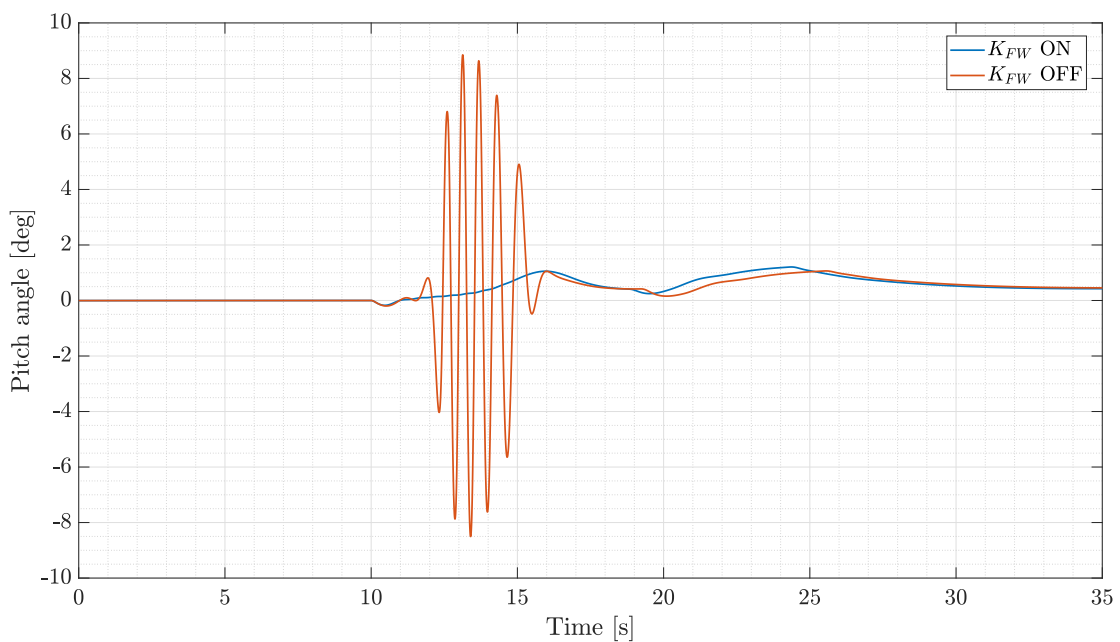


Figure 6.8: Pitch angle during transition: action **A** activated and deactivated.

part of the weight is balanced by the multicopter vertical force and the reduced weight resultant by the fixed-wing. This is evident in Figure 6.10, where lift and multicopter vertical force are shown. The latter does not go to zero but settles down to a non-zero equilibrium value. Then the fixed-wing is trimmed considering the reduced weight. In Figure 6.11 the comparison between the pitch angle of the chosen strategy and the latter is depicted.

As can be seen from the figures, the transition with K_{PITCH_m} is not completed and therefore this approach is discarded.

A possible solution to overcome this problem is to apply the scaling factor K_{MC} not only to the control moments, but also to the force calculated by the multicopter controller. By doing this, the multicopter controller is forced to stop once the stall speed is reached. However, this causes an unavoidable descent: the force calculated to ensure the vertical equilibrium is then reduced by the scaling factor. The simulated altitude loss is about 0.4 m (the controller automatically increases the force to overcome the descent), while this loss is not significant, a problem may arise when the calculated stall speed is not reliable. Indeed when that speed is reached the multicopter will shut down, regardless if the lift produced is enough to balance the weight or not: the vehicle may fall. So, also this option is not to be considered.

An important remark is that all the implemented actions depend on the stall speed; an inaccurate value can have serious consequences. A fixed-wing flight test campaign to better estimate this value is recommended. Also, the airspeed measurement has a central role; the low pass filter introduced in Section 5.1.3 is essential.

6.3 Back transition

Back transition is the inverse process with respect to transition: the aircraft goes from a fixed-wing condition to hovering condition in multicopter mode; this must be achieved without altitude loss and in the shortest time and distance. A possible strategy, that is not yet simulated, can be:

- starting point: fixed-wing mode at any airspeed.
- Back transition switch is activated.
- The airspeed is reduced by setting the throttle to idle and using air brakes. Height is maintained with the elevator action; the VTOL will be pitched up.
- Once the stall speed is reached, the multicopter controller is turned ON while the fixed-wing controller is turned OFF.
- Ending point: hovering condition.

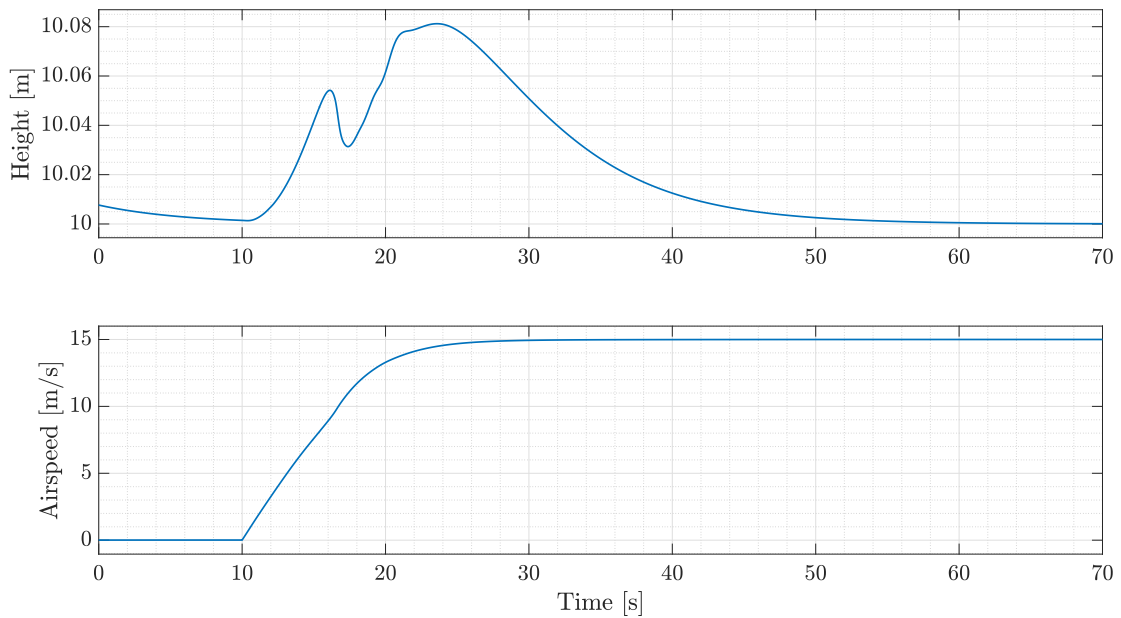


Figure 6.9: Height and airspeed during transition with scaling factor K_{PITCH_m} .

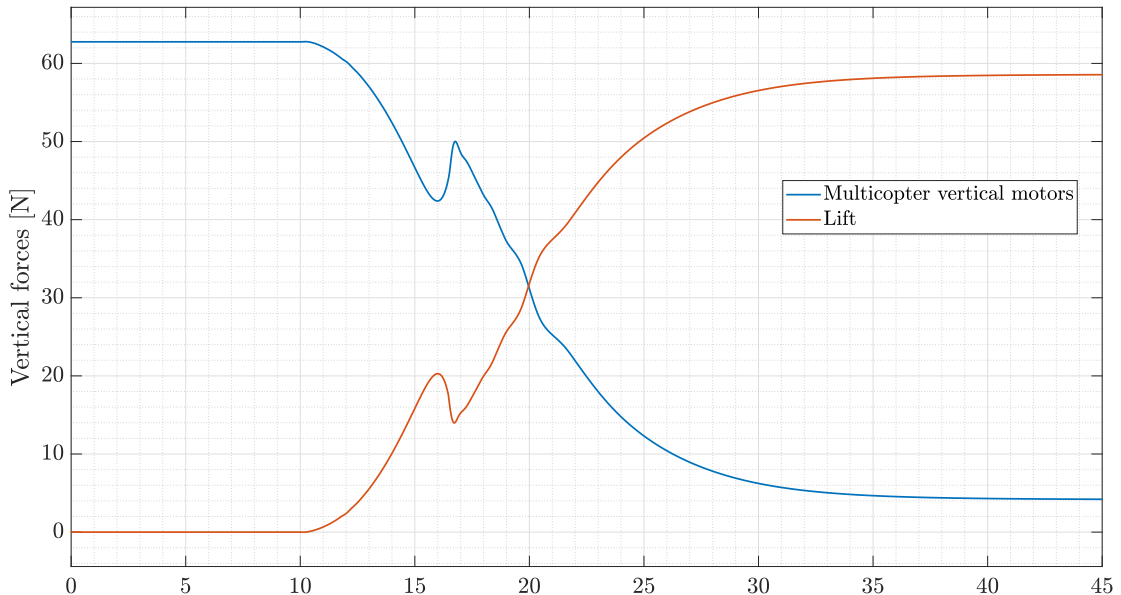


Figure 6.10: Vertical forces during transition with scaling factor K_{PITCH_m} .

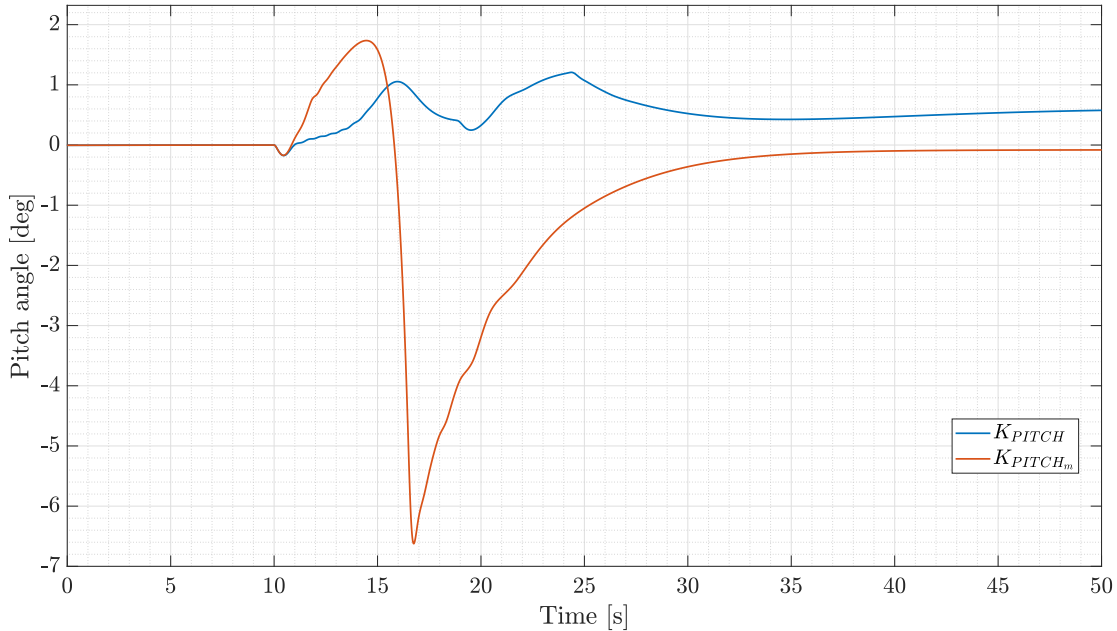


Figure 6.11: Pitch angle during transition: with K_{PITCH} and K_{PITCH_m} .

Note that the two rudders can be used like air brakes by ordering an opposite deflection. The rudders are connected specifically to two different FCU ports to be able to command them differently.

The activation of the multicopter controller in POSITION MODE can cause abrupt manoeuvres; the option to use only the velocity loop with null speed setpoint might be considered. Once stopped, POSITION MODE is enabled in order to maintain the current position.

6.4 Mission management and indoor testing

Mission management

A complete VTOL mission includes: vertical take-off and climb, fixed-wing mode flight, vertical descent and landing. Mission management is assigned to an unique system that brings together both the controllers (multicopter controller and fixed-wing controller are implemented in the same *Simulink* file). The controllers are activated and weighted according to states that represent the flight condition of the aircraft (see Table 6.2): they depend on the pilot command (switch SB (Appendix A)), flight mode, airspeed and current state. The states assignment logic is shown in Table 6.3. The feedback on the current state prevents unwanted changes of state. For example: the VTOL starts from a multicopter configuration, the transition is activated with the switches, once the v_{cruise} is reached the controller passes in fixed-wing state. However, a reduction of speed, above v_{cruise} ,

State	Mission phase
0	Multicopter
1	Transition
2	Fixed-wing
3	Back transition

Table 6.2: VTOL mission states.

Pilot switch	Flight mode	Airspeed	Current state	State
0	/	/	/	0
1	Altitude OFF	/	/	0
1	Altitude ON	/	/	1
1	Altitude ON	$v \geq v_{cruise}$	/	2
1	Altitude ON	$v < v_{cruise}$	2	2
2	Position OFF	/	/	2
2	Position ON	/	2	3
2	Position ON	$v < v_{back}$	/	0
2	Position ON	$v > v_{back}$	0	0

Table 6.3: States assignment logic.

would cause the change of state, returning in transition phase.

In Figure 6.12 the simulation of a mission composed of vertical take off, transition, climb, cruise, descent in fixed-wing is depicted.

Indoor testing

An indoor flight test has been performed in order to asses the implemented transition logic, the mission management system and the proper operation of hardware and software. The test consists of: vertical take off in multicopter POSITION MODE, hovering, first part of transition manoeuvre. For obvious reasons (the test is performed in the Flight arena, with a flight volume of 6 x 12 x 4 m) the transition is stopped by the pilot action in the early stages and the throttle of the forward motors is limited to 20%.

The switches related to flight modes and states are show in Figure 6.13. The first part of the flight is carried out in POSITION MODE. The transition phase starts when the pilot activates the transition switch and passes to ALTITUDE MODE (Appendix A); the state switch reaches unit value, forward motors turn on and the VTOL starts accelerating in the forward direction. Forward velocity and position can be seen in Figure 6.14: the VTOL is accelerating keeping a level

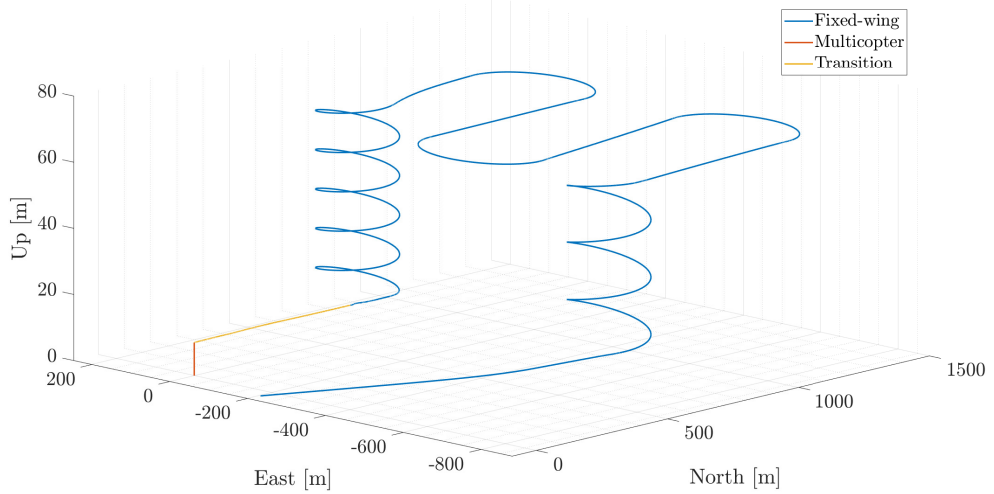


Figure 6.12: VTOL mission. Vertical take off, transition and fixed-wing phase.

attitude (Figure 6.15). After a few meters the transition is blocked and the VTOL stopped with a pitch-up manoeuvre.

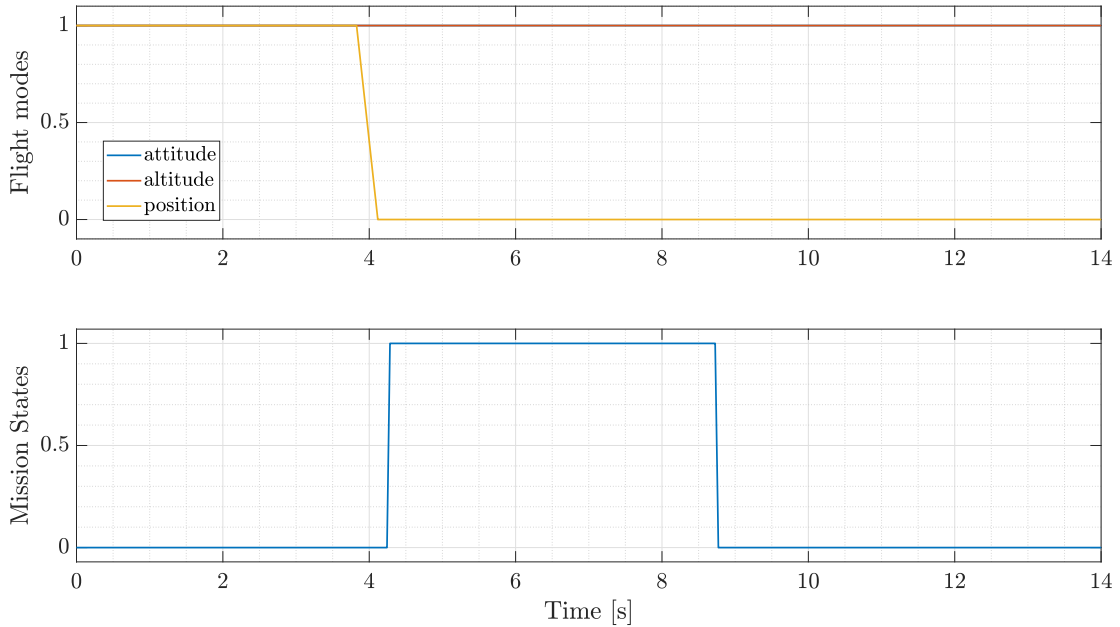


Figure 6.13: Flight modes and states switches during transition phase.

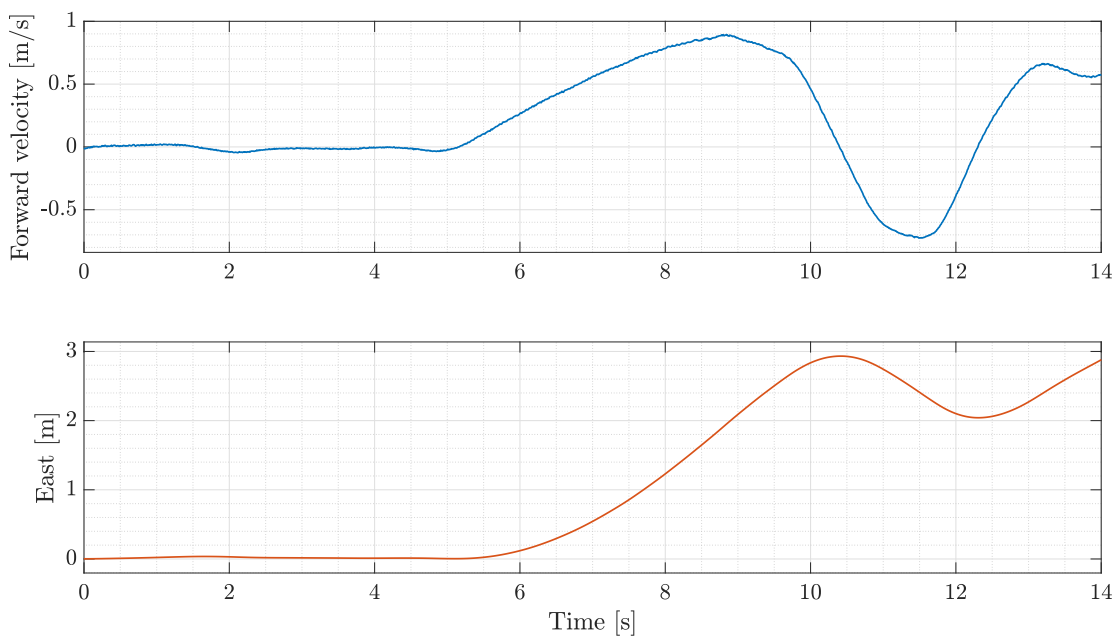


Figure 6.14: Forward velocity and position during transition phase.

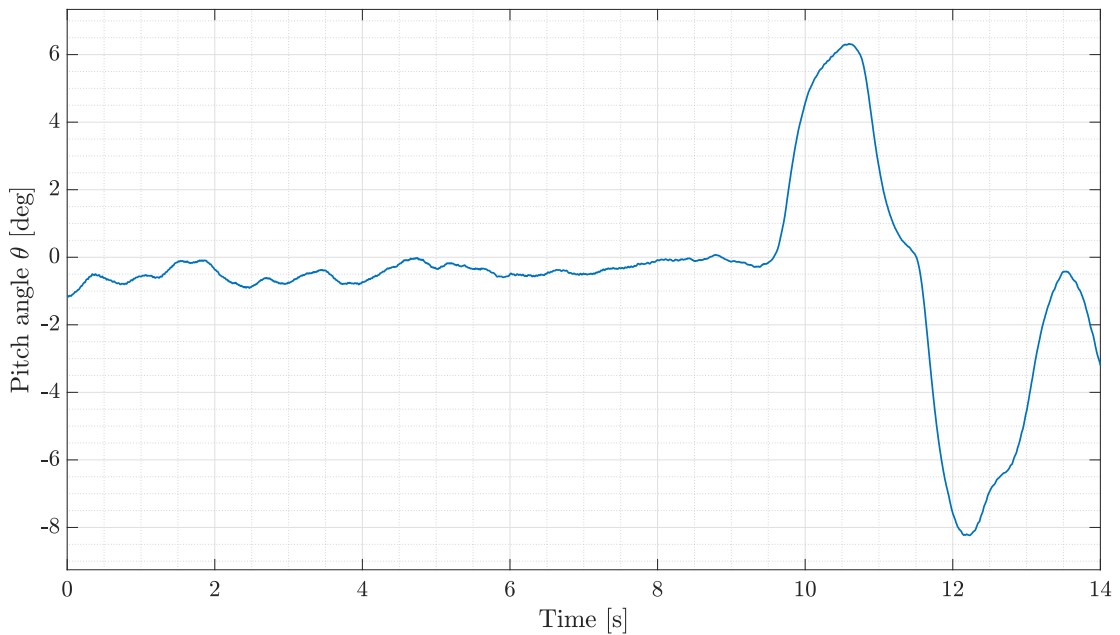


Figure 6.15: Pitch angle during transition phase.

Conclusions

In this thesis the integration, control, modelling and testing of an eVTOL completely designed within the *ASLC* Laboratory of *Politecnico di Milano* has been carried out. The starting point of the present work is the VTOL designed and built in two previous master thesis ([1] and [2]).

The initial part of the thesis is devoted to the update of the VTOL hardware to fix the problems faced during the first flight tests: in particular, the weight and balance of the aircraft have been improved manufacturing a lighter wood tail. The second modification is related to the propulsive system: the vertical motor propellers have been changed to provide the necessary force to lift the drone; a second battery and an additional power distribution board have been installed to mitigate problems related to power distribution.

Once the hardware problems have been solved, the controller for multicopter flight mode has been designed: a cascade PID loops architecture has been adopted, the inner loop to control the attitude and the angular rates, the outer to control the position and the velocity. The tuning has been manually performed in flight; the achieved performance is satisfactory in terms of gain and phase margins.

The multicopter model has been identified using a black-box approach, focusing on the longitudinal, lateral, directional and vertical dynamics. The best results have been obtained using a frequency sweep excitation signal since it better excites the low frequency dynamics. The identified model, implemented into the multicopter part of the simulator developed in [2], has been validated against a flight experiment obtaining good results.

The VTOL aircraft can fly both as a multicopter and as a fixed-wing; then, a controller for the fixed-wing mode has been developed and tested in simulation. The selected architecture is made up of two loops, the inner one for attitude control and the outer one for airspeed and altitude. The outer loop implements the total energy control system (TECS) in two variants: this choice has been made in order to design a controller suitable also for the transition phase.

Last but not least, the transition has been investigated: it is the flight phase during which the VTOL passes from multicopter mode into fixed-wing mode and *vice versa*. A transition strategy has been implemented: since in this phase both controllers work, it is required to mix the controller outputs; the mixing procedure is based on the forward velocity and the stall speed. The implemented controller

has been tested only in simulation achieving good results, as presented in Figure 6.12.

The results obtained present some limitations:

- for the multicopter controller the tuning has been performed only manually in flight; no systematic tuning based on the identified model has been performed. In this way, the controller performance are not optimal.
- The fixed-wing and the transition controllers have been tuned and tested only in simulation; the obtained performance need to be verified in real flight. Moreover, the tuning procedure in simulation only may lead to wrong controller gains due to the rigid body assumption used in the fixed-wing part of the simulator.

Starting from the obtained results and their limitations, the following activities can be outlined:

- flight testing of the fixed-wing configuration to assess the controller performance, identify the stall speed (fundamental in the transition control) and the dynamic model;
- comparison of the identified fixed-wing model with the analytical one used in simulation, with focus on the structural model and the aerodynamic characteristics of the aircraft;
- test of the transition procedure both in the updated simulator and in real flight;
- implementation and testing of the proposed back-transition procedure, first in simulation and then in flight.

The experience gathered during this work and the previous master thesis ([1] and [2]) may be used to develop a new VTOL aircraft which improves the limiting aspects of the present one:

- improved propulsion system to avoid excessive voltage drop and current demand during the multicopter flight, in order to obtain better endurance performance of the aircraft;
- better fuselage structure to avoid structure-control coupling problems reducing at the same time the overall mass.

Bibliography

- [1] N. Battaini. “Design and dynamic modeling of a VTOL UAV”. MA thesis. Politecnico di Milano, 2020.
- [2] N. Martello. “Modelling and integration of an eVTOL UAV”. MA thesis. Politecnico di Milano, 2021.
- [3] *The Verge, Alphabet’s Wing kicks off drone delivery service in Dallas on April 7th.* <https://www.theverge.com/2022/4/4/23006894/alphabet-wing-drone-delivery-dallas-kick-off>.
- [4] *The Verge, Alphabet’s drone delivery service Wing hits 100,000 deliveries milestone.* <https://www.theverge.com/2021/8/25/22640833/drone-delivery-google-alphabet-wing-milestone>.
- [5] *FedEx, FedEx Plans to Test Autonomous Drone Cargo Delivery with Elroy Air.* <https://newsroom.fedex.com/newsroom/elroyair>.
- [6] *Wing, Continental Drones.* <https://wingcopter.com/continental-drones>.
- [7] *Wing, multi-million-dollar delivery drone orders.* <https://wingcopter.com/series-a-extension>.
- [8] *Forbes, Google’s Wing Kicks Off Mall-To-Home Drone Delivery Service.* <https://www.forbes.com/sites/johnkoetsier/2021/10/06/world-first-drone-delivery-googles-wing-starts-mall-to-home-flights/?sh=1059c28311f0>.
- [9] S. O. H. Madgwick. *An efficient orientation filter for inertial and inertial/magnetic sensor arrays.* Tech. rep. University of Bristol, Apr. 2010.
- [10] G. Gozzini. “UAV autonomous landing on moving aerial vehicle”. MA thesis. Politecnico di Milano, 2019.
- [11] R. W. Prouty. *Helicopter performance, stability and control.* John Wiley & Sons Ltd, 1986.
- [12] M. Lovera, F. Riccardi, and P. Panizza. “Identification of the attitude dynamics for a variable-pitch quadrotor UAV”. In: *European Rotorcraft Forum (ERF) 2014 proceedings* (Sept. 2014).

- [13] G. Fumai. “Accuracy analysis of $PBSID_{opt} - H\infty$ for multirotor UAVs model identification”. MA thesis. Politecnico di Milano, 2020.
- [14] *Optitrack motion capture system*. <https://optitrack.com/>.
- [15] *Motive: Optical motion capture software*. <https://optitrack.com/software/motive/>.
- [16] *Optitrack camera*. <https://tracklab.com.au/products/brands/optitrack/optitrack-prime-cameras/>.
- [17] *QGroundControl*. <http://qgroundcontrol.com/>.
- [18] *KDE Motors Website*. <https://www.kdedirect.com/pages/motors>.
- [19] *Holybro Power Distribution Board Website*. <http://www.holybro.com/product/pixhawk-4-power-module-pm07/>.
- [20] *Electronic Design Master*. <https://www.edmelectronics.eu/tutorial/come-misurare-la-resistenza-interna-di-pile-e-batterie/>.
- [21] *Turnigy RC Power Systems*. <https://turnigy.com/>.
- [22] *T-MOTOR*. <https://uav-en.tmotor.com/>.
- [23] *Px4 Autopilot Website*. <https://px4.io/>.
- [24] *Px4 Controller Diagrams*. [https://docs.px4.io/v1.12/en/flight_stack/controller_diagrams.html/](https://docs.px4.io/v1.12/en/flight_stack/controller_diagrams.html).
- [25] *Px4 Autopilot Discussion Forum*. <https://discuss.px4.io/>.
- [26] G. Bressan. “Hardware/software architecture, code generation and control for multirotor UAVs”. MA thesis. Politecnico di Milano, 2018.
- [27] D. Brescianini, M. Hehn, and R. D’Andrea. “Nonlinear Quadrocopter Attitude Control”. In: *ETH Library* (Oct. 2013).
- [28] *PX4 Multicopter PID Tuning Guide*. https://docs.px4.io/v1.12/en/config_mc/pid_tuning_guide_multicopter_basic.html.
- [29] J. W. van Wingerden et al. *Predictor-based subspace identification toolbox*. https://www.dcsc.tudelft.nl/~jwvanwingerden/pbsid/pbsidtoolbox_product_page.html.
- [30] A. N. Tikhonov and V. Y. Arsenin. “Solutions of ill posed problems”. In: *Scripta series in mathematics. V. H. Winston and Sons* (1977).
- [31] D. Chevallard. “Design, identification and control of a micro aerial vehicle”. MA thesis. Politecnico di Milano, 2017.
- [32] P. C. Hansen. *Regularization tools: a MATLAB package for analysis and solution of discrete ill-posed problems, version 4.1*. <http://www.imm.dtu.dk/~pcha/>.

- [33] D. Migliore. "Model identification and inversion-based control for multirotor UAVs". MA thesis. Politecnico di Milano, 2019.
- [34] M. Giurato. "Design, integration and control of a multirotor UAV platform". MA thesis. Politecnico di Milano, 2015.
- [35] S. Fari. "Guidance and control for a fixed-wing UAV". MA thesis. Politecnico di Milano, 2017.
- [36] G. R. Balmer. "Modelling and Control of a Fixed-wing UAV for Landings on Mobile Landing Platforms". In: *Royal Institute of Technology* (Oct. 2015).
- [37] P. Chudy and P. Rzucidlo. "TECS/THCS based flight control system for general aviation". In: *AIAA Modeling and Simulation Technologies Conference* (Aug. 2009).
- [38] K. R. Bruce. "NASA B737 Flight Test Results of the Total Energy Control System". In: *NASA* (July 2009).
- [39] L.P. Faleiro and A.A. Lambregts. "Analysis and tuning of a 'Total Energy Control System' control law using eigenstructure assignment". In: *Aerospace Science and Technology* (Feb. 1999).
- [40] J. Zhang et al. "Application of Total Energy Control on Vertical Take-off and Landing UAV". In: *IMCEC 2019* (May 2019).
- [41] *FrSky Radio Controller Website*. <https://www.frsky-rc.com/>.

Appendix A

Flight modes

The PX4 autopilot presents different flight modes, exploiting the cascade loops structure of the controller. Flight modes define how the controller responds to remote control input, providing different levels of assistance to the pilot. This is achieved by managing the control loops activated.

Figure A.1 shows the radio controller, highlighting the sticks used for the different flight modes; they are described in the following starting from the kill switch, used as a safety measure: in case of dangerous behaviour of the vehicle the pilot can immediately stop the motors (while this switch is active the controller sends the disarm PWM to the motors). The SB switch is set as transition switch, allowing the activation of this manoeuvre. During the identification campaign it is also used to stop the experiment in case of unexpected/dangerous situations. the SC and SD switches manage the flight modes: stabilized mode when both are in the upper position, altitude mode when the SC switch is in centered position and the SD switch is in upper position, position mode when both are centered and finally offboard mode when the SC switch is in centered position and the SD switch is in lower position.

In Figure A.2 the multicopter's controller diagram is shown while in Figure A.3 the fixed-wing one.

A.1 Multicopter flight modes

The following list summarizes flight modes for the multicopter case, describing the roles of the sticks and the active control loops. The modes are ordered in increasing pilot workload.

Offboard mode

The offboard mode is the flight mode used to control the vehicle through the



Figure A.1: FrSky Taranis X9D remote controller ([41]).

Flight mode	X	Y	Z	T
Position	speed v_x	speed v_y	yaw rate $\dot{\psi}$	speed v_z
Altitude	roll angle θ	pitch angle ϕ	yaw rate $\dot{\psi}$	speed v_z
Stabilized	roll angle θ	pitch angle ϕ	yaw rate $\dot{\psi}$	throttle th_{MC}

Table A.1: Radio commands for multicopter flight modes.

ground station. The setpoints given to the drone are position (in the inertial frame) and yaw angle ψ . The position loop is always active (Figure A.2).

Position mode

The position mode is the simplest flight mode. The X and Y stick controls body velocity over ground, v_x and v_y respectively. Z control yaw rate $\dot{\psi}$ and T controls the climb/descent speed v_z . When the sticks are centered the vehicle maintains the current leveled position, compensating for wind and other forces.

The velocity loop is active during maneuvers, the position loop works only when the sticks are centered (Figure A.2).

Altitude mode

In this mode, the X and Y stick controls the roll angle ϕ and the pitch angle θ respectively, Z controls the yaw rate $\dot{\psi}$ and T the speed of climb/descent v_z . When the sticks are centered the vehicle will level and maintain the current altitude. The drone does not maintain the in-plane position; if moving or disturbed by external forces, the vehicle will continue drifting in the horizontal plane.

The attitude loop is active. The vertical force F_v is calculated by attitude extraction module considering only the vertical force component calculated respectively by the velocity controller during maneuvers and by the position and velocity controllers when the sticks are centered (Figure A.2).

Stabilized (Attitude) mode

The X and Y stick controls the roll angle ϕ and the pitch angle θ , Z controls the yaw rate $\dot{\psi}$ and T the throttle of the motors th_{MC} . Altitude control is managed by the ability of the pilot to set appropriately the throttle th_{MC} . When the X and Y stick is centered the vehicle will level. The drone does not maintain the position; if moving or disturbed by external forces, the vehicle will continue drifting. Only the attitude loop is active (Figure A.2).

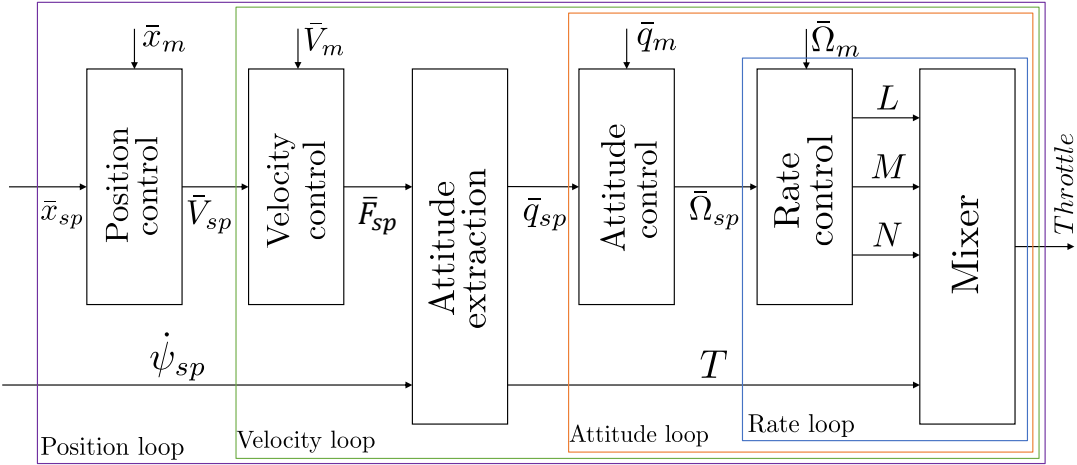


Figure A.2: Multicopter controller.

Flight mode	X	Y	Z	T
Altitude	roll angle θ	climb/descent rate \dot{H}	rudder deflection δ_r	speed V
Stabilized	roll angle θ	pitch angle ϕ	rudder deflection δ_r	throttle th_{FW}

Table A.2: Radio commands for different fixed-wing flight modes.

A.2 Fixed-wing flight modes

The list below summarizes flight modes for the fixed-wing case, describing the roles of the sticks and the active control loops. The modes are ordered in increasing pilot workload.

Altitude mode

X controls the roll angle ϕ , Y controls the climb/descent rate \dot{H} , Z control the rudder deflection δ_r and T the forward speed V . When the sticks are centered the aircraft will level and maintain the current altitude and speed. The mode will not attempt to hold the vehicle course against wind.

The TECS controller and the attitude loop are active (Figure A.3).

Stabilized (Attitude) mode

X and Y stick controls the roll angle ϕ and the pitch angle θ , Z controls the rudder

deflection δ_r and T the throttle of the motors th_{FW} . The vehicle climbs/descends and accelerates according to the throttle th_{FW} and the pitch command θ . When the X and Y stick is centered the aircraft will level. The mode will not attempt to hold the vehicle course against wind. Only the attitude loop is active (Figure A.3).

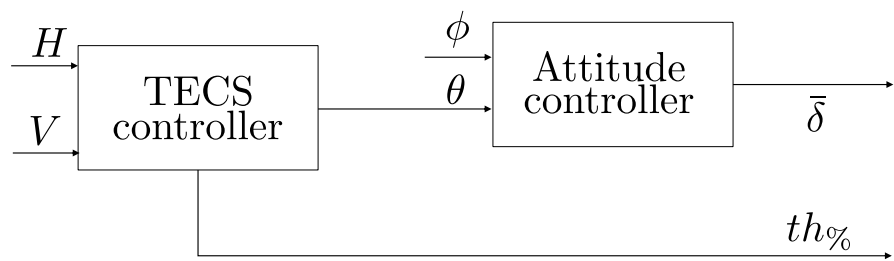


Figure A.3: Fixed-wing controller.

